Nonlinear Optics in a Thermal Rb Vapour at High Magnetic Fields

WHITING, DANIEL,JAMES

Nonlinear Optics in a Thermal Rb Vapour at High Magnetic Fields

Daniel J. Whiting

Abstract

We present investigations of nonlinear optical phenomena using a ^{87}Rb thermal vapour in a high magnetic field. The magnetic field (of strength 0.6 T) separates the optical transitions by more than their Doppler-broadened linewidths. This technique provides a high level of control over thermal-vapour systems, which can be used as a simpler alternative to conventional state-preparation methods such as optical pumping. Using this approach, we study electromagnetically induced transparency in a non-degenerate 3-level ladder system. Finding excellent agreement with the numerically modelled transmission spectra, we are able to directly infer the dipole moment of the $5P_{3/2} \rightarrow 5D_{5/2}$ transition $|\langle 5P_{3/2}||er||5D_{5/2}\rangle| = (2.27 \pm 0.002_{\text{stat}} \pm 0.04_{\text{syst}})\ ea_0$. Changing the coupling field to a standing-wave geometry, we observe resonant enhanced absorption: an effect that previously had only been observed in systems involving 4 or more atomic states. We also consider four-wave mixing (FWM) in a diamond level-scheme. Compared to the zero magnetic field case, we find good agreement with the FWM spectra using a simple model, even in the regime of strong laser dressing. Finally, we investigate heralded single-photon generation by spontaneous FWM. With strong laser dressing we observe the appearance of collective quantum beats, a single-photon interference effect due to the relative motion of atoms in a collective spin excitation. A violation of the Cauchy-Schwarz inequality by 6.7 standard deviations is reported.

Nonlinear Optics in a Thermal Rb Vapour at High Magnetic fields

Daniel J. Whiting

A thesis submitted in partial fulfilment
of the requirements for the degree of
Doctor of Philosophy

Department of Physics
Durham University

25th September 2017

Contents

List of Figures

Declaration

I confirm that no part of the material offered has previously been submitted by myself for a degree in this or any other University. Where material has been generated through joint work, the work of others has been indicated.

Daniel J. Whiting
Durham, 25th September 2017

Acknowledgements

First and foremost, I would like to thank my two supervisors, Ifan Hughes and Charles Adams, without whom I would not a have a thesis at all. Ifan has been an endless source of encouragement, with a seemingly inexhaustible supply of anecdotes in every imaginable situation, and the infectious drive and enthusiasm of Charles has been instrumental in the advancement of this research. I would also like to take this opportunity to thank the Engineering and Physical Sciences Research Council (Grant No. EP/L023024/1) and Durham University for their financial support.

My years in AtMol have been some of the most enjoyable of my life and much of this can be attributed to the wonderful community of people who I have gotten to know here. Specifically, I would like to thank: James, Renju, Mark, Erwan, Nick, Rob and Hannes for entertaining and stimulating discussions in the realms of Physics and Philosophy; Teodora, for patiently listening to all of my grumblings and keeping my spirits up with regular coffee (if you can indeed call it that) breaks, and for providing unending feedback on the quality of my figures; the members of fAtMol and Alistair's mother for providing much-needed cake-based sustenance; and the members of fitMol for providing the perfect antidote to all of that cake. I am indebted to Ifan, Renju and James for investing a significant amount of their time and energy to proof-read this thesis (although any remaining mistakes are entirely the fault of the author). Without the hard work and skills of many department staff the experiments described in this thesis could not have been conducted. Therefore I extend my thanks to the whole Durham Physics Department

and in particular the staff of the mechanical workshop, who constructed the magnet holder and cell heater.

Finally, I am incredibly grateful to my family whom I do not acknowledge enough: my parents Lesley and Gerald, who have unfailingly supported and encouraged me through all the choices I've made; my brother Adam, who is still my friend after 23 years of having me for an elder brother; and my wife Carmen, whose dedication, trust and love continue to uplift and inspire me.

"Science walks forward on two feet, namely theory and experiment... but continuous progress is only made by the use of both." – Robert A. Millikan

For Carmen

Chapter 1

Introduction

1.1 Nonlinear optics

Photons, the fundamental quanta of light, do not interact with each other in everyday life. An important consequence of this is the ability to transmit information via light over very large distances with little degradation in signal quality. However, photons can interact with each other strongly in nonlinear materials, where the polarisation (i.e. the dipole moment per unit volume) of the material responds non-linearly to the electric field of the light. Most materials exhibit these optical nonlinearities when the incident light has a sufficiently high intensity.

The polarisation $\vec{P}(t)$ of the material system interacting with the electric field $\vec{E}(t)$ of the light can be written as [1]

$$\vec{P}(t) = \epsilon_0[\chi^{(1)}\vec{E}(t) + \chi^{(2)}\vec{E}^2(t) + \chi^{(3)}\vec{E}^3(t) + ... \,], \tag{1.1}$$

where $\chi^{(1)}$ is the linear susceptibility and $\chi^{(2)}$ and $\chi^{(3)}$ are the second- and third-order nonlinear susceptibilities respectively[1]. For low light intensities, only the first term of equation 1.1 is significant and the polarisation of the

[1]Note that $\chi^{(n)}$ are tensors for $n \geq 2$.

medium scales linearly with the electric field strength. As the field strength is increased, nonlinear processes that give rise to the nonlinear susceptibilities [encapsulated in the higher-order terms of equation 1.1], begin to appear. Since the development of lasers in 1960 [2], much higher optical intensities have been accessible and a vast array of nonlinear effects have been explored, with wide-ranging applications from optical frequency conversion [3] to light storage [4] and quantum information processing [5]. In particular, the study of nonlinear phenomena in optically driven *multi-level atomic systems* is a flourishing field of research [6]. For example, electromagnetically induced transparency (EIT) [7, 6], coherent population trapping (CPT) [8] and four-wave mixing (FWM) have been instrumental in the development of atomic clocks [9, 10], magnetometers [11], sub- and super-luminal propagation of light [12, 13].

More recently, advances in nonlinear optics have lead to the relatively new field of quantum nonlinear optics, where nonlinear interactions persist on the level of single photons. One of the prominent ideas to come out of this field is the so-called "quantum internet" [14]. The main idea is that photons act as flying quantum bits (qubits) that transfer quantum-information between the nodes of a network. At the nodes, the photonic qubits can be coherently mapped onto long-lived excitations of stationary media, using nonlinear interactions [15]. The stationary media can exhibit strong interactions that enable rapid quantum logic operations to be performed [16]. For example, single-photon controlled phase gates [17, 18] and CNOT gates [19].

The success of these schemes relies on the development of several key components that include: sources of single photons at frequencies that can be transmitted over long distances in free-space or optical fibres, and well-controlled strongly interacting systems to act as the nodes of the network. Atomic systems are promising candidates on both fronts [20], with the demonstration of high-brightness single-photon sources [21, 22, 23] that are naturally frequency and bandwidth matched to atomic quantum memories [24, 25, 26, 15, 27], and with well-defined optical transitions and long coherence times, providing strong and controllable interactions with photons [4, 28].

1.2 Thermal atomic vapours

The group 1 elements of the periodic table, called the alkali metals, exist in metallic form at room temperature and can be easily stored in glass vacuum cells. The atomic vapour pressure inside the cells is significant at room temperature and scales exponentially with temperature, meaning that very high optical densities can be achieved with relative ease [29]. This is in direct contrast to cold-atom systems, where bulky vacuum chambers and complex laser systems are required to cool and trap atoms. The ability to produce small-scale thermal vapour cells with high optical densities has led to the development of many practical devices including chip-scale atomic clocks [30], brain sensors [31], terahertz detectors [32] and microwave electrometers [33]. Furthermore, scalability is a key requirement of any realisable quantum computer, making thermal vapours a strong candidate for such systems. For example a recent work [34] showed the potential for generating a large number of intensity-squeezed fields by cascading multiple vapour cells.

Of course, thermal atomic vapours are not without issue. The atomic motion at room temperature introduces Doppler-broadening of the absorption lines, which typically exceeds the atomic hyperfine splittings. This makes it difficult to interact with individual atomic states in a controlled manner and can complicate modelling and optimisation of the system. The most commonly used method to improve control over thermal vapour systems is optical pumping, where a strong circularly-polarised laser field is applied to the vapour to drive all of the atoms into a single "dark"-state which is not coupled to the light [35]. While this method can reduce the number of participating atomic energy levels, it is practically challenging to realise in thermal vapours, and typically requires further complexities such as the use of buffer gases and/or anti-relaxation coatings [36, 37] to reduce the effect of state-changing collisions. In addition to this, many applications rely on the use of excited states, where buffer gases lead to significant unwanted broadening.

1.3 The hyperfine Paschen-Back regime

The study of atom-light interactions in magnetic fields began with Michael Faraday in 1845 [38], who observed that the plane of polarisation of light propagating through leaded glass was modified by the application of a magnetic field. This *Faraday effect* is the basis for optical isolators and optical circulators [39] that are used extensively in the telecommunications industry. Recent progress on the quantitative modelling of linear atom-light interactions in magnetic fields [40, 29] has led to significant developments in both fundamental physics, such as the observation of the cooperative lamb shift [13], and novel technologies including: compact optical isolators [41], narrowband atomic filters [42] and self-stabilised diode lasers [43].

Atomic energy levels and transition strengths are extremely sensitive to an externally applied magnetic field, as first observed by Zeeman in 1896 [44]. In magnetic field strengths of the order of 1 T ground state alkali-metal atoms enter the hyperfine Paschen-Back (HPB) regime, where the Zeeman shifts exceed the atomic hyperfine splittings. In this regime each of the transitions can become individually resolved and separately addressable [40, 45], despite the presence of Doppler broadening in thermal vapours. In addition to the high level of control that this brings, the reduced number of states that are simultaneously coupled to the light can greatly simplify spectroscopic measurements in thermal vapours [46, 45, 47, 48].

1.4 Motivation

It is the aim of this investigation to study nonlinear optical effects in a thermal atomic vapour exposed to high magnetic fields. We shall study the effects of EIT, electromagnetically induced absorption (EIA) and FWM. Finally, we will consider spontaneous FWM with a view to single-photon generation. Previous studies of these effects in magnetic fields have focussed primarily on lambda systems, where two long-lived ground states are optically coupled to

a single excited state. Here, we extend these studies to ladder systems, where an relatively short-lived excited state is coupled to a long-lived ground state and an additional excited state. In lambda systems, the wavelengths of the two optical transitions are very close, making separation of the beams difficult, especially in experiments working with single-photon generation. In contrast, the optical wavelengths in ladder systems are sufficiently distinct to employ dichroic beam splitters or narrowband interference filters to easily separate out the light of interest. In lambda systems the optimum signal is usually obtained with co-propagating optical fields, as the atom-light interaction is essentially Doppler insensitive, whereas for ladder systems the most Doppler insensitive signal is obtained with counter-propagating fields. Ladder excitation schemes are currently of significant interest as a means of exciting Rydberg atoms that exhibit long-range interactions [49]. In the case of each of the nonlinear phenomena that we investigate, we will endeavour to quantitatively compare the results of experiments with theoretical models. By doing so we hope to further the understanding of the underlying physics in these complex systems and to discover if the simplifications afforded by the HPB regime extend to nonlinear optical effects.

1.5 Thesis summary

Chapter 2 – A minimal introduction to atom-light interactions in thermal vapours is given. We discuss the atomic structure of rubidium atoms, which are the atom of choice for the experiments in this thesis. We then focus on the effects of an externally applied magnetic field on the atomic structure and absorption spectra.

Chapter 3 – A theoretical model for EIT in a three-level ladder scheme is developed and an experimental investigation of EIT in the HPB regime is presented. We find excellent agreement with the simple model, enabling us to go on to make a direct measurement of the of the rubidium $5P_{3/2} \rightarrow 5D_{5/2}$ transition dipole matrix element in rubidium.

Chapter 4 – We investigate EIA in a three-level ladder scheme. By the addition of a co-propagating coupling laser beam to the EIT set-up, many multi-photon resonances appear. With a resonant coupling field we observe enhanced-absorption. The resultant line-shapes provide an explanation of small structures observed in the EIT spectra of the previous chapter.

Chapter 5 – Seeded FWM in a four-level diamond scheme is studied. We develop a simple four-level theoretical model that finds excellent agreement with the experimentally obtained FWM spectra, even when there is strong laser dressing. We investigate the dependence of the FWM signal on laser detunings, powers and the atomic density of the vapour.

Chapter 6 – We investigate spontaneous FWM as a heralded source of single photons. Experimentally, we observe the appearance of beats in the arrival times of the single-photons which cannot be explained within the framework of conventional quantum beats. We develop a theoretical model that finds excellent agreement with the data and explains the origin of the beats.

Chapter 7 – The important results are summarised and future directions for this research are discussed.

1.6 Publications

The following papers have come out of the work described in this thesis:

D. J. Whiting, J. Keaveney, C. S. Adams, and I. G. Hughes, *Direct measurement of excited-state dipole matrix elements using electromagnetically induced transparency in the hyperfine Paschen-Back regime*, Physical Review A **93**, 043854 (2016), 10.1103/PhysRevA.93.043854.

D. J. Whiting, E. Bimbard, J. Keaveney, M. A. Zentile, C. S. Adams, and I. G. Hughes, *Electromagnetically induced absorption in a nondegenerate three-level ladder system*, Optics Letters **40** 18, 4289 (2015), 10.1364/OL.40.004289.

D. J. Whiting, R. S. Mathew, J. Keaveney, C. S. Adams, and I. G. Hughes, *Four-wave mixing in the hyperfine Paschen-Back regime*, to appear in Journal of Modern Optics arXiv:1705.01855.

D. J. Whiting, N. Šibalić, J. Keaveney, C. S. Adams, and I. G. Hughes, *Single-photon interference due to motion in an atomic collective excitation*, Physical Review Letters **118**, 253601 (2017), 10.1103/PhysRevLett.118.253601.

1.7 Author contributions

D. Whiting carried out the majority of experiments, most of the analysis and contributed to the writing of each paper. J. Keaveney contributed to the experiments for articles one and two and to the writing of each article. E. Bimbard contributed to the experiments and theoretical analysis for, and the writing of, article two. M. A. Zentile contributed to the writing of article two. R. S. Mathew contributed to the experiment for, and the writing of, article three. N. Šibalić assisted with the theoretical analysis for, and the writing of, article three. C. S. Adams contributed to the writing of each article and is the co-investigator for this project. I. G. Hughes contributed to the writing of each article and is the principal investigator for this project.

Chapter 2

Atom-light interactions in magnetic fields

The majority of results presented in this thesis are based upon the interaction of rubidium atoms with coherent optical laser light. In chapters 3 through 5 it will be sufficient to model this interaction by treating the light as a classical electromagnetic field and the atom as a quantised harmonic oscillator. In section 2.1 we present a basic overview of this *semi-classical* model (a more detailed description can be found in e.g. [50]). In section 2.2 we briefly discuss the atomic structure of rubidium atoms and finally, in section 2.3 we discuss modifications to the structure when the atom is placed in an external magnetic field.

In chapter 6 it will become necessary to consider the quantum nature of the light. The appropriate theoretical treatment is presented there.

2.1 The two-level atom

In this section we present a semi-classical description of the interaction between an atom and a coherent light field, beginning with the simplest possible case:

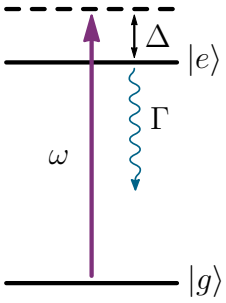

Figure 2.1: The hypothetical two-level atom with an incident optical field of frequency ω detuned by Δ from an electric dipole transition between state $|g\rangle$ and state $|e\rangle$ which has a spontaneous decay rate Γ.

the hypothetical two-level atom (figure 2.1) with ground-state $|g\rangle$ of energy E_g and excited-state $|e\rangle$ of energy E_e, where $E_e - E_g = \hbar\omega_0$.

We describe the state of the atoms using a density matrix formalism [51]. The density matrix of the unperturbed atom is

$$\hat{\rho} = \begin{pmatrix} \rho_{gg} & \rho_{ge} \\ \rho_{eg} & \rho_{ee} \end{pmatrix},$$

where the diagonal elements ρ_{gg} and ρ_{ee} correspond to the populations in the ground and excited states respectively and the off-diagonal elements correspond to coherent superpositions of the ground and excited states.

Consider an incident plane-wave optical field of frequency ω propagating in the z-direction with electric field $\vec{E} = \vec{\epsilon} E_0 \cos(kz - \omega t)$[1], where $\vec{\epsilon}$ is the polarisation vector and $k = 2\pi/\omega$ is the wavenumber. The field couples states $|g\rangle$ and $|e\rangle$ via an electric dipole transition which has the dipole operator

$$\hat{d} = \begin{pmatrix} 0 & \vec{d}_{ge} \\ \vec{d}_{eg} & 0 \end{pmatrix},$$

[1]Since the spatial extent of the atomic wavefunctions are much smaller than the wavelength of the light we can neglect the z dependence of the electric field and write that $\vec{E} = \vec{\epsilon} E_0 \cos(\omega t) = \vec{\epsilon} E_0 (e^{i\omega t} + e^{-i\omega t})/2$ in the region of an atom. This is known as the dipole approximation.

where $\vec{d}_{ij} = \langle i|e\vec{r}|j\rangle$ are the dipole matrix elements with e the electron charge and $\vec{r}$ the displacement vector. We also have that $\vec{d}_{ij} = \vec{d}^{*}_{ji}$ since $\hat{d}$ is a Hermitian operator. The atom-field interaction is then described by the Hamiltonian $\hat{H}_{\text{int}} = -\hat{d} \cdot \vec{E}$.

The time evolution of the density matrix is governed by the von Neumann equation [51]

$$\frac{\mathrm{d}\hat{\rho}}{\mathrm{d}t} = -\frac{\mathrm{i}}{\hbar}[\hat{H}, \hat{\rho}], \tag{2.1}$$

where the total Hamiltonian $\hat{H} = \hat{H}_0 + \hat{H}_{\text{int}}$ is the sum of the interaction Hamiltonian and the unperturbed atomic Hamiltonian

$$\hat{H}_0 = \begin{pmatrix} E_g & 0 \\ 0 & E_e \end{pmatrix}.$$

2.1.1 Rotating frame transformation

The coherent evolution can be completely modelled using the above formalism. However, in order to elucidate some of the effects that will be later discussed, it is useful to make a unitary transformation into a rotating frame, oscillating with the driving field frequency, and to shift the energy scale by the energy of the atomic ground-state. This is accomplished with the unitary operator [52]

$$\hat{U} = \begin{pmatrix} \exp(-\mathrm{i}E_g/\hbar t) & 0 \\ 0 & \exp(-\mathrm{i}\omega t)\exp(-\mathrm{i}E_g/\hbar t) \end{pmatrix},$$

which gives the transformed density matrix

$$\tilde{\rho} = \hat{U}^{\dagger}\hat{\rho}\hat{U} = \begin{pmatrix} \rho_{gg} & \rho_{ge}\exp(-\mathrm{i}\omega t) \\ \rho_{eg}\exp(\mathrm{i}\omega t) & \rho_{ee} \end{pmatrix},$$

and the transformed Hamiltonian

$$\begin{aligned}\tilde{H} &= \hat{U}^\dagger \hat{H} \hat{U} - \mathrm{i}\hbar \hat{U}^\dagger \frac{\mathrm{d}\hat{U}}{\mathrm{d}t} \\ &= \frac{1}{2}\begin{pmatrix} 0 & -\vec{d}_{ge}\cdot\vec{\epsilon}E_0[1+\exp(-2\mathrm{i}\omega t)] \\ -\vec{d}_{eg}\cdot\vec{\epsilon}E_0[1+\exp(+2\mathrm{i}\omega t)] & 2[E_e - E_g - \hbar\omega] \end{pmatrix}.\end{aligned}$$

Note that since this is a unitary transformation ($U^\dagger U = 1$), equation 2.1 is unchanged in the rotating frame. The rapidly oscillating terms in the off-diagonal elements can be neglected since their time dependence averages out over the much slower evolution of the atomic populations. This is called the rotating wave approximation (RWA). Using the definitions for Rabi frequency $\Omega = -\vec{d}_{ge}\cdot\vec{\epsilon}E_0/\hbar$ and detuning $\Delta = \omega - \omega_0$ we have the, now time-independent, Hamiltonian

$$\tilde{H}_{\mathrm{RWA}} = \frac{\hbar}{2}\begin{pmatrix} 0 & \Omega \\ \Omega^* & -2\Delta \end{pmatrix}.$$

2.1.2 Dissipation

The von Neumann equation (equation 2.1) describes the fully coherent evolution of the density matrix, in response to a Hamiltonian. In our case $\tilde{H}_{\mathrm{RWA}}$ describes only the interaction between the atom and the incident single-mode light field but, in practice, the atom can also interact with other electromagnetic field modes in its environment, albeit usually empty ones. This interaction leads to the spontaneous emission of photons, and is the subject of study in chapter 6. Here it is sufficient to say that this interaction introduces decoherence, since we lose information about the system by choosing not to model the entire environment.

The time evolution of the density matrix including these processes is described by the Lindblad master equation [53]

$$\frac{\mathrm{d}\hat{\rho}}{\mathrm{d}t} = -\frac{\mathrm{i}}{\hbar}[\hat{H}, \hat{\rho}] + \hat{L}, \tag{2.2}$$

where $\hat{L}$ contains terms relating to dissipation. Explicitly, $\hat{L}$ can be constructed as $\hat{L} = \sum_n [2\hat{C}_n\hat{\rho}\hat{C}_n^\dagger - (\hat{\rho}\hat{C}_n^\dagger\hat{C}_n + \hat{C}_n^\dagger\hat{C}_n\hat{\rho})]/2$, where $\hat{C}_n = \sqrt{\gamma_n}\hat{A}_n$ are the collapse operators, and $\hat{A}_n$ are the operators through which the environment couples to the system with rates γ_n.

In the case of the two-level atom (figure 2.1) the collapse operator for spontaneous decay from the excited state, with lifetime $\tau = 1/\Gamma$, to the ground state is $\hat{C} = \sqrt{\Gamma}|g\rangle\langle e|$.

2.1.3 Relating microscopic and macroscopic properties

It is common to relate the microscopic and macroscopic properties of the atomic vapour via the polarisation density [54]. For an isotropic medium the polarisation density is given by the number density of dipoles N multiplied by the expectation value of the dipole operator

$$\vec{P} = N\langle\hat{d}\rangle = \mathrm{Tr}[\hat{\rho}\hat{d}]N = N(\vec{d}_{ge}\tilde{\rho}_{eg}e^{-\mathrm{i}\omega t} + \text{c.c.}). \tag{2.3}$$

We can also write the polarization of the macroscopic medium as

$$\vec{P} = \epsilon_0\chi(\omega)\vec{E} = \frac{1}{2}\epsilon_0\vec{E}(\chi e^{-\mathrm{i}\omega t} + \text{c.c.}), \tag{2.4}$$

where χ is the electric *susceptibility* of the medium. The susceptibility is frequency dependent and complex; the real part describes the dispersive properties of the medium while the imaginary part describes its absorptive properties. Equating equations 2.3 and 2.4 the susceptibility can be written in terms of microscopic quantities as

$$\chi(\omega) = -\frac{2|\vec{d}_{ge}|^2}{\hbar\epsilon_0}\frac{\tilde{\rho}_{eg}}{\Omega^*}N.$$

The refractive index of the medium is related to the susceptibility by $n = \sqrt{1+\chi}$. In a medium of refractive index n the propagation of the electric field is modified. In terms of the real and imaginary parts of the refractive index

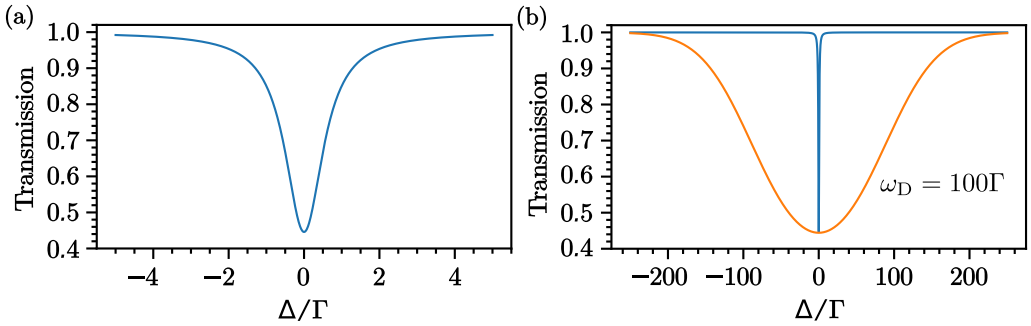

Figure 2.2: Transmission profiles of a weak laser beam through ensembles of 2-level atoms. (a) A typical Lorentzian line shape for cold atomic ensembles. The width is determined by the spontaneous decay rate from the excited state, Γ. (b) In a room temperature (20 °C) atomic ensemble, motion results in the Doppler-broadening of the Lorenzian (blue) into the Voigt line shape (orange). For room temperature alkali-metal atoms the Doppler-broadened width is much larger than Γ.

$(n = n_\mathrm{R} + \mathrm{i}n_\mathrm{I})$ we can write the electric field as $\hat{E}(z) = \hat{\epsilon}E_0 e^{\mathrm{i}(n_\mathrm{R}kz-\omega t)}e^{-kn_\mathrm{I}z}$ where a positive n_I leads to an exponentially decaying amplitude describing extinction of the field.

Calculating the steady-state value of ρ_{eg} using equation 2.2 and taking the limit of $\tilde{\rho}_{eg}/\Omega^*$ as $\Omega \to 0$, i.e. in the limit of a weak incident electric field, we find that

$$\lim_{\Omega\to 0}\frac{\tilde{\rho}_{eg}}{\Omega^*} = \frac{1}{2\Delta + \mathrm{i}\Gamma}. \tag{2.5}$$

In this limit, known as the weak-probe regime [55], the susceptibility and refractive index are independent of the incident electric field strength. Thus the transmitted intensity through a slab of material of thickness l can be written as $T = \exp(-\alpha l)$ where the so-called absorption coefficient α depends linearly on the imaginary part of the refractive index $\alpha = 2kn_\mathrm{I}$. Figure 2.2(a) shows an example theoretical transmission spectrum as a weak field (called the *probe*) is tuned through resonance. The absorption line displays the characteristic Lorentzian line-shape of equation 2.5 with a full width at half maximum of Γ.

2.1.4 Doppler broadening

So far we have only considered the interaction of light with stationary atoms. For the experiments described in this thesis, the atoms are in the vapour phase and are assumed to be in thermal equilibrium with the Pyrex vapour cell windows[2]. In this case the distribution of atom velocities is the Maxwell-Boltzmann velocity distribution. The partial distribution for v_z, the velocity component in the z direction, is $p(v_z) = \exp(-v_z^2/u^2)/(u\sqrt{\pi})$ where $u = \sqrt{2k_{\mathrm{B}}T/m}$ is the characteristic width of the distribution, k_{B} is the Boltzmann constant, T is the vapour temperature and m is the atomic mass. For ^{87}Rb atoms at a temperature of 20 °C we have $u = 236$ ms^{-1}. For an applied laser field directed along z, moving atoms experience a Doppler shifted light frequency $\omega' = \omega - kv_z$. Thus, a laser detuned by Δ in the laboratory frame interacts resonantly with atoms moving at $v_z = \Delta/k$.

The total susceptibility of the medium is given by the sum over all velocities weighted by $p(v_z)$. In a two-level system interacting with a single optical field this leads to a broadening of the spectral lines with a characteristic *Doppler width* of $\omega_{\mathrm{D}} = ku$. Typically in hot atomic vapours this width is much larger than the *natural linewidth* of the transition Γ. For example the ^{87}Rb D_2 transition with $k = 2\pi/780$ nm and a temperature of 20 °C has $\omega_{\mathrm{D}}/2\pi = 303$ MHz compared with the natural linewidth of $\Gamma/2\pi = 6$ MHz [56]. In figure 2.2(b) we show the theoretical probe transmission spectra with and without Doppler broadening for $u = 100\Gamma$. In this case the line shape takes the form of a Voigt function [54], which resembles a Gaussian at small detunings ($\Delta << \omega_{\mathrm{D}}$) and a Lorentzian at large detunings ($\Delta >> \omega_{\mathrm{D}}$).

With increasing numbers of levels and fields, the Doppler effect plays a more complex role, leading to effects such as velocity selective optical pumping [57] and multi-photon resonances (chapter 4).

[2]This assumption may break down if anti-relaxation coatings are used.

2.2 Rubidium atomic structure

In this section we briefly discuss the electronic structure of rubidium atoms that is relevant to understanding the experiments contained within this thesis. Rubidium is an alkali-metal atom with a single valence electron; its electronic structure is similar to that of hydrogen atoms. Naturally occurring rubidium has two isotopes; ^{85}Rb (72.2%) with nuclear spin $I = 5/2$ and ^{87}Rb (27.8%) with nuclear spin $I = 3/2$. A detailed analysis of the structure of alkali-metal atoms can be found in most atomic physics text books (e.g. [58]) but for the sake of completeness we list a few of the key results here.

A schematic diagram of the electronic energy level structure of ^{87}Rb atoms is shown in figure 2.3. The gross structure is determined by the principal quantum number and the orbital angular momentum of the electron. The electron orbital angular momentum $\vec{L}$ couples to the electron spin $\vec{S}$ (LS-coupling) which results in fine structure splitting. The new energy eigenstates, with spin-orbit angular momenta $\vec{J} = \vec{L}+\vec{S}$, are well identified by the quantum number $J = |\vec{J}|$, along with the projection of $\vec{J}$ onto the quantization axis, m_J. The electron spin-orbit angular momentum $\vec{J}$ further couples to the nuclear spin of the atom $\vec{I}$, resulting in hyperfine structure splitting. The new energy eigenstates, with total angular momenta $\vec{F} = \vec{J} + \vec{I}$, are well identified by the quantum number $F = |\vec{F}|$, along with the projection of $\vec{F}$ onto the quantization axis, m_F.

In the absence of external electric or magnetic fields the atomic structure is well described by the above formulation. The weak probe transmission spectrum of the ^{87}Rb D_2 line ($5S_{1/2} \rightarrow 5P_{3/2}$) in a 7.5 cm vapour cell at room temperature (20 C), calculated using the ElecSus program [29], is shown in figure 2.4(a). The two absorption lines correspond to transitions from each of the two ground-states ($F = 1, 2$) which are separated in frequency by 6.83 GHz. The excited state hyperfine structure is smaller than the Doppler width and is therefore unresolved. We now go on the discuss the effect of an external magnetic field being applied to the atoms.

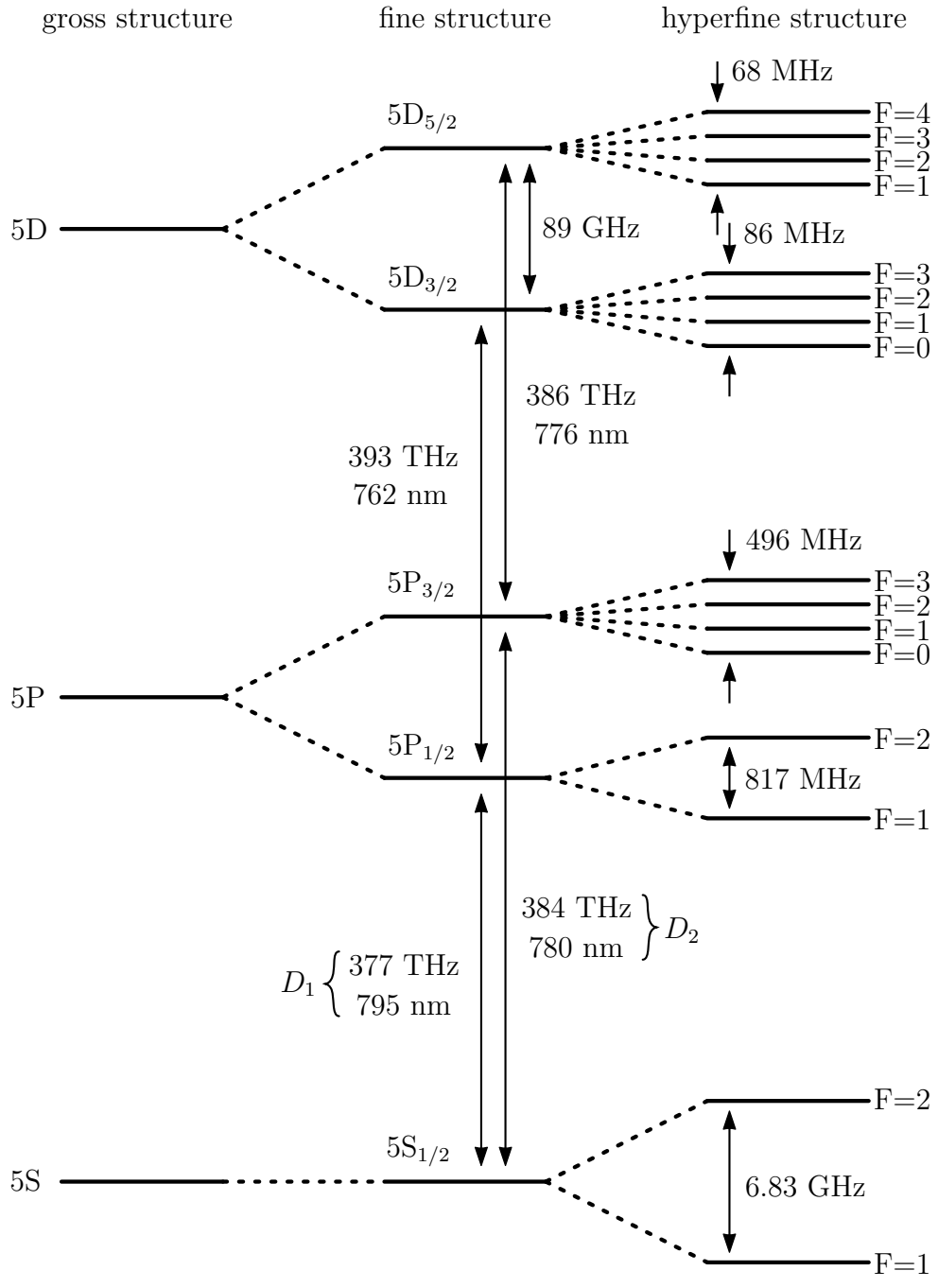

Figure 2.3: Schematic diagram of the ^{87}Rb atomic structure relevant to the experiments in this thesis.

2.3 The hyperfine Paschen-Back regime

The atomic energy levels shift in response to an applied magnetic field $\vec{B}$ (the Zeeman effect). This is due to a coupling of the field to the electron orbital motion, to the electron spin and to the nuclear spin, which is formally described by the Hamiltonian [58]

$$\hat{H}_B = -\frac{\mu_\mathrm{B}}{\hbar}(g_L\vec{L} + g_S\vec{S} + \frac{m_\mathrm{e}}{m_\mathrm{p}}g_I\vec{I}) \cdot \vec{B},$$

where μ_B is the Bohr magneton, $m_\mathrm{e,p}$ are the electron and proton rest masses and $g_{L,S,I}$ are the angular momentum g-factors. At small field strengths, the interaction is weaker than the hyperfine interaction[3] and the energy level shift is proportional to the magnetic field strength B, $\Delta E = g_F m_F \mu_\mathrm{B} B$, where g_F is the Landè g-factor for F [59]; this is known as the hyperfine linear Zeeman regime. As the field strength increases, the coupling to the external field becomes similar in strength to the hyperfine interaction. In this regime it is often said that there are "no good quantum numbers" which means that the relevant eigenstates cannot be described by a single S, L, I, J or F quantum number and its projection m. At even larger fields, the nuclear spin and spin-orbit angular momenta decouple, since individually they couple more strongly to the field than to each other. In this *hyperfine Paschen-Back* (HPB) regime [58] the energy levels again shift linearly with the applied field but now according to $\Delta E = g_J m_J \mu_\mathrm{B} B$, where g_J is the Landè g-factor for J. At still larger fields, where the Zeeman interaction exceeds the fine structure splitting, one enters the Paschen-Back regime[4]. For the states and field strengths considered in this thesis, the maximum Zeeman shift is around one third of the fine structure splitting so this last regime need not be further discussed.

Figure 2.4(d) shows the shift of the energy levels in the ground and excited

[3] For the ^{87}Rb $5S_{1/2}$ state the Zeeman and hyperfine interaction strengths are approximately equal in a field of strength 0.24 T.

[4] For the ^{87}Rb $5P_{1/2}$ and $5P_{3/2}$ states this requires a field strength of more than 170 T. For the $5D_{3/2}$ and $5D_{5/2}$ states the field strength would have to be more than 1.3 T.

manifolds of the ^{87}Rb D_2 line as a function of applied B-field up to a maximum field strength of 0.6 T. In zero magnetic field the m_F states are degenerate, the atom having no preferred orientation in space (quantisation axis). The $F = 1, 2$ branches of the ground-state ($5S_{1/2}$) can be clearly seen whereas the hyperfine intervals in the excited state are smaller and cannot be seen on the scale of the plot. In the low-field linear Zeeman regime, the degeneracy of the m_F states is lifted, with the magnetic field vector establishing a quantisation axis. In the ground-state the HPB regime is reached at a field strength of 0.24 T. Here, $J = 1/2$ and there are two branches of states defined by their magnetic spin-orbit quantum numbers $m_J = \pm 1/2$, each of which contain $2I + 1 = 4$ states with $m_I = \pm 1/2, \pm 3/2$ that are separated by the hyperfine interaction energy. The Landè g-factor $g_J = 2$ so that the states with $m_J = \pm 1/2$ shift linearly by ± 14.0 GHz/T respectively in the applied field. For B=0.6 T, the interaction of the ground state with the field is not large enough to completely decouple the spin-orbit and nuclear spin angular momenta. On the right hand side of figure 3.5 we write the $5S_{1/2}$ eigenstates in the uncoupled basis, $|m_J, m_I\rangle$, which show clearly (in blue) the small remaining fraction of hyperfine mixing. In the excited state ($5P_{3/2}$) the hyperfine interaction is significantly weaker and the HPB regime is reached at a field strength of just 15 mT. Here, $J = 3/2$ and there are four branches of states defined by $m_J = -3/2, -1/2, 1/2, 3/2$. The Landè g-factor $g_J = 4/3$ which gives a shift of ± 28.0 GHz/T for the stretched (maximal values of $|m_J|$) states $m_J = \pm 3/2$ respectively. For B=0.6 T we are very far into the HPB regime and any residual hyperfine mixing is negligible. For this reason we choose not to write out the full state decomposition.

Through the shifting of energy levels and the modification of the hyperfine coupling, the Zeeman interaction changes the transition frequencies and line strengths. The modified weak probe transmission spectrum is shown in figure 2.4(a,b,c) for different magnetic field strengths (indicated on the right hand side). Notice that the probe detuning axes have different scales to accommodate the large line shifts in the high magnetic field regime. In (a) the Doppler broadening masks the hyperfine structure in the excited state.

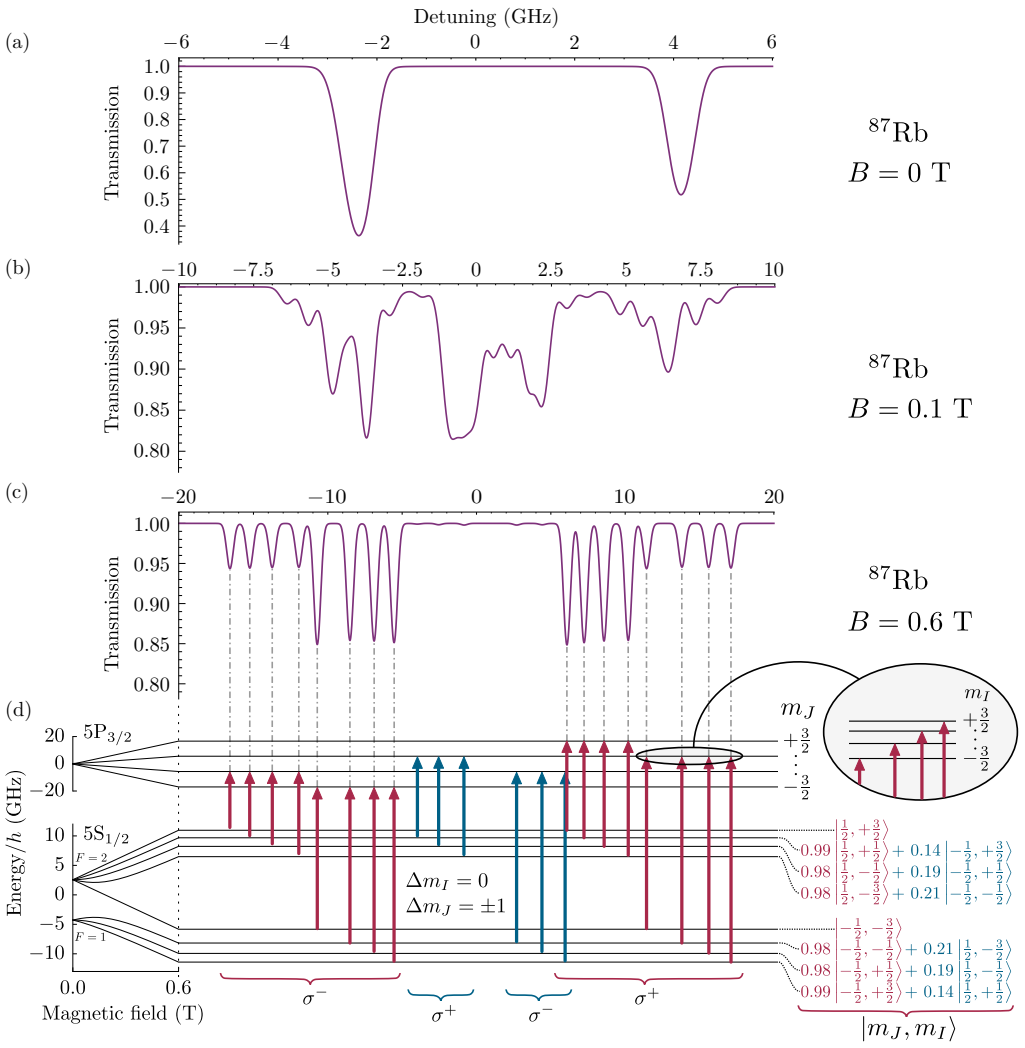

Figure 2.4: Theoretical transmission spectra for the ^{87}Rb D_2 line in different magnetic field regimes. (a) In zero external B-field there are two absorption lines corresponding to the two hyperfine ground-states $F = 1, 2$. Three transitions ($F \to F'$, $F \to F' - 1$, $F \to F' + 1$) are unresolved within each of the Doppler-broadened lines. (b) In intermediate B-fields many of the transitions are partially resolved but identifying individual lines is tricky. (c) In the HPB regime all the transitions are well resolved and can be easily identified. (d) On the left the splitting of the D_2 line energy levels is shown as a function of B-field. In the HPB regime arrows are used to indicate the individual transitions in (c). On the right we display the $5S_{1/2}$ state decomposition in the $|m_J, m_I\rangle$ basis. Residual hyperfine mixing results in the small mixed fractions of the states (shown in blue) which correspond to the transitions with blue arrows.

In (b) the excited state is already in the HPB regime but the ground state is not. Many of the transitions become partially resolved but identifying individual lines and understanding the relative line-strengths is tricky. Finally, in (c) which corresponds to the HPB regime for both ground and excited states, the lines become fully resolved and the spectrum shows a symmetry about zero detuning. Each of the observed absorption lines can be mapped onto the individual transitions indicated by the vertical arrows in (d). Note that transitions between states with different m_I are not dipole coupled. In this example the probe field propagates along the magnetic field vector[5] and therefore $\sigma_\pm$ ($\Delta m_J = \pm 1$) transitions are driven by the left and right circular components of the probe polarisation. Here, the probe is linearly polarised, i.e. containing equal quantities of left- and right-circular polarisation. Apart from the weak transitions indicated by the blue coloured arrows, the negative detuning part of the spectrum contains σ_- transitions and the positive part σ_+ transitions. Since the probe is linearly polarised, both sets of absorption lines have equal depth. The weak transitions in the centre of the spectrum are the result of the residual hyperfine mixing in the ground state manifold. Their line-strength therefore decreases with increasing B. For more information the reader is referred to [60] where these transitions and the dependence of their line strengths on magnetic field have been investigated in detail. Finally, we note that in addition to being fully resolved, the transition between the stretched states $m_J = 1/2 \rightarrow 3/2$ and $m_J = -1/2 \rightarrow -3/2$ are closed, i.e. the only decay is to the original ground-state, making these the text-book 2-level systems.

2.4 Summary

In summary we have presented a semi-classical model for the electric susceptibility of a thermal vapour of 2-level atoms interacting with coherent radiation

[5] By choosing a non-zero angle between the probe and magnetic-field vectors, one could also drive π ($\Delta m_J = 0$) transitions since this requires that the electric field polarisation has some component pointing along $\vec{B}$.

such as that produced by a laser. We have discussed the atomic structure and spectra of the rubidium D_2 line and shown how it is modified under the application of magnetic fields. In particular we discussed the theoretical probe transmission spectra in the HPB regime, showing how individual two-level systems can be resolved and easily identified. In the following chapter we increase the model's complexity to allow for three atomic-levels coupled by two optical fields. In this new system we investigate the nonlinear phenomenon of EIT, whilst in the HPB regime.

Chapter 3

Electromagnetically induced transparency (EIT)

This chapter is based on the following publication:

D. J. Whiting, J. Keaveney, C. S. Adams, and I. G. Hughes, *Direct measurement of excited-state dipole matrix elements using electromagnetically induced transparency in the hyperfine Paschen-Back regime*, Physical Review A **93**, 043854 (2016), 10.1103/PhysRevA.93.043854.

3.1 Introduction

Laser-induced coherence of atomic states can lead to interference between the excitation pathways that control a medium's optical response. This can be used to eliminate the absorption at the resonant frequency of a transition, an effect known as electromagnetically induced transparency (EIT) [61]. Since the first observation of EIT in a strontium vapour [62], the effect has been investigated in a wide variety of atoms and level-schemes. A review of the subject is presented in [6].

Historically, the primary interest in EIT stemmed from the fact that it

generates an enhanced nonlinear susceptibility in a spectral region associated with induced transparency. This fulfils the requirements for efficient wave-mixing [61] and is the basis for all-optical switching [63] protocols. In Rydberg EIT [64], where coherence is induced between an atomic ground-state and a highly excited (Rydberg) state, the strong atom-atom interactions can lead to an optical nonlinearity that is strong on a single-photon level. These atom-mediated photon-photon interactions can be used for nonclassical light generation and quantum gate protocols [65, 66]. Associated with the increase in transmission is a change in the medium's dispersive properties, dramatically reducing the group-velocity on resonance. A reduction in the group-velocity results in a slowing of optical pulses that propagate through the medium. This effect is known as slow-light, with propagation speeds as low as 8 m/s having been observed in thermal atomic vapours [67]. If the coupling field is switched off whilst the pulse is propagating through the medium, the pulse can even be stored for lengths of time in excess of 1 ms, before being coherently retrieved by switching the coupling field back on [68, 69].

For applications involving precision measurement or optimisation of devices, it is imperative to obtain an accurate quantitative understanding of the relevant physical phenomena. Accurate quantitative modelling of nonlinear optical effects, such as EIT, remains difficult for atomic thermal vapours due to the unresolved hyperfine structure [70]. This is in contrast to linear optical phenomena (e.g. absorption, Faraday rotation) where there has been significant recent progress in quantitative modelling, both in terms of fundamental physics and applications [13, 40, 41, 42, 29]. A recent experiment [45] demonstrated that applying a large magnetic field can greatly simplify spectroscopic measurements by separating out individually-addressable two-level systems. In this chapter we investigate whether this simplification can be extended to three-level systems, to allow for accurate modelling of EIT spectra.

Previous investigations of EIT in magnetic fields have led to the development of sensitive magnetometers [71, 11]. The steep dispersion profiles obtainable with EIT mean that small variations in frequency equate to large changes of

refractive index. Thus, these devices can be highly sensitive to the Zeeman shifts induced by a magnetic field. Usually these devices operate in the linear Zeeman regime, where the Zeeman shift is much smaller than the hyperfine structure splittings of the atom. In large magnetic fields (the HPB regime), studies of EIT have been limited to Λ systems [72], where two long-lived ground states are coupled via a short lived intermediate state. We extend this work by investigating a ladder system, which is relevant for many schemes involving highly excited states such as Rydberg EIT [64] and four-wave mixing [73, 74, 75].

3.2 Theoretical model

One of the main aims of this chapter is to investigate whether, by applying a strong magnetic field, one can individually address three-level systems in a thermal atomic vapour, thereby enabling quantitative modelling of EIT spectra. We therefore begin by presenting a theoretical semi-classical description of a thermal vapour of three-level atoms interacting with two continuous-wave driving fields.

3.2.1 The three-level atom

We consider the three-level ladder-system shown in figure 3.1. Following the methods introduced in section 2.1 we arrive at the Hamiltonian for the system (in the rotating wave approximation),

$$\hat{H} = \frac{\hbar}{2}\begin{pmatrix} 0 & \Omega_\mathrm{p} & 0 \\ \Omega_\mathrm{p}^* & -2\Delta_\mathrm{p} & \Omega_\mathrm{c} \\ 0 & \Omega_\mathrm{c}^* & -2\delta \end{pmatrix}, \tag{3.1}$$

where $\Omega_\mathrm{p}, \Omega_\mathrm{c}$ are the pump and coupling Rabi frequencies and $\delta = \Delta_\mathrm{p} + \Delta_\mathrm{c}$ is the two-photon detuning with $\Delta_\mathrm{p}, \Delta_\mathrm{c}$ being the pump and coupling detunings respectively. In the weak probe limit (as $\Omega_\mathrm{p} \to 0$) the eigenstates of this

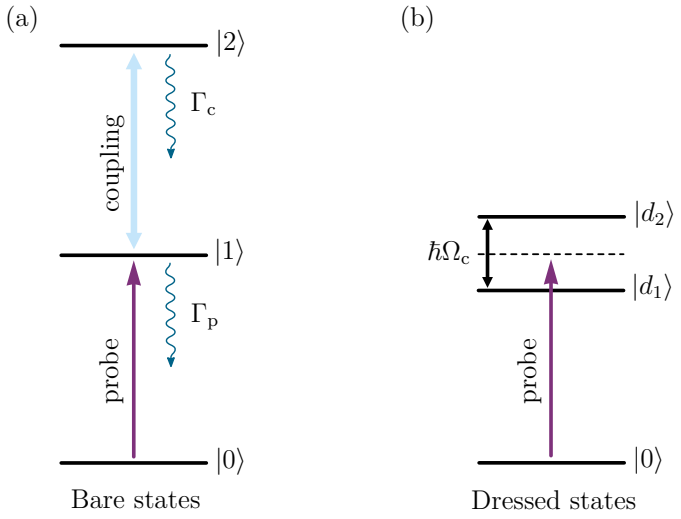

Figure 3.1: The three-level ladder-system depicted in the atom-only eigen-basis (bare states) and in the atom + light eigen-basis (dressed states). Here, the dressed states are depicted in a reference frame rotating at the coupling field frequency. In the dressed state picture, destructive interference between excitation to $|d_1\rangle$ and $|d_2\rangle$ results in transparency for the probe field.

Hamiltonian are $|0\rangle$ and

$$|d_{1,2}\rangle = |2\rangle + \frac{\Delta_c \mp \sqrt{\Delta_c^2 + \Omega_c^2}}{\Omega_c}|1\rangle$$

with corresponding eigenvalues (energies) $E = 0$ and

$$E = -\frac{\hbar}{2}\left(2\Delta_p + \Delta_c \pm \sqrt{\Delta_c^2 + \Omega_c^2}\right). \tag{3.2}$$

These are often referred to as the dressed states since the atomic (bare) states have been modified ("dressed") by the strong coupling field. The energy shift of states $|1\rangle$ and $|2\rangle$ due to the coupling field is known as the AC Stark shift [76].

The dressed-state picture provides an intuitive explanation for EIT. For resonant probe and coupling fields $\Delta_p = \Delta_c = 0$ the dressed states $|d_{1,2}\rangle = \frac{1}{\sqrt{2}}(|2\rangle \mp |1\rangle)$ are split in energy by $\hbar\Omega_c$ [figure 3.1(b)]. This splitting of the

dressed states is referred to as Autler-Townes splitting [76]. The probability amplitudes for excitation to the dressed states via the dipole transition $|0\rangle \rightarrow |1\rangle$ are equal but exactly out of phase and therefore cancel, resulting in transparency for the probe field.

Although it is possible to find an analytic solution for the steady state of the density matrix for arbitrary Ω_p, using symbolic mathematics software packages, the equations are too unwieldy to display here. In the weak probe limit, the resulting probe transition coherence simplifies to [77]

$$\frac{\rho_{10}}{\Omega_\mathrm{p}} = \frac{1}{2\Delta_\mathrm{p} + \mathrm{i}\Gamma_\mathrm{p} - \dfrac{\Omega_\mathrm{c}^2}{2\delta + \mathrm{i}\Gamma_\mathrm{c}}}, \tag{3.3}$$

where Γ_c is the decay rate of state $|2\rangle$. For $\Omega_\mathrm{c} = 0$ we return to the solution for a 2-level system (equation 2.5). In the case of resonant probe and coupling fields ($\Delta_\mathrm{p} = \Delta_\mathrm{c} = 0$) the absorption coefficient on the probe transition

$$\alpha = 2k_\mathrm{p} n_\mathrm{I} \approx \frac{2k_\mathrm{p}|\vec{d}_{01}|^2 N}{\hbar\epsilon_0} \frac{1}{1 + \dfrac{\Omega_\mathrm{c}^2}{\Gamma_\mathrm{c}\Gamma_\mathrm{p}}},$$

where the approximation is that $n_\mathrm{I} = \mathrm{Im}[\sqrt{1+\chi}] \approx \chi_\mathrm{I}/2$, which is true for $\chi \ll 1$. Keaveney et al. [78] have shown that for a high density Rb vapour $\chi_\mathrm{max} = 0.3$ and so this approximation is valid within the context of this discussion. From this it is clear that there is a significant transparency induced for the probe field when $\Omega_\mathrm{c}^2/\Gamma_\mathrm{c}\Gamma_\mathrm{p} > 1$. Theoretical probe transmission lineshapes based on equation 3.3, with $\Gamma_\mathrm{c} = 0.1\Gamma_\mathrm{p}$, are shown for a range of coupling-field Rabi frequencies in figure 3.2.

3.2.2 Doppler broadened EIT

Up to this point we have neglected the atomic velocity distribution in the modelling of the lineshapes. We now include this in the same way as in

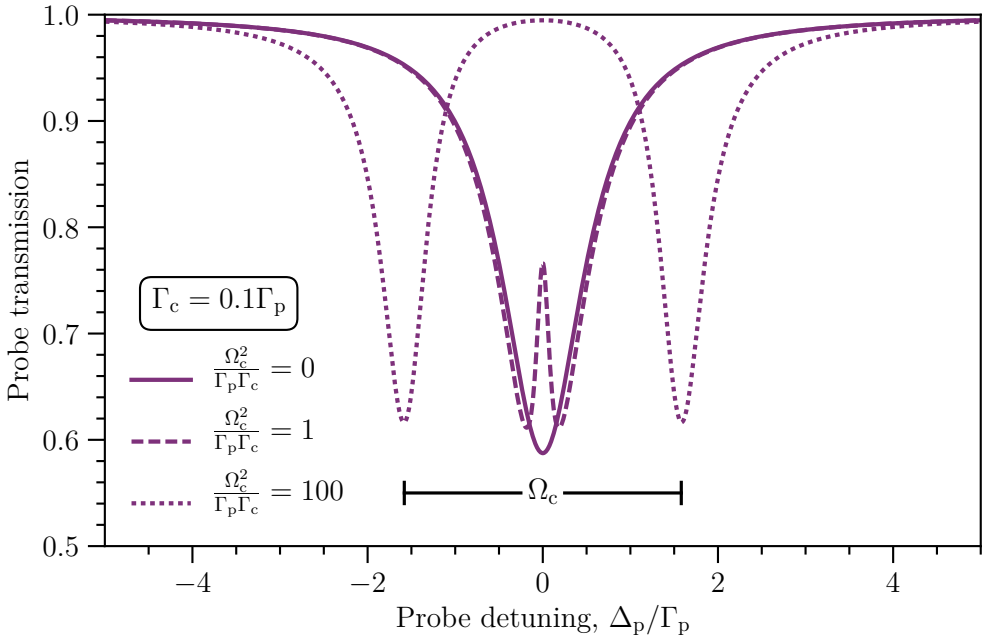

Figure 3.2: Theoretical weak-probe transmission spectra of a cold atomic gas. As a strong coupling field is applied, the initially Lorentzian absorption line (solid line) develops a resonant transparency (dashed line). With a much stronger coupling field the absorption line is completely split into an Autler-Townes doublet (dotted line) with a splitting equal to the coupling Rabi frequency and almost complete transparency at zero probe detuning.

section 2.1, i.e. by integrating the susceptibility over all velocity classes weighted by the Maxwell-Boltzmann distribution. In this case the atomic motion results in Doppler shifted detunings for both probe and coupling fields: $\Delta'_{\rm p} = \Delta_{\rm p} - \vec{k_{\rm p}} \cdot \vec{v}$ and $\Delta'_{\rm c} = \Delta_{\rm c} - \vec{k_{\rm c}} \cdot \vec{v}$ where $\vec{k_{\rm p}}, \vec{k_{\rm c}}$ are the probe and coupling field wave-vectors and $\vec{v}$ is the atom velocity. In general the angle between the two beams can be arbitrary but here we limit our discussion to the two special cases that are most relevant to the experiments presented in this thesis: exactly co- and counter-propagating beams.

For a counter-propagating coupling field, the Doppler shifted two-photon detuning $\delta(v_z) = \delta - (k_{\rm p} - k_{\rm c})v_z$, where $k_{\rm p}$ and $k_{\rm c}$ are the probe and coupling field wavenumbers respectively. In the rubidium ladder scheme with transitions $5S_{1/2} \rightarrow 5P_{3/2} \rightarrow 5D_{5/2}$ we have $k_{\rm p} = 2\pi/780$ nm and $k_{\rm c} = 2\pi/776$ nm. Since $k_{\rm p} \approx k_{\rm c}$ we have that $\delta(v_z)$ is almost independent of the atomic motion. We therefore refer to this as the *Doppler-free* configuration. In the case of a co-propagating coupling field, the Doppler shifted two-photon detuning $\delta(v_z) = \delta - (k_{\rm p} + k_{\rm c})v_z$ depends strongly on the velocity. We refer to this as the *Doppler-selective* configuration. Figure 3.3(a) shows the imaginary component of the refractive index on the probe transition (proportional to the absorption coefficient) for the different velocity classes of the medium, along with the resulting absorption lineshape in each of the above configurations.

In the limit of a weak coupling field, there is no dressing of the atomic states. In this case the one-photon absorption resonance will occur for atoms moving with $k_{\rm p}v_z = \Delta_{\rm p}$. The two-photon absorption resonances, between probe and co- or counter-propagating coupling fields, will occur for atoms moving with $k_{\rm p}v_z = \delta k_{\rm p}/(k_{\rm p} \pm k_{\rm c})$ respectively. These conditions are plotted as dashed lines in the velocity maps of figure 3.3. To determine the conditions for probe absorption resonances in the presence of dressing we need to consider the dressed-state energies (equation 3.2). A probe absorption resonance occurs when the probe field is resonant with the $|0\rangle \rightarrow |d_{1,2}\rangle$ transition. In the rotating reference frame, this occurs when the energies of the dressed states $|d_{1,2}\rangle$ are equal to the ground-state energy, i.e. $0 = -\hbar/2(2\Delta_{\rm p} + \Delta_{\rm c} \pm \sqrt{\Delta_{\rm c}^2 + \Omega_{\rm c}^2})$

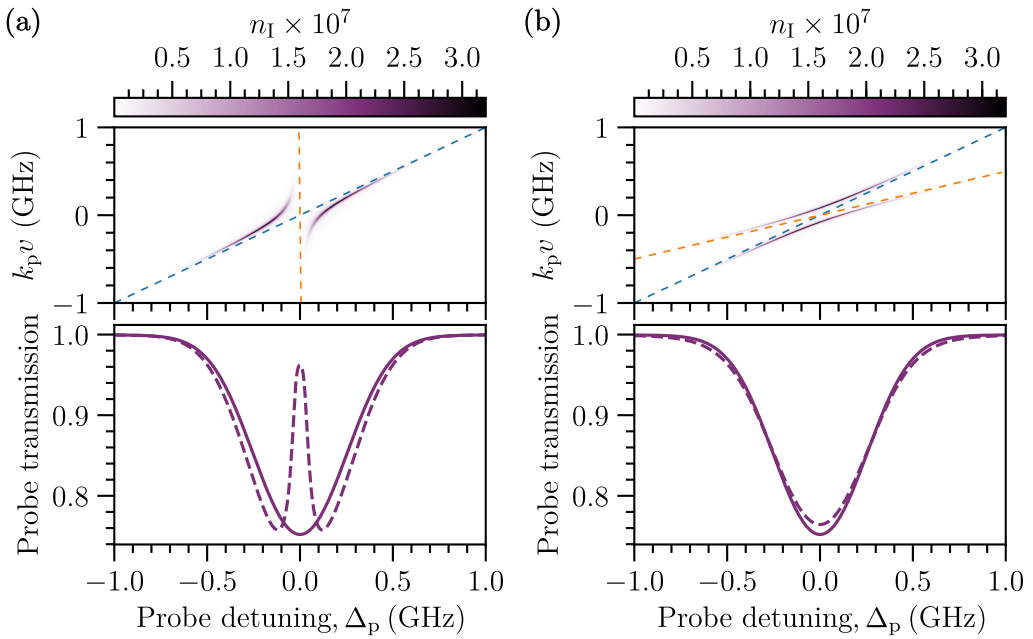

Figure 3.3: Theoretical EIT in a thermal atomic vapour with a resonant coupling field in Doppler-free (a) and Doppler-selective (b) geometries. The imaginary component of the medium refractive index is shown for different velocity classes (top). The probe resonance condition ($k_p v_z = \Delta_p$) is shown by the dashed blue lines and the two-photon resonance condition [$(k_p \pm k_c)v_z = \Delta_p$] is shown by the dashed orange lines. The transmission profile of a weak probe field (bottom) depends on the sum of all velocity classes. The imaginary component of the refractive index exhibits avoided crossings, with the special case of symmetric Autler-Townes splitting for $v_z = 0$. The avoided crossing leads to the formation of a transparency window in (a).

which is true for

$$\Delta_{\mathrm{p}}^2 + \Delta_{\mathrm{c}}\Delta_{\mathrm{p}} = \frac{\Omega_{\mathrm{c}}^2}{4}.$$

Thus for atoms with $v_z = 0$ the probe absorption resonances occur for $\Delta_{\mathrm{p}} = -\frac{1}{2}(\Delta_{\mathrm{c}} \pm \sqrt{\Delta_{\mathrm{c}}^2 + \Omega_{\mathrm{c}}^2})$. For a resonant coupling field ($\Delta_{\mathrm{c}} = 0$) the resonances occur for $\Delta_{\mathrm{p}} = \pm\Omega_{\mathrm{c}}/2$, i.e. the Autler-Townes splitting is observed in the probe transmission spectrum. Including the Doppler shift $\Delta_{\mathrm{p,c}} \to \Delta_{\mathrm{p,c}} - k_{\mathrm{p,c}}v_z$ we can write that

$$k_{\mathrm{p}}(k_{\mathrm{p}} + k_{\mathrm{c}})v_z^2 - (2k_{\mathrm{p}}\Delta_{\mathrm{p}} + k_{\mathrm{c}}\Delta_{\mathrm{p}} + k_{\mathrm{p}}\Delta_{\mathrm{c}})v_z + \Delta_{\mathrm{p}}(\Delta_{\mathrm{p}} + \Delta_{\mathrm{c}}) = \frac{\Omega_{\mathrm{c}}^2}{4} \tag{3.4}$$

which can be solved to find the resonant velocity classes

$$k_{\mathrm{p}}v_z = \frac{(2k_{\mathrm{p}} + k_{\mathrm{c}})\Delta_{\mathrm{p}} + k_{\mathrm{p}}\Delta_{\mathrm{c}} \pm \sqrt{(k_{\mathrm{c}}\Delta_{\mathrm{p}} - k_{\mathrm{p}}\Delta_{\mathrm{c}})^2 + k_{\mathrm{p}}(k_{\mathrm{p}} + k_{\mathrm{c}})\Omega_{\mathrm{c}}^2}}{2(k_{\mathrm{p}} + k_{\mathrm{c}})}. \tag{3.5}$$

In figure 3.3(a) we see that the Doppler-free geometry results in a narrow transparency window and a line shape resembling the result for stationary (cold) atoms (figure 3.2). However, from the velocity-map we observe that fast-moving atoms lead to absorption at small detunings, which can be understood as follows: The moving atoms are Doppler shifted out of resonance with the coupling field, reducing the AC Stark shift, and giving rise to an asymmetry in the dressed states. This increases the absorption at the edges of the transparency window, leading to an effective narrowing of the transparency window. This narrowing means that to observe a similar level of transparency, the coupling Rabi frequency must be significantly larger in a thermal vapour than in a cold atomic gas.

In figure 3.3(b) we see that the Doppler-sensitive geometry results in only a small and broad reduction in probe absorption. Although the probe transmission spectrum is only marginally modified by the addition of the coupling field, the distribution of the excited atoms amongst the velocity classes is changed dramatically. With only a resonant probe field, atoms with $v_z = 0$ are excited. With the addition of the coupling field, a resonant probe field simultaneously

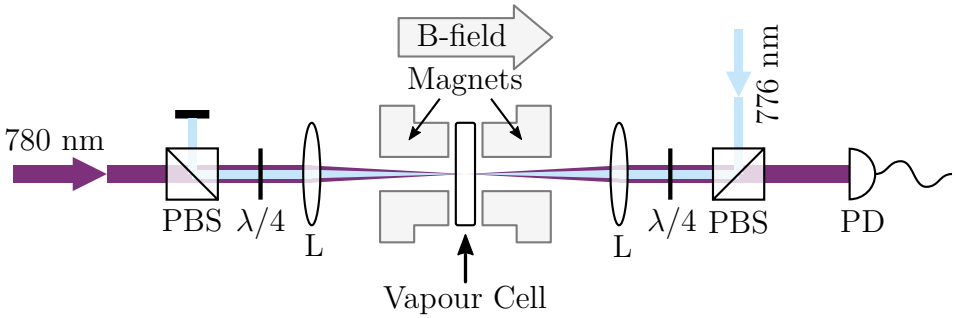

Figure 3.4: Schematic of the experimental apparatus. PBS - Polarizing beam splitter; $\lambda/4$ - quarter waveplate; L - lens with 200 mm focal length; Vapour Cell - 2 mm ^{87}Rb vapour cell; PD - high-gain photodetector.

excites two groups of atoms with velocities $k_{\mathrm{p}}v_z = \pm\frac{\Omega_{\mathrm{c}}}{2}\sqrt{k_{\mathrm{p}}/(k_{\mathrm{p}}+k_{\mathrm{c}})}$ (equation 3.5). This distribution of the excitation amongst the velocity classes is crucial to the phenomenon of collective quantum beats, which is discussed in chapter 6.

3.3 Experiment

In this section we experimentally investigate EIT in the HPB regime. We will consider the transmission of a weak probe laser through a thermal rubidium vapour which is coupled to a strong continuous laser field on an optical transition between two excited states.

3.3.1 Experimental details

A schematic diagram of the experimental apparatus is shown in figure 3.4. We use a 2 mm long vapour cell, containing isotopically enriched ^{87}Rb with 98.25% ^{87}Rb and 1.75% ^{85}Rb, which is heated to 70 °C to provide a suitable resonant optical density for the probe. Due to nature of the manufacturing process, a small quantity of background gases are trapped within the vapour cell. Collisions between rubidium and these background gases give rise to a

measured Lorentzian line broadening of ∼7 MHz on the D_2 transition [79]. We measure the transmission of a weak [55] (20 nW) probe laser at 780 nm as its frequency is scanned ∼25 GHz around the rubidium D_2 ($5S_{1/2} \rightarrow 5P_{3/2}$) transition. A second laser at 776 nm provides a strong (27 mW) coupling field resonant with the $5P_{3/2} \rightarrow 5D_{5/2}$ transition which counter-propagates with the probe. The vapour cell is placed between two cylindrical NdFeB permanent magnets (the figure shows a cross-sectional view of the top-hat-profile of the magnets) with an axial magnetic field of strength 0.6 T which Zeeman-splits the $5S_{1/2}$, $5P_{3/2}$ and $5D_{5/2}$ manifolds into the HPB regime (see section 2.3). The magnets are designed to provide a magnetic field that is uniform to the 1 mT level over the extent of the vapour cell in the beam propagation direction (see appendix A for additional details of the field profile). Figure 3.5(b) shows the evolution of the state energies with increasing magnetic field strength.

In the HPB regime the relevant states are well identified by their spin-orbit angular momentum projection values m_J[1] and their nuclear angular momentum projection values m_I which we write in the basis $|m_J, m_I\rangle$. The coupling field has a power of 27 mW and is tuned on-resonance with the $5P_{3/2}|\frac{1}{2}, -\frac{1}{2}\rangle \rightarrow 5D_{5/2}|\frac{3}{2}, -\frac{1}{2}\rangle$ transition. The pump and coupling polarizations are set using $\lambda/4$ waveplates such that they drive σ^+ ($\Delta m_J = +1$) transitions. The beams are focused through the vapour cell to $1/e^2$ radii of 54 ± 1 μm for the probe and 116 ± 1 μm for the coupling. The beam sizes are chosen as a compromise between maximizing the coupling intensity, minimizing beam diffraction across the cell and ensuring that the probed atoms observe a uniform coupling-beam electric field profile. The temperature and magnetic field strength are verified by quantitatively fitting the probe transmission spectra with the coupling beam blocked [29].

[1]Projection onto the quantization axis defined by the magnetic field vector.

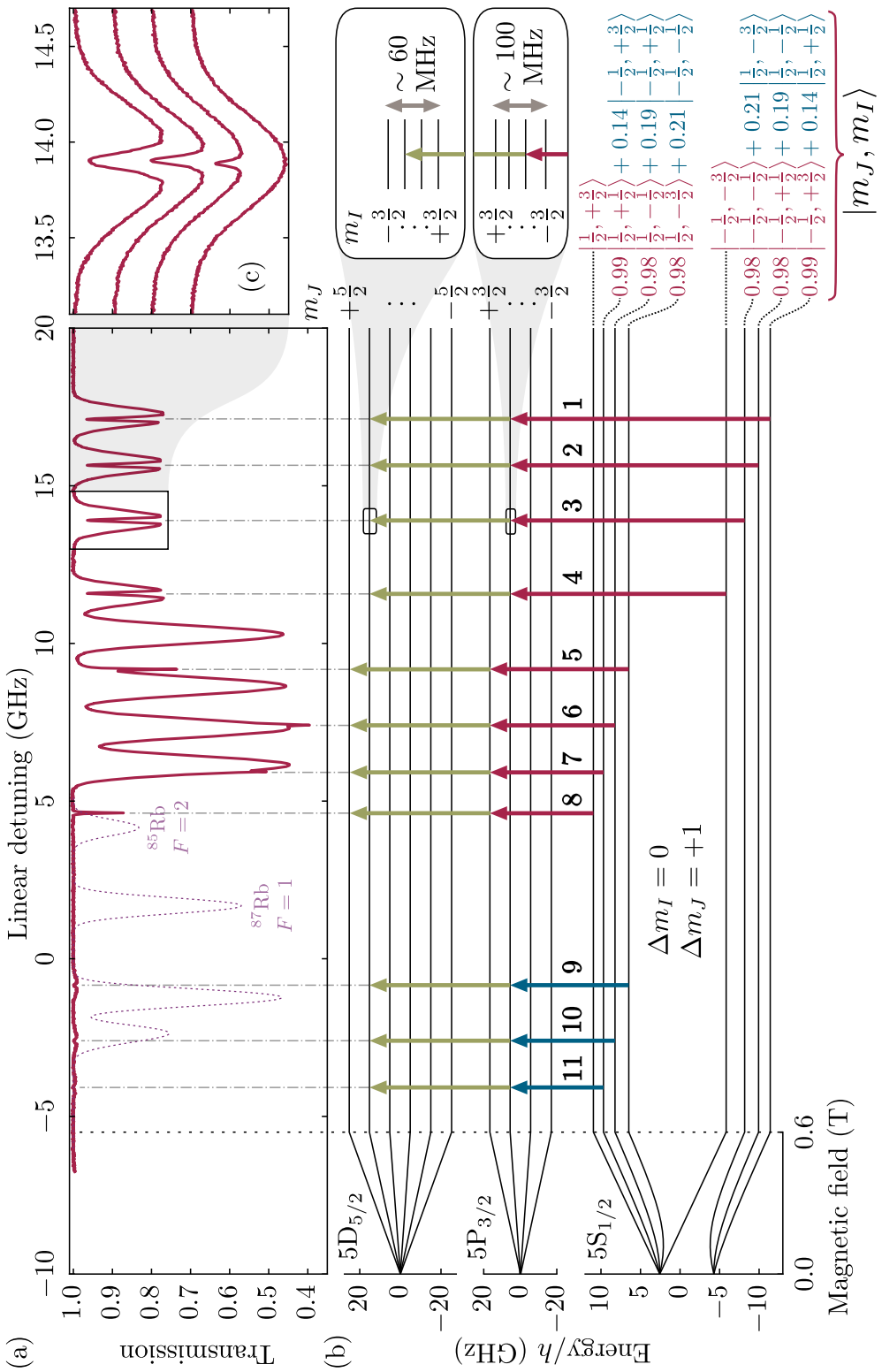
(a)
Transmission
Linear detuning (GHz)
^{85}Rb $F = 2$
^{87}Rb $F = 1$
(c)
(b)
Energy/h (GHz)
$5D_{5/2}$
$5P_{3/2}$
$5S_{1/2}$
m_J
m_I
~ 60 MHz
~ 100 MHz
$\Delta m_I = 0$
$\Delta m_J = +1$
Magnetic field (T)
$|m_J, m_I\rangle$

Figure 3.5: Panel (a) shows an experimentally measured weak probe transmission spectrum for a ^{87}Rb vapour cell placed in a magnetic field of $B = 0.6$ T (red) with a strong counter-propagating coupling field. The dotted purple line is the probe-only spectrum for a vapour cell with natural isotopic abundance, for a frequency reference. Panel (b) is a diagram of the transitions associated with each of the spectral features in panel (a). On the left of the panel is an energy level diagram for the relevant states, showing the evolution into the HPB regime at large magnetic fields. The eigenstates of the system in the $|m_J, m_I\rangle$ basis are shown to the right of the diagram for a field strength of $B = 0.6$ T. Even at this large field there still exists a significant admixture of states with opposite spin (blue text) in the $5S_{1/2}$ ground-state manifold; these result in the weak transitions indicated by the blue arrows. The large splittings between ground states as well as the electric dipole selection rule $\Delta m_I = 0$ ensure that only three atomic states are involved in each of the two-photon resonances. An expanded view of the three-level EIT resonance $5S_{1/2}|-\frac{1}{2},-\frac{1}{2}\rangle \rightarrow 5P_{3/2}|\frac{1}{2},-\frac{1}{2}\rangle \rightarrow 5D_{5/2}|\frac{3}{2},-\frac{1}{2}\rangle$ is shown in panel (c) for coupling-beam powers of 0, 3, 9 and 27 mW. Vertical offsets have been added for clarity. Zero detuning is given as the weighted D_2 line center of naturally abundant rubidium in zero-magnetic field [80].

3.3.2 Results

The experimentally measured probe transmission spectrum after addition of the coupling field is shown in figure 3.5(a). We observe several narrow spectroscopic features associated with the addition of the coupling field, which can be mapped onto individual Δm_J transitions as we show in figure 3.5(b).

The lines labelled 1-4 correspond to the four nuclear spin states ($m_I = -3/2, -1/2, 1/2, 3/2$) of the $m_J = -1/2 \rightarrow 1/2 \rightarrow 3/2$ two-photon resonance. For a single coupling field frequency these lines simultaneously display Doppler-free EIT, with the observed transparency windows each detuned differently from their respective probe-only absorption lines. The relative detunings of the transparencies are given by the relative energies of the m_I states in the $5P_{3/2}$ $m_J = 1/2$ and $5D_{5/2}$ $m_J = 3/2$ excited manifolds. Since the hyperfine structure intervals (m_I splittings) in these manifolds are significantly smaller than the Doppler width, the two-photon resonances are simultaneously observed within the four Doppler-broadened absorption lines. Part (c) of figure 3.5 shows an expanded view of line 3 for coupling-beam powers of 0, 3, 9 and 27 mW. At 27 mW we observe a high contrast transparency. There is evidently a slight variation in the central frequency of the transparency between each data set which can be explained by a drift in the coupling laser frequency as it is not actively stabilised.

The weak absorption lines labelled 9-11 correspond to probe transitions from the residual $m_J = -1/2$ components of the predominantly $m_J = 1/2$ ground-state manifold. Here, the $5P_{3/2}$ excited states are the same as for lines 1-3 and therefore we observe the formation of similar EIT resonances.

Additionally we observe four Doppler-free two-photon absorption lines labelled 5-8, approximately 1.5 GHz red detuned from their respective probe-only absorption lines. The leftmost of these lies in a transmissive region of the spectrum and can be tuned in frequency with the coupling beam detuning, in width with the coupling beam power and in depth by the atomic number density through changing the cell temperature. This line can be tuned around

the frequencies of the commonly used ^{87}Rb $F = 1$ and ^{85}Rb $F = 2$ transitions in the zero magnetic field spectrum and therefore could find application as a narrowband notch filter or optical switch.

Since all of the D_2 resonances are fully resolved in the HPB regime, the probe field couples to an individual $|m_J, m_I\rangle$ ground state and the transition selection rule $\Delta m_I = 0$ determines that the coupling field only interacts with the probe via a single intermediate state. Thus, all the observed two-photon resonances involve only three atomic states. Given this, we can apply the theoretical formalism introduced in section 3.2 in order to quantitatively model the line shapes.

Focusing on the $|-\frac{1}{2}, -\frac{1}{2}\rangle \rightarrow |\frac{1}{2}, -\frac{1}{2}\rangle \rightarrow |\frac{3}{2}, -\frac{1}{2}\rangle$ EIT resonance (labelled 3 in figure 3.5) we show the experimental transmission spectra as well as a least-squares fit to three level model, in figure 3.6. In the model the $5P_{3/2}$ decay rate is fixed as the 6 MHz natural linewidth plus the 7 MHz broadening ($\Gamma_p/2\pi = 13$ MHz) due to collisions with background gases. The free parameters of the fit are: the probe transition line centre frequency $\Delta_p^{(0)}$, the coupling field detuning Δ_c, the coupling-field Rabi frequency Ω_c, the $5D_{5/2}$ decay rate Γ_c and the atomic number density N. The values resulting from the fit are: $\Delta_p^{(0)}/2\pi = 13.9002 \pm 0.0001$ GHz, $\Delta_c/2\pi = -5.5 \pm 0.2$ MHz, $\Omega_c/2\pi = 255.1 \pm 0.1$ MHz $\Gamma_c/2\pi = 30.0 \pm 0.1$ MHz. The model is clearly in excellent agreement with the data as indicated by the smallness of the residuals. We calculate a reduced chi-squared statistic $\chi^2_\nu = 2$ [81], which is larger than expected for the number of data points, due to the noticeable structure in the residuals (near to line centre) which is symmetric about resonance. We find that the observed structure is consistent with a small amount of electromagnetically induced absorption [82] (EIA) caused by the back-reflected coupling light in the cell (this EIA is the subject of investigation in chapter 4).

Figure 3.7 shows experimental spectra and fits for three different coupling detunings, $\Delta_c/2\pi \approx 0, 400, 800$ MHz. The transition from resonant EIT to off-resonant two-photon absorption is clearly displayed across this range

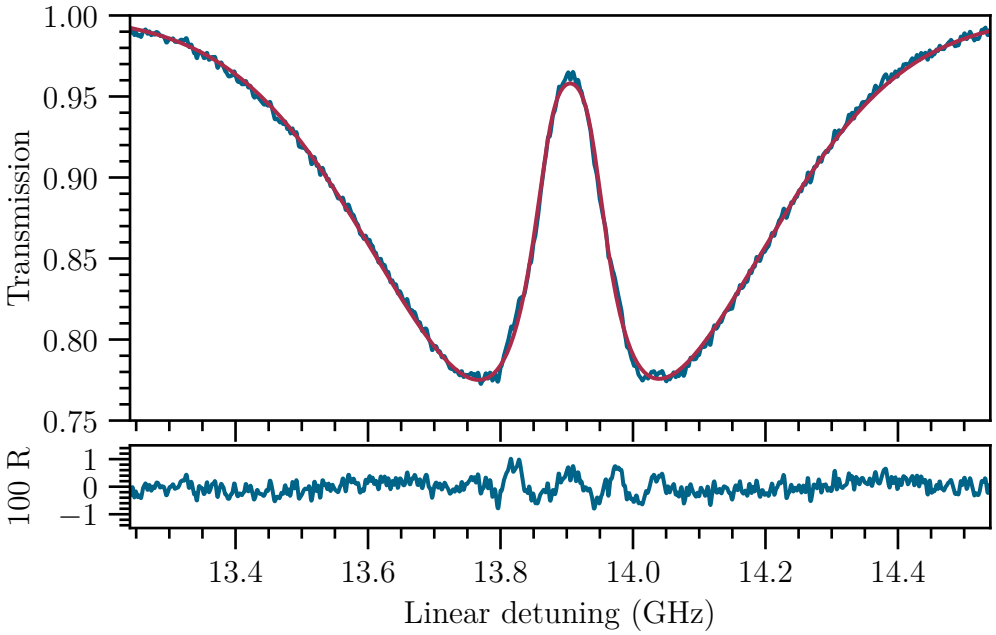

Figure 3.6: Experimental transmission spectrum (blue) showing a purely three-level EIT resonance in a hot ^{87}Rb vapour. The red line is a least-squares fit to the data using a three-level EIT model. The fit results in a measurement of the coupling-beam Rabi frequency $\Omega_c/2\pi = 255.1 \pm 0.1$ MHz where the uncertainty is from the statistical error of the fit. The residual (R = Experiment − Fit) shows the excellent agreement between the model and data, with the small amount of structure near line center being explained by the EIA effect (see main text).

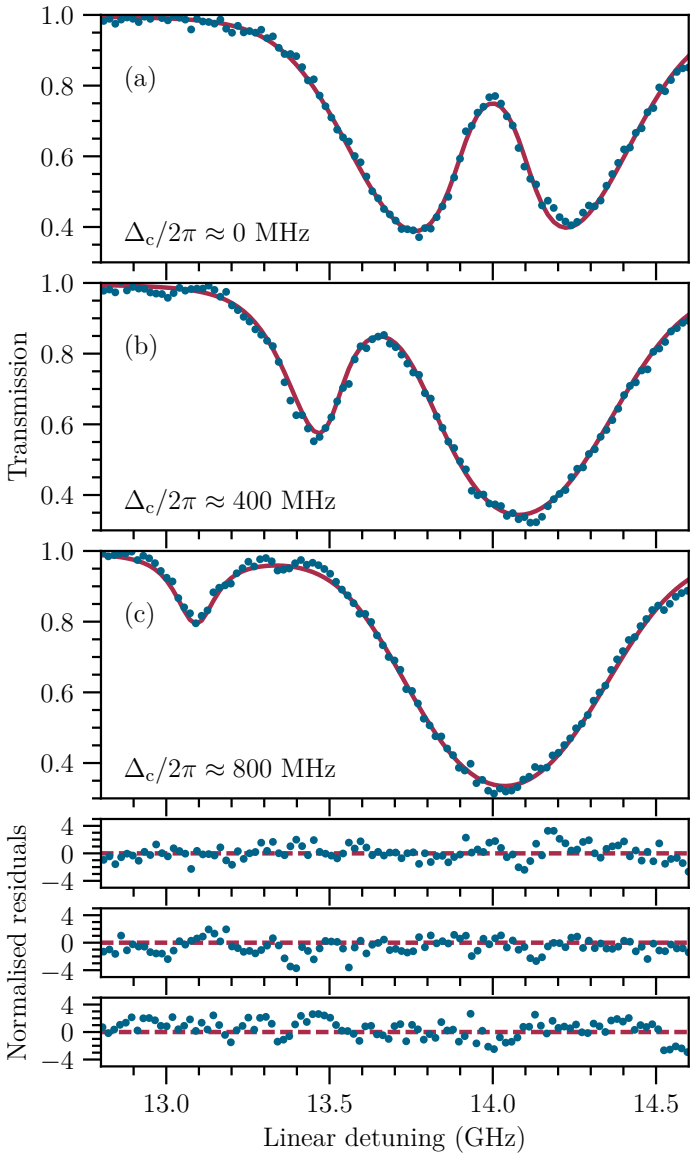

Figure 3.7: Experimental transmission spectra (blue) and numerical fits (red) for three coupling-beam detunings. The fit parameters except for coupling detuning are constrained to be equal in all three data sets. The extracted coupling-beam detunings are $\Delta_c/2\pi = -18.8 \pm 0.6,\ 408.0 \pm 0.6,\ 834.7 \pm 0.7$ MHz. The residuals (R) show the excellent agreement between the model and data.

providing an excellent test for the model. In this case all fit parameters, except for coupling detuning, are constrained to be equal for all data sets. Again we find that the resulting fits are in excellent agreement with the experimental data.

In summary, the application of a large magnetic field, in the HPB regime, allows the selective coupling of individual two-photon resonances. This results in EIT line-shapes that have good contrast and can be easily and accurately modelled with a simple analytic formula. In contrast, such good agreement is not easily obtained for the case of zero magnetic field. In the latter case, multiple overlapping resonances lead to reduced EIT contrast and more complex line shape, the modelling of which is computationally demanding [70].

3.4 Dipole matrix element measurement

Matrix elements for the alkali-metal atom D-lines are known to a very high precision by measuring fluorescence decay lifetimes [56]. Extending this technique to transitions between excited states is generally very difficult owing to the many possible decay channels. In most cases these matrix elements can be inferred by combining experimentally measured lifetimes with theoretically predicted branching ratios. However, in the case of excited states with large orbital angular momenta, e.g. D states, properties such as lifetimes and branching ratios are more difficult to calculate accurately [83, 84]. Direct experimental measurements of these matrix elements are therefore needed to support theoretical models.

Based on the excellent agreement between experiment and theory in the previous section, we now extract the coupling Rabi frequency from the numerical fitting, for a range of coupling-beam powers and detunings, allowing us to make the first direct measurement of the dipole matrix element $|\langle 5P_{3/2}||er||5D_{5/2}\rangle|$.

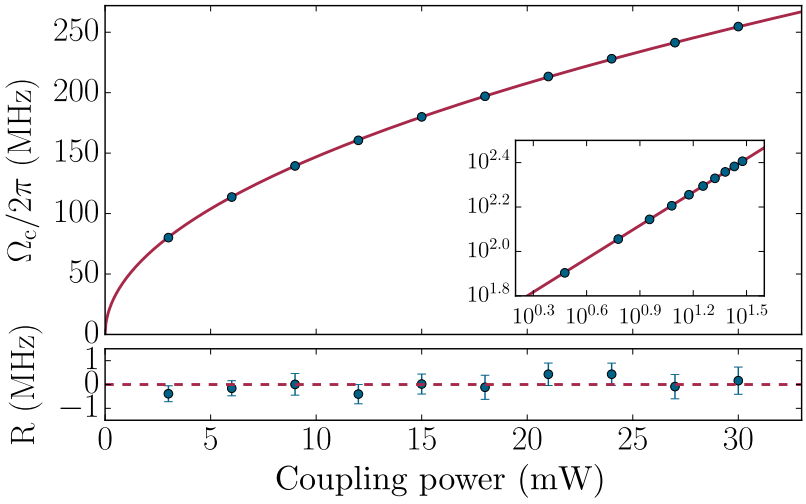

Figure 3.8: Extracted values of the coupling Rabi frequency (Ω_c) for increasing coupling-beam power (P). The red line is a least-squares fit to the function $\Omega_c = \alpha\sqrt{P}$, with $\alpha/2\pi = (46.57 \pm 0.03)$ MHz/$\sqrt{\text{mW}}$. The residuals (R) are shown below and the fit has a reduced chi-squared of 0.9. The inset shows the same data on a logarithmic scale.

At each power Rabi frequencies are extracted for 15 coupling-beam detunings (between −80 and +80 MHz) and these are averaged to give the data points shown in Fig. 3.8; the error bars shown are the standard error on the mean. Since the Rabi frequency is proportional to the local electric field amplitude, we expect to observe a square root dependence on the coupling-beam power. In Fig. 3.8 the red line is the result of a least-squares fit to the experimental data using the function $\Omega_c = \alpha\sqrt{P}$, from which it is determined that $\alpha/2\pi = (46.57 \pm 0.04)$ MHz/$\sqrt{\text{mW}}$. The agreement between model and experimental data is excellent, considering there is only a single free-parameter, with structureless residuals and reduced chi squared $\chi^2_\nu = 0.9$ [81]. In the following section we provide details of how the measured value α can be converted into the dipole matrix element.

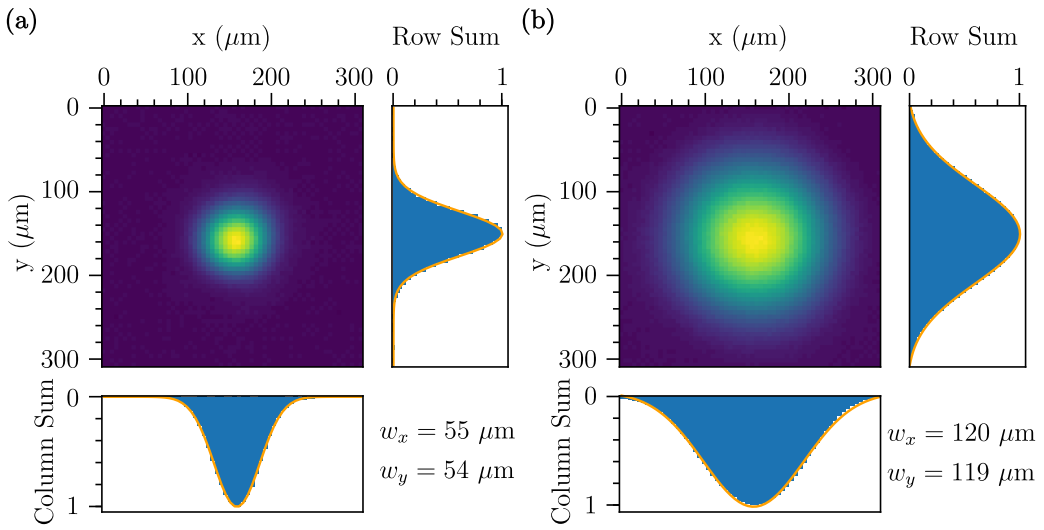

Figure 3.9: Experimentally measured beam profiles of the probe (a) and coupling (b) lasers at the position of the centre of the atomic vapour cell. The normalised sums of pixel row and column values are shown (blue) along with the fit to a Gaussian function (orange). The fitted $(1/e^2)$ waists are displayed.

3.4.1 From Rabi frequency to dipole-moment

To calculate the dipole moment we first need to determine the absolute value of the coupling-beam electric field in the atoms' vicinity. Therefore, the vapour cell and magnet are removed from the experimental set-up and a Thorlabs DC1545M CMOS camera is used to record the beam intensity profiles in relative units, B_{pixel}. The absolute calibration of the electric field at each pixel, E_{pixel}, is provided by the pixel size ($d = 5.20$ μm square) and the measured total beam power (P) through the equation

$$E_{\text{pixel}} = \frac{1}{d}\sqrt{\frac{B_{\text{pixel}}}{\sum B_{\text{pixel}}}}\sqrt{\frac{2P}{cn\epsilon_0}}. \tag{3.6}$$

The normalised intensity profiles are displayed in figure 3.9.

Since the coupling-beam intensity changes significantly over the probe beam extent, we use a weighted average of the coupling-beam electric field profile (E_{coupling}) that is weighted by the probe-beam intensity profile (I_{probe}),

i.e.

$$E_0 = \frac{\int\int I_{\text{probe}}(x,y) E_{\text{coupling}}(x,y)\ \mathrm{d}x\mathrm{d}y}{\int\int I_{\text{probe}}(x,y)\ \mathrm{d}x\mathrm{d}y}.$$

Note that the total detector size is 5 mm × 5 mm which means that for a Gaussian beam of waist 100 μm the fraction of power that falls outside the detector is negligible. We then determine the dipole moment of the driven transition (between ground and excited states $|g\rangle$ and $|e\rangle$) through the equation:

$$\begin{aligned}|\langle g|er_{+1}|e\rangle| &= \hbar\frac{\Omega_{\text{c}}/\sqrt{P}}{E_0/\sqrt{P}} \\ &= (0.72 \pm 0.0006_{\text{stat}} \pm 0.01_{\text{syst}})\ ea_0\end{aligned}$$

where the subscript +1 refers to the transition being of σ^+-type in which the final magnetic spin-orbit angular momentum $m'_J = m_J + 1$.

To go from the measured dipole moment of the driven transition to the reduced matrix element for the $5\text{P}_{3/2} \rightarrow 5\text{D}_{5/2}$ transition, which is a quantity of more general interest, we use the Wigner 3-j symbol [85]

$$|\langle J, m_J|er_{-1}|J', m_{J'}\rangle| = \begin{pmatrix} J & 1 & J' \\ -m_J & -1 & m_{J'}\end{pmatrix} |\langle J||er||J'\rangle|$$

which gives

$$\begin{aligned}|\langle 5P_{3/2}||er||5D_{5/2}\rangle| &= \sqrt{10}|\langle 5P_{3/2},\ m_J = 1/2|er_{-1}|5D_{5/2},\ m_J = 3/2\rangle| \\ &= (2.27 \pm 0.002_{\text{stat}} \pm 0.04_{\text{syst}})\ ea_0.\end{aligned}$$

Our measured value is within 2σ of the theoretically calculated value of 2.334 ea_0 [84]. Over the course of the following section we discuss the possible sources of uncertainty in the measurement and give suggestions for future improvements.

Source	Correction (%)	Uncertainty (%)
Statistical		0.08
Optical power meter		1.5
Beam spatial profiles		0.7
Coupling polarization purity	0.5	0.05
Vapor cell transmittance	2.9	0.3
Line shape systematics		0.5
Total		2

Table 3.1: Error budget of the $|\langle 5P_{3/2}||er||5D_{5/2}\rangle|$ dipole moment measurement. The second column shows the corrections we have made to account for the measured polarization impurity of the coupling field and for the measured reflectivity of the vapour cell windows.

3.4.2 Uncertainties

Table 3.1 shows a breakdown of uncertainties in the measurement. One of the major sources of systematic uncertainty is the optical power meter (Thorlabs S121C sensor). Optical power meters that are sensitive over this range in beam-powers typically have calibration uncertainties of 3% or more. Having measured the powers of identical beams with several devices, we determine that our device is within its 3% calibration uncertainty. Since this is the largest single source of uncertainty in the measurement, we envisage that this method could be used to improve the calibration of power meters given a precisely known dipole moment.

Another large source of uncertainty comes from the beam profile measurements. The uncertainty in the axial positioning of the camera with respect to the centre of the vapour cell is 1 mm. Additionally the thickness of the vapour cell is 2 mm. Over this range the beam profile changes marginally but significantly. The corresponding uncertainty in the matrix element measurement can be estimated by calculating its value using beam profiles recorded at axial positions of ± 1 mm for the probe beam and ± 2 mm for the coupling beam[2]. We estimate the errors associated with the probe and coupling beams to be 0.4% and 0.5% respectively. By adding these in quadrature we find the total

[2]Beam profiles for ± 1 mm for the coupling beam were not recorded.

error associated with beam profile measurement is 0.7%. In future by using broader beams and/or thinner vapour cells it would be possible to reduce this uncertainty significantly.

Knowing the polarization purity of the coupling beam is crucially important to the measurement. This is because the power meter is only sensitive to the total beam-power and not the power in the relevant polarisation mode. The transition used to measure the matrix element is a σ^- transition and therefore only the fraction of the coupling beam that has the correct circular polarization will contribute to the EIT. To complicate matters the polarisation purity cannot simply be measured using standard polarimetry techniques [86] as the vapour cell has birefringent properties meaning that the polarisation inside and outside the vapour cell are different. Therefore we have developed a method with which to measure the polarisation purity within the cell to a high level of precision. First, we find a different resonance for the coupling laser, which is driven by light of the opposite handedness, in this case a σ^- transition. We then observe any EIT that appears due to the impure polarization component in the coupling field, fitting the lineshape to extract the coupling Rabi frequency. To make the measurement simpler we choose two transitions with the same dipole moments so that by comparing the extracted Rabi frequencies we have a direct measure of the polarization purity. Using this method we measure a purity of $(99.1 \pm 0.1)\%$. With this precise measurement we are able to apply a correction to the measured dipole moment, reducing the polarisation purity uncertainty to a negligible level.

Similarly we make a correction for the coupling beam power that is lost due to reflection at the vapour cell interfaces. The glass cell is not anti-reflection coated and so we expect approximately 4% reflection at each interface. As expected we measure a total propagation loss, through all four surfaces, of 16.4%. After applying this correction the associated uncertainty is again reduced to a negligible level.

Finally, to reduce the systematic uncertainty to less than 1% it becomes necessary to consider many sources of systematic changes to the line shape

Source	Uncertainty (%)
Coupling beam intensity distribution	0.4
EIA modification	<0.2
Frequency calibration	0.1
Absolute calibration of transmission	0.2
Effective probe saturation	0.08
B field non-uniformity	0.1
Total	0.5

Table 3.2: Breakdown of line shape systematic uncertainties.

such as the small amount of EIA [82] we observe in the transmission spectra. A breakdown of these systematic line shape effects is presented in the following section.

3.4.3 Systematic line shape effects

Table 3.2 shows a breakdown of potential sources of error in the dipole matrix element measurement caused by systematic changes to the EIT line shape. In all cases the uncertainties are estimated by numerically modelling the modified line shapes and then performing a least-squares fit to the three-level EIT model [77]. The following subsections provide details of these systematic changes to the EIT line shape.

Coupling beam intensity distribution

The three-level EIT line shape [77] implicitly assumes that every atom within the probe field experiences the same coupling-beam electric field. In practice this can be achieved by using specially engineered diffractive optics [87] to create super-Gaussian or top-hat shaped beams of light. However, this beam shape is not a stable propagating mode and rapidly changes shape away from the focal plane. For simplicity we take the alternate approach of expanding the coupling beam to approximately double the size of the probe beam. This approach leads to a lower peak Rabi frequency but has the advantage

that the beam profile does not change significantly on propagation through the medium. We calculate the theoretical probe transmission spectrum for probe and coupling fields that have Gaussian spatial profiles and then fit the theoretical line-shape which assumes constant intensities. By doing so, we estimate that making the assumption of constant coupling-beam intensity leads to a 0.4% overestimate of the matrix element.

EIA modification

The vapour cell windows are uncoated and have a measured reflectivity of approximately 4% at each surface. The reflected light from the coupling beam partially overlaps with the interaction region (the cell is tilted to minimise the overlap) and gives rise to weak EIA resonances. This effect is the subject of chapter 4 and the associated publication [82]. Its modifying effect on the EIT line shape is well understood and can be quantitatively modelled [82]. Figure 3.10 shows the expected EIA line shape assuming a 4% back reflection overlapping with 15% of the length of the interaction region. The three-level EIT model [Eq. (3.3)] is fitted to the modified line shape and the residual shows the same structure that is observed in the experimental data. Although the effect on the line shape is quite noticeable, the fit reveals that the effect on the extracted Rabi frequency is small, typically a $< 0.2\%$ change. Additionally, the sign of the change varies across the range of coupling-beam powers used and therefore the impact on the measurement of the matrix element is smaller still.

B field non-uniformity

If the vapour cell is not positioned correctly at the centre of the magnetic field profile there will be a significant magnetic field gradient across the cell leading to an effective broadening of the lines. The effect on the line shape can be quite large so care is taken to ensure the cell is positioned correctly. The uncertainty in the positioning of the cell is ± 0.5 mm. From the theoretical

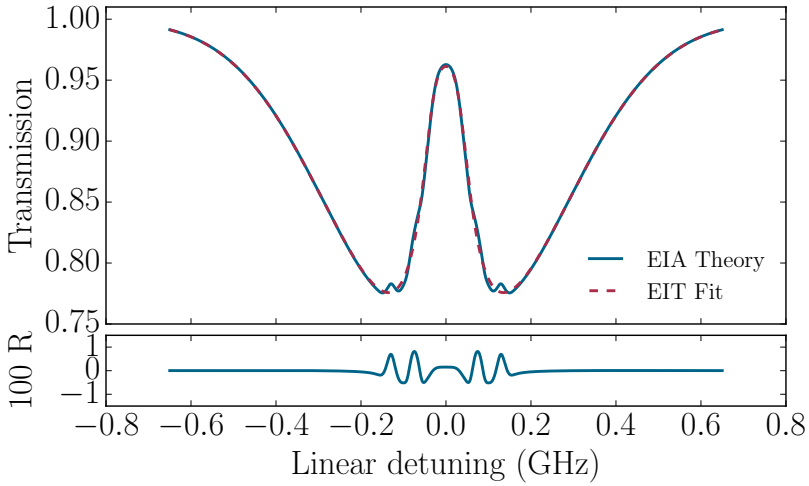

Figure 3.10: Predicted EIA line shape for a 4% back reflection of the coupling beam overlapping with 15% of the interaction region. The dashed line shows the fit to this line shape using a three-level EIT line shape and the residual (R) shows the same structure as is found in the experimental data.

magnetic field profile we estimate that this leads to a maximum RMS field variation of 0.05 mT which corresponds to a line broadening on the 1 MHz level. Simulating the modified line shape and fitting using equation 3.3 results in a 0.1% overestimate of the matrix element.

Effective probe saturation

In our experiment the probe-beam Rabi frequency is 0.5 MHz which is significantly smaller than the natural linewidth of 6 MHz. As such there is very little power broadening of the spectral lines and the weak probe assumption [55] (section B) is very good. Nevertheless we find that making this approximation leads to a 0.08% underestimate of the matrix element.

Frequency calibration

The experimental spectra are frequency calibrated using an optical cavity with a free spectral range of 375 MHz and an atomic reference based on hyperfine optical pumping spectroscopy [88] (details can be found in appendix D). The uncertainty in the frequency scaling is estimated to be 0.1%, which directly correlates with the uncertainty in the dipole matrix element.

Absolute calibration of transmission

The presence of other nearby absorptive resonances can modify the EIT line shape. Specifically, the absorption in the wings of the line is increased more than the line-centre value. Since the nearest absorptive resonances are ~ 1.5 GHz away, this effect is small and leads to a 0.2% underestimate of the matrix element.

3.5 Summary

In summary, we have experimentally investigated EIT in a thermal atomic vapour the HPB regime. We have demonstrated that the HPB regime vastly reduces the complexity of modelling nonlinear atom-light interactions in thermal vapours. We have made use of the excellent agreement between experiment and theory to directly measure an excited-state dipole matrix element, which has hitherto only been possible indirectly through lifetime measurements. In the following chapter we extend the experiment and theory to include an additional coupling field and we investigate the appearance of EIA.

Note that the analysis presented in this chapter has been slightly modified since the publication of article [47] due to a minor error in the calculation, which changes the quoted value of the matrix element by less than the error

bar. We are writing to the journal to make a formal alteration to the published work.

Chapter 4

Electromagnetically induced absorption (EIA)

This chapter is based on the following publication:

D. J. Whiting, E. Bimbard, J. Keaveney, M. A. Zentile, C. S. Adams, and I. G. Hughes, *Electromagnetically induced absorption in a nondegenerate three-level ladder system*, Optics Letters **40** 18, 4289 (2015), 10.1364/OL.40.004289.

4.1 Introduction

Three-level atoms driven by two applied fields display a variety of effects, including EIT [7], coherent population trapping [8] and coherent population transfer [89]. By adding further fields and states, a plethora of different phenomena have been observed. Two such effects are the appearance of electromagnetically induced gratings/Bragg reflection [90, 91, 92] and electromagnetically induced absorption (EIA) [93, 94]. In contrast to the sharp increase in resonant transmission that characterises EIT, these effects are identified by a decrease in resonant transmission due to the presence of additional coupling fields. A concomitant change in sign of dispersion can

be used to switch between subluminal and superluminal light propagation [95, 96, 97, 98, 99]. Previous work on EIA focussed on Zeeman-degenerate systems, where the interpretations of the phenomenon relied upon spontaneous transfer of coherence [100, 101, 102, 103] or population [104], with a minimum of four levels. More recently, EIA has been observed in a degenerate lambda system [105] and also in a four-level $\mathcal{N}$-system [106], even when the degeneracy is lifted by applying a small magnetic field. The effects of thermal motion on such systems have also been investigated [107].

In this chapter we present the first experimental observation of EIA in a non-degenerate three-level ladder system. In a thermal ^{87}Rb vapour, the degeneracy is lifted by a strong magnetic field, in which the atoms enter the HPB regime [72, 45, 108] where, due to selection rules, all of the relevant optical transitions are separated in frequency by more than the Doppler width. Hence, the transitions are individually addressable and a pure non-degenerate three-level system is formed. EIA is observed by measuring the transmission of a weak probe beam [55] through an atomic vapour which is dressed by both co- and counter-propagating coupling beams. Both coupling beams have the same optical frequency, since they are from the same laser source, and are resonant with an excited-state transition forming a ladder system similar to standard EIT configurations [77]. A model based on [109] reproduces the experimental results and highlights the prominent role of fast moving atoms in the observed spectral features.

Using the same ladder system, albeit in the absence of any applied magnetic field, narrow absorption resonances due to four-wave mixing have recently been observed [75]. In our experiment we observe no such four-wave mixing emission, nor any strong dependence of the EIA signals on the beam angles as would be expected if phase-matching were important. Instead, our results can be understood simply in the context of multi-photon resonances for moving atoms, which we will now discuss.

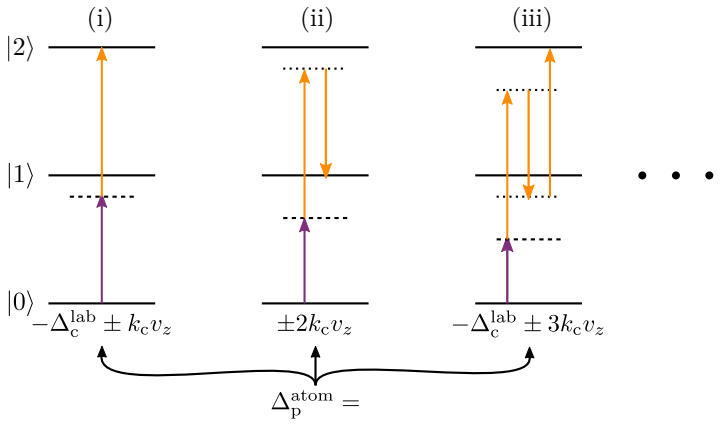

Figure 4.1: Conditions for multi-photon resonances (in the atomic reference frame). Atoms travelling with velocity component v_z along the probe field direction observe a Doppler shifted coupling field detuning $\Delta_c^{lab} \pm k_c v_z$ for the co- and counter-propagating coupling fields respectively. Odd numbers of coupling photons (orange) lead to resonances between states $|0\rangle$ and $|2\rangle$ (e.g. i, iii), and even numbers between states $|0\rangle$ and $|1\rangle$ (e.g. ii). These resonances occur when the probe photons (purple) are detuned by the amounts shown below each diagram.

4.2 Theoretical model

In the rest frame of an atom moving with velocity component v_z along the probe field direction, the two coupling fields of wavenumber k_c (with detuning Δ_c^{lab} in the laboratory frame) are detuned by $\Delta_{c,\pm}^{atom} = \Delta_c^{lab} \pm k_c v_z$ (co- and counter-propagating fields respectively) and thus appear to have a non-zero frequency difference $\delta\Delta_c^{atom} = 2k_c v_z$. It is therefore possible to form resonances involving increasing numbers of coupling photons, m, by choosing a suitable probe field detuning Δ_p^{lab}. These resonances are shown diagrammatically in figure 4.1 in the rest frame of the moving atom.

For odd numbers of coupling photons (i and iii) we can form resonances between states $|0\rangle$ and $|2\rangle$ if the probe detuning

$$\Delta_p^{lab} = -\Delta_c^{lab} + (k_p \pm m k_c) v_z. \tag{4.1}$$

For even numbers of coupling photons (ii) we can form resonances between states $|0\rangle$ and $|1\rangle$ for

$$\Delta_{\mathrm{p}}^{\mathrm{lab}} = (k_{\mathrm{p}} \pm m k_{\mathrm{c}}) v_z. \tag{4.2}$$

These multi-photon resonances and the interaction between them causes the overall medium response to differ dramatically from standard EIT.

In order to model the probe transmission spectra we adapt the results of [109] to the case of a three-level ladder system. As we have already done for EIT, the first step is to write the Hamiltonian for a three-level atom (equation 3.1). However, in this case the coupling Rabi frequency Ω_{c} has a spatially dependent amplitude since the two counter-propagating coupling beams coherently add. Experimentally we consider the situation where the probe and coupling fields all propagate axially along z and therefore we write the spatially varying Rabi frequencies $\Omega_{\mathrm{p}}(z) = \Omega_{\mathrm{p}} e^{\mathrm{i}k_{\mathrm{p}}z}$ and $\Omega_{\mathrm{c}}(z) = \Omega_{+} e^{\mathrm{i}k_{\mathrm{c}}z} + \Omega_{-} e^{-\mathrm{i}k_{\mathrm{c}}z}$, where $\Omega_{\pm}$ are the Rabi frequencies associated with the forward- and backward-propagating coupling beams respectively.

Now, it should be possible to numerically solve the Lindblad master equation (equation 2.2) for each position z in the medium and thereby determine the atomic coherences and the action of the medium on the probe field. However, since the spatial variation of the coupling Rabi frequency is periodic, a more insightful approach is to look for Fourier series expansions (in space) of the density matrix elements. Specifically we write

$$\rho_{ij} = \sum_m \rho_{ij}^{(m)} e^{\mathrm{i}mk_{\mathrm{c}}z} \qquad ij = \{00, 11, 22, 21\},$$

$$\rho_{ij} = e^{\mathrm{i}k_{\mathrm{p}}z} \sum_m \rho_{ij}^{(m)} e^{\mathrm{i}mk_{\mathrm{c}}z} \qquad ij = \{10, 20\}.$$

The Lindblad master equation then produces a series of coupled equations on the elements $\rho_{ij}^{(m)}$, with different values of m coupled by the joint action of the two control fields. Since we are only interested in terms oscillating at the probe frequency[1], the relevant action of the medium on the probe field is

[1]This is equivalent to the rotating wave approximation.

entirely contained within the term $\rho_{10}^{(0)}$ which is the element of the coherence on the probe transition that oscillates at or near the probe frequency.

To simplify the calculation we work in the weak probe regime (Appendix B), and perform a perturbative expansion with Ω_p as a small parameter. To zeroth-order $\rho_{10} = 0$ since the initial populations $\rho_{11} = \rho_{22} = 0$ in a ladder system. To first order (i.e. terms linear in Ω_p), the solution for $\rho_{12}^{(0)}$ for a given velocity class v_z can be written as a continued fraction involving two Lorentzian lineshapes ($j = 1, 2$)

$$L_{j0}(m) = \frac{1}{2}\frac{1}{\Delta_j^\mathrm{lab} - (k_\mathrm{p} + mk_\mathrm{c})v_z + \mathrm{i}\gamma_{j0}}, \tag{4.3}$$

which describe precisely the aforementioned multi-photon resonances, involving $|m|$ coupling photons. Here, $\Delta_1^\mathrm{lab} = \Delta_\mathrm{p}^\mathrm{lab}$, $\Delta_2^\mathrm{lab} = \Delta_\mathrm{p}^\mathrm{lab} + \Delta_\mathrm{c}^\mathrm{lab}$, γ_{10} and γ_{20} are the decay rates of the coherences between the corresponding states.

In terms of $L_{j0}(m)$, the coherence of interest can be written as

$$\frac{\rho_{10}^{(0)}}{\Omega_\mathrm{p}} = \frac{1}{L_{10}(0)^{-1} + [X_+(1) + X_-(1)]}, \tag{4.4}$$

where the $X_\pm$ functions are defined by the recurrence relation

$$X_\pm(n) = -\frac{\Omega_\pm^2}{L_{20}(\pm n)^{-1} - \dfrac{\Omega_\mp^2}{L_{10}(\pm n \pm 1)^{-1} + X(n+2)}}. \tag{4.5}$$

The absorption coefficient of the probe field α can then be calculated in the usual way (chapter 2). For the purposes of this discussion it is only important to note that α is proportional to $\rho_{10}^{(0)}/\Omega_\mathrm{p}$.

In order to get an idea of the structure of this result, we consider a few simple limiting cases and approximations. In each case we plot, in figure 4.2, the normalised probe absorption coefficient as functions of atom velocity and probe detuning. The parameters used to generate the plots are $k_\mathrm{p} = k_\mathrm{c}$,

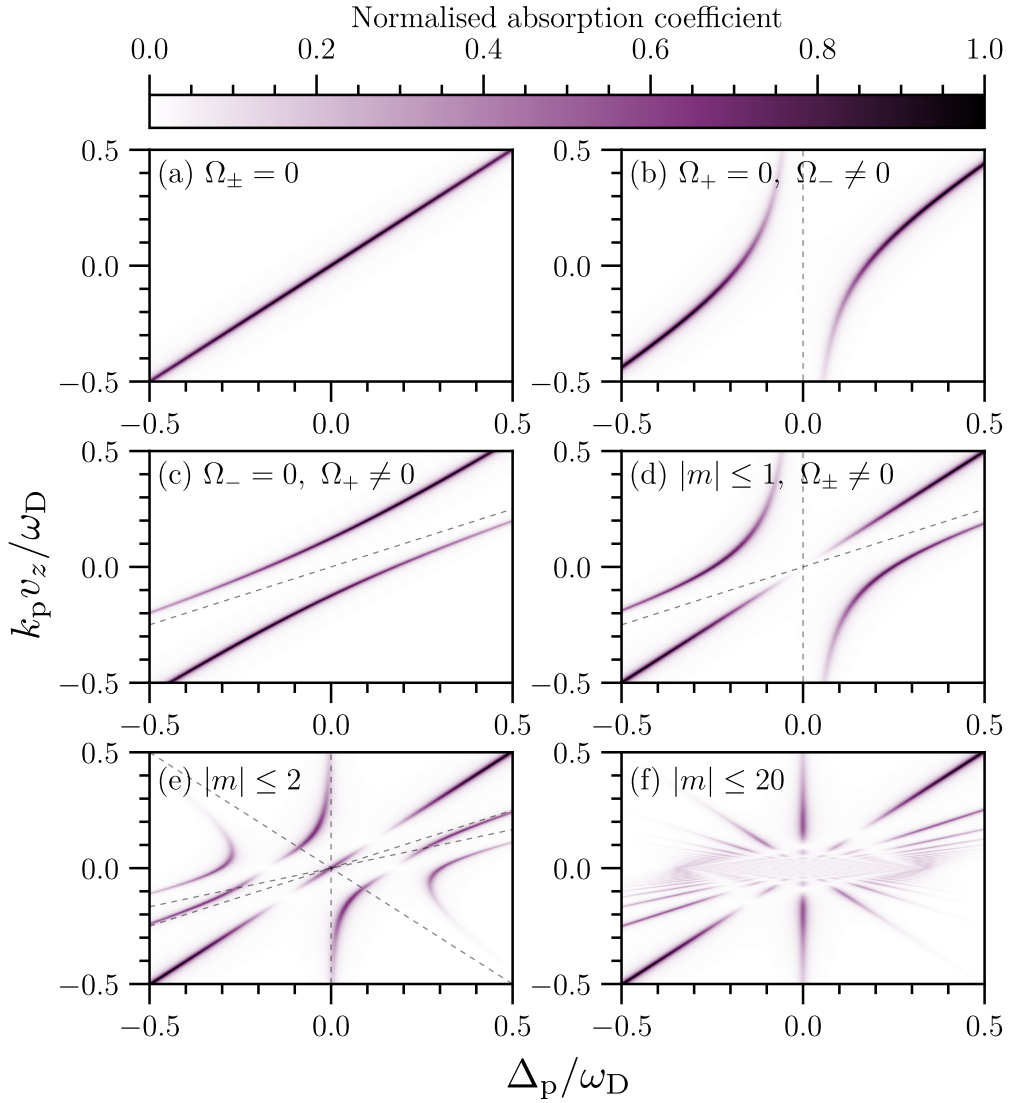

Figure 4.2: Velocity maps of the probe absorption coefficient are shown for several limiting cases and approximations of a model for EIA which is discussed in the main text. The dashed lines show the atom velocities and probe detunings that correspond to multi-photon resonances involving m coupling photons which give rise to the many avoided crossings. The atom velocities v_z and the probe detunings Δ_p have been scaled by the probe wavenumber k_p and the Doppler width ω_D.

$\gamma_{31} = \gamma_{21}$, $\omega_{\mathrm{D}} = 100\gamma_{21}$, $\Omega_{\pm} = 30\gamma_{21}$ and $\Delta_{\mathrm{c}} = 0$.

Firstly, considering the situation with both coupling beams switched-off (setting $\Omega_{\pm} = 0$), only the first term in the denominator of equation 4.4 remains and so we return to the probe-only response [figure 4.2(a)] as expected. Secondly, considering the situations where *either* the co- *or* counter-propagating beams are switched off (setting $\Omega_{+} = 0$ or $\Omega_{-} = 0$), we obtain the standard results (equation 3.3) for Doppler-free and Doppler-selective EIT respectively [figure 4.2(b,c)]. We previously discussed the roles of the different velocity-classes in section 3.2. Here, we only note the avoided crossings which occur for coincident one- and two-photon resonances. The dashed lines in figure 4.2(b,c) correspond to two-photon resonances involving the co- and counter-propagating coupling fields individually [figure 4.1(i)], which lead to the avoided-crossings.

When both beams are switched on ($\Omega_{\pm} \neq 0$), equation 4.5 becomes a continued fraction describing the effects of the multi-photon resonances shown in figure 4.1. To gain some further physical insight we can make approximations of $\rho_{10}^{(0)}$ by truncating the continued fraction at some level. Keeping only terms with $m = 0$ we return to the probe-only response. Keeping terms with $|m| \leq 1$ we receive a first-order approximation of the probe coherence which takes into account only the resonances involving 0 or 1 coupling photons, *and* the interference between them. In figure 4.2(d) we show the results of this first-order approximation. Here, it is clear to see the additional avoided crossings that are generated by the combined effect of the two coupling fields. Higher order terms ($|m| \geq 2$) in the continued fraction correspond to higher-order interaction of the medium with coupling photons, and involve multi-photon resonances occurring for particular values of v and $\Delta_{\mathrm{p}}^{\mathrm{lab}}$. In figure figure 4.2(e) we show the results for $|m| \leq 2$, i.e. additionally including resonances (ii) from figure 4.1. The additional resonance frequencies are plotted on the velocity-map as new dotted lines which have smaller gradients.

In the low-order approximations considered so far, the individual level crossings can be easily followed and understood. In figure 4.2(f) we show the

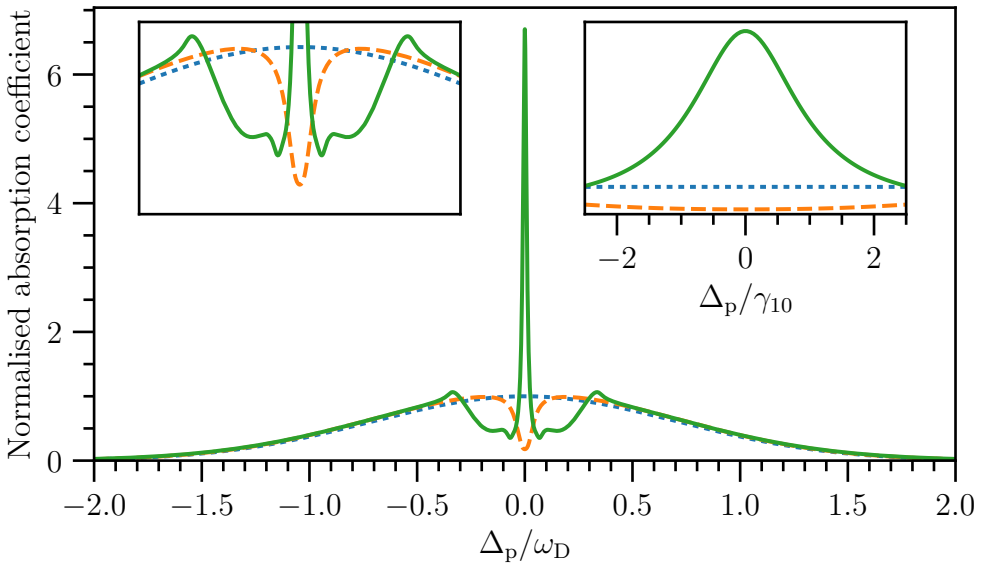

Figure 4.3: Theoretical probe absorption spectra. The absorption coefficients are normalised to the maximum of the Doppler-broadened probe-only spectrum (blue dotted line). Switching on a counter-propagating coupling field results in a Doppler-free EIT line shape (orange dashed line) which can be seen clearly in the expanded view (left inset plot). Additionally, switching on a co-propagating coupling field of equal strength results in a change from transparency to enhanced absorption (green solid line). The right inset plot shows an expanded view of the narrow absorption feature, with probe detuning now in units of the natural linewidth (γ_{10}).

results for $|m| \leq 20$. Further increases in m do not qualitatively change the appearance of the results. For a resonant coupling field ($\Delta_c^{\text{lab}} = 0$) the multi-photon resonances are degenerate at $v = 0$, $\Delta_p = 0$. This means that as resonances involving more coupling photons are included, the number of level crossings increases rapidly and it becomes difficult to identify absorption lines corresponding to particular transitions. The probe absorption spectra resulting from summation over the responses of all velocity classes is shown in figure 4.2. The dotted line shows the Doppler-broadened probe-only absorption line. The dashed line shows the Doppler-free EIT line shape

obtained by setting $\Omega_+ = 0$ [figure 4.2(b)]. For the chosen parameters the EIT shows good contrast with an 82% reduction in absorption on resonance (left inset). The solid line shows the *dramatically modified* response in the presence of both co- and counter-propagating coupling fields. Rather than a narrow transparency on resonance (EIT), there is now a narrow absorption feature (EIA) with a resonant absorption coefficient $\sim$ 6 times that of the probe-only spectrum. The spectral width of the enhanced absorption feature is approximately equal to the natural linewidth of the probe transition γ_{10}, as can be seen in the right-hand inset of figure 4.2, despite the fact that the coupling Rabi frequencies $\Omega_\pm = 30\gamma_{10}$.

By examining figure 4.2(f) it is clear that the resonant EIA is due to an integrated effect of many velocity classes having strong absorption at $\Delta_{\mathrm{p}}^{\mathrm{lab}} = 0$. A complementary physical explanation for this is as follows. For fast atoms such that $k_{\mathrm{c}} v_z > \Omega_\pm$, the two resonant coupling beams are Doppler shifted far off-resonance with $\Delta_{\mathrm{c},\pm} > \pm\Omega_\pm$. Taken independently, each of the coupling fields Stark shift the two-photon absorption line to $\Delta_{\mathrm{p}}^{\mathrm{lab}} \approx \pm\Omega_\pm^2/4k_{\mathrm{c}}v_z$ respectively [6]. Therefore to a first order approximation the addition of the second coupling beam simply cancels the light-shift of the first, creating a 2-photon resonance at precisely $\Delta_{\mathrm{p}}^{\mathrm{lab}} = 0$ for all velocity classes.

This being the case we should expect that the maximum absorption is obtained for equal co- and counter propagating coupling field strengths ($\Omega_+ = \Omega_-$). In figure 4.4(a) we plot the resonant absorption coefficient (relative to the probe-only absorption) against the ratio of the two coupling-beam Rabi frequencies. The two lines correspond to two different Rabi frequencies for the backwards coupling field; the blue solid line is for $\Omega_- = 0.25\omega_{\mathrm{D}}$ and the orange dashed line is for $\Omega_- = \omega_{\mathrm{D}}$. In both cases there is a smooth transition from EIT to EIA with increasing strength of the forward field. The absorption coefficient has a maximum for equal forward and backward field strengths, independently of the absolute field strengths. As the strength of the forward field is further increased, the absorption smoothly decreases again. At very high field strengths ($\Omega_+ > \omega_{\mathrm{D}}$) the medium becomes transparent again due to the strong Autler-Townes splitting by the forward coupling field

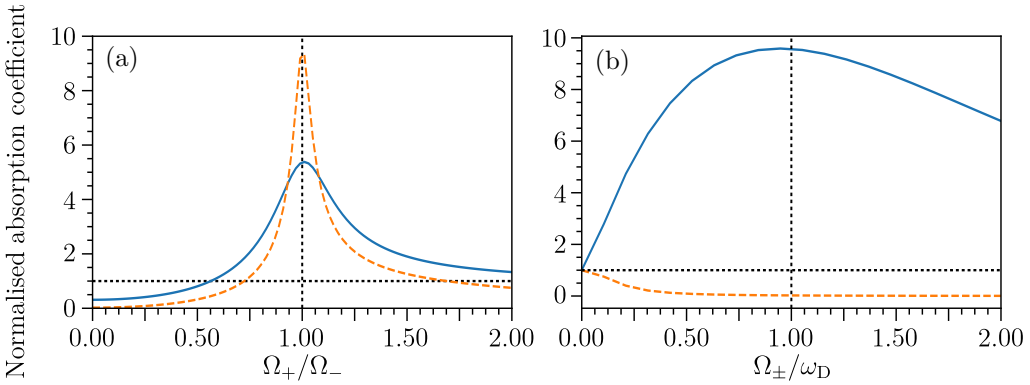

Figure 4.4: (a) Dependence of resonant absorption on the ratio of the forward and backward coupling field Rabi frequencies. The maximum absorption is obtained for equal field strengths. The two lines correspond to $\Omega_- = 0.25\omega_D$ (solid) and $\Omega_- = \omega_D$ (dashed). (b) Dependence of resonant absorption on the absolute coupling-field Rabi frequency when the forward and backward field strengths are equal (solid). When the forward beam is switched off (dashed) the absorption decreases with the applied field strength (EIT). The dotted lines in both (a) and (b) are guides for the eye.

being larger than the Doppler width. In figure 4.4(b) we plot the resonant absorption coefficient against the coupling Rabi frequency (in units of the Doppler width) under the condition $\Omega_+ = \Omega_-$. The solid blue line shows the absorption in the Doppler-free EIT configuration ($\Omega_+ = 0$) and the orange line shows the absorption in the EIA configuration ($\Omega_\pm \neq 0$). We observe that the absorption increases approximately linearly with $\Omega_\pm$ before saturating at around $\Omega_\pm = \omega_D$. We note that only fast-enough ($k_p v_z > \Omega_\pm$) atoms feel a perturbative light-shift that is linearly dependent on the atom velocity[2], and so only these atoms experience a cancellation of the light shift. Thus the saturation corresponds to the point at which the number of atoms moving fast enough to contribute to the resonant absorption begins to decrease rapidly.

Having discussed a theoretical model for EIA in an atomic three-level system,

[2]In contrast, slow atoms ($k_p v_z \ll \Omega_\pm$) experience a light shift (to first order) of $\pm\Omega_\pm$, which is independent of the atom velocity and therefore does not give rise to a light-shift cancellation.

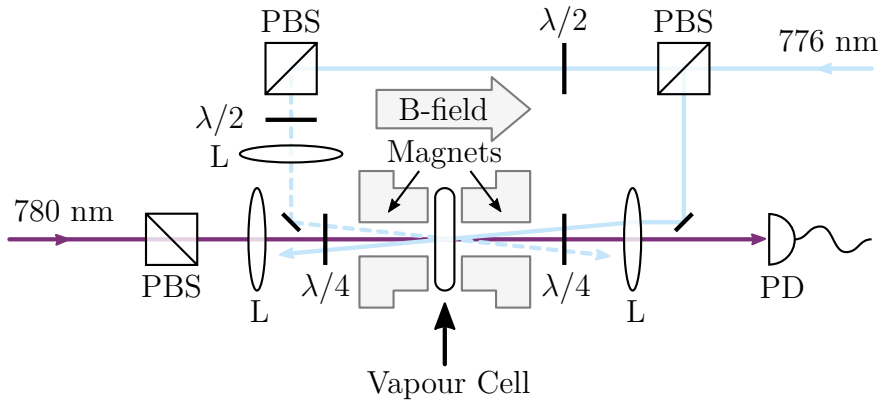

Figure 4.5: Schematic of the experimental setup. PBS - polarising beam splitter; $\lambda/2$ - half-wave plate; $\lambda/4$ - quarter-wave plate; L - lens; M - plane mirror; PD - photodiode; PM - permanent ring magnet. Switching from EIT to EIA is achieved by switching on the dashed 776nm coupling beam. Angles are exaggerated for clarity, the crossing angles between probe and coupling beams was less than 20 mrad.

we will now present the details and results of an experimental investigation, based on the same three-level ladder system in rubidium atoms that we investigated in chapter 3.

4.3 Experimental details

Experimentally, we study the probe field transmission spectra using the setup shown in figure 4.5. A weak probe beam (purple) is focussed through a 2 mm long vapour-cell containing 98.25% ^{87}Rb and 1.75% ^{85}Rb which is heated to 80 °C. As in the previous chapters the cell is positioned in a uniform axial magnetic field of strength $B = 0.6$ T, which is aligned with the probe beam. In the strong field the atoms enter the HPB regime, allowing an isolated three-level ladder system of states $5S_{1/2}(m_J = 1/2, m_I = 1/2) \rightarrow 5P_{3/2}(m_J = 3/2, m_I = 1/2) \rightarrow 5D_{5/2}(m_J = 5/2, m_I = 1/2)$ to be addressed by circularly polarised probe (780 nm) and coupling (776 nm) beams. The crossing angle between the probe beam and each of the co- and counter-propagating coupling beams was less than 20 mrad and the beam waists ($1/e^2$

radii) at the centre of the vapour cell were measured to be 50 μm (probe) and 120 μm (co-propagating coupling). The counter-propagating coupling beam was set up to have the same beam waist, although this was not independently measured.

4.4 Results

4.4.1 Dependence on coupling strength

We begin by measuring the probe transmission spectra in the case of a resonant coupling field ($\Delta_c^{\text{lab}} = 0$) with a fixed counter-propagating beam power of 47 mW. We study the dependence of the transmission spectra on the co-propagating coupling beam power, which is varied between 0 and 50 mW. Figure 4.6(a) shows the experimentally measured transmission spectra (solid orange lines) for a range of co-propagating coupling-beam powers (5 mW, 10 mW, 20 mW, 40 mW). The blue dashed lines are individual least-squares fits to the theoretical model (equation 4.4), with resulting model parameters $\Omega_+/2\pi = (19,\ 59,\ 102,\ 145) \pm 3$ MHz and averaged parameters: $\Omega_-/2\pi = 189 \pm 3$ MHz, $\Delta_p^{\text{offset}}/2\pi = -3.2 \pm 1.5$ MHz, $\Delta_c/2\pi = 4.6 \pm 1.5$ MHz and $\gamma_{20}/2\pi = 25 \pm 5$ MHz. On the whole, the model is in good agreement with the data, with the range of powers clearly showing the transition from EIT to EIA (the black dotted lines show the probe-only transmission). The observed contrast of the EIA is significantly lower than in the discussion of the theoretical model [figures 4.2 and 4.4(b)]. This is in part because we show the transmission as opposed to the absorption coefficient, but it is mainly because of the larger linewidth on the coupling transition relative to the Doppler width. The fit value of $\gamma_{20}/2\pi = 25 \pm 5$ MHz is much larger than the natural width $\gamma_{20}/2\pi = 0.33$ MHz [110] suggesting that there are additional broadening mechanisms at play. Fitting the probe-only spectrum with ElecSus [29], we have identified an additional broadening on the D_2 line of 7 MHz, which we attribute to collisions with background gases in the

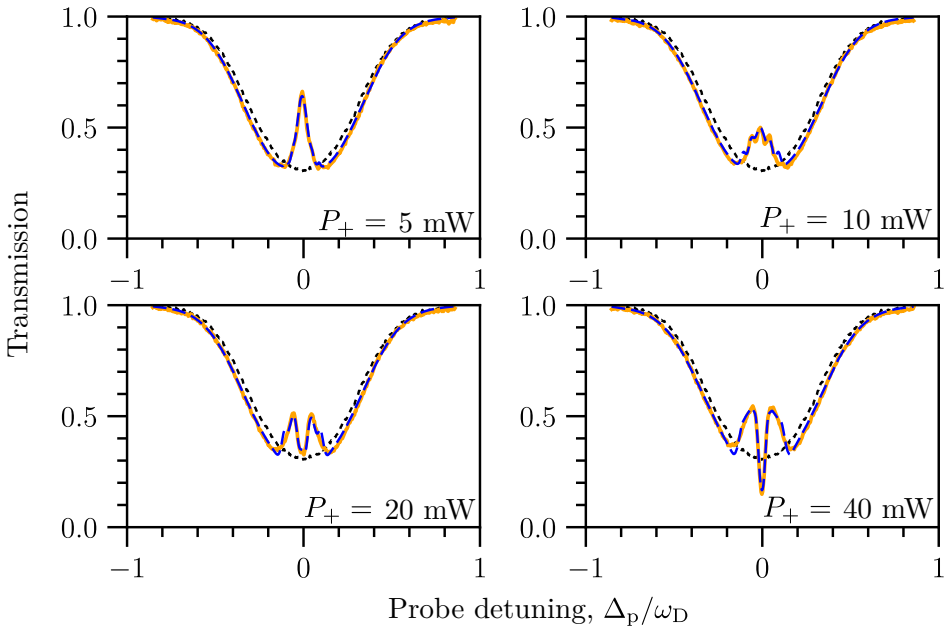

Figure 4.6: Experimentally measured probe transmission spectra (solid orange lines) displaying the transition from resonant EIT to EIA with increasing power in the co-propagating coupling field. The power in the counter-propagating field (P_-) is fixed at 47 mW and the power in the co-propagating field (P_+) is shown on each of the axes. The blue dashed lines show the results of a fit to the theoretical model described in the text and the black dotted lines show the probe-only transmission spectra.

cell. It is well known that collisional broadening of the 5P→5D transitions is significantly stronger than that of the D_2 line [79], suggesting that the strong broadening of γ_{20} is also due to collisions with background gases.

In the case of the experiment presented in this chapter alone, the coupling beam was not prepared in a single spatial mode before being incident on the atoms. In fact, in order to generate the large powers used in the experiment, the coupling laser was first put through a tapered amplifier system which led to a strongly non-Gaussian spatial mode. In this case the atoms in the probe beam may be subject to several different coupling field strengths (in the transverse direction), which leads to an effective broadening and a washing-out of finer spectral details. We suggest this as an explanation for the lower quality of agreement between experiment and theory than observed in the previous chapter. Additionally this may explain why the Rabi frequencies extracted from the fits are smaller than predicted for the measured beam size.

4.4.2 Dependence on coupling detuning

We now consider the effect of detuning the coupling field. The co- and counter-propagating beam powers are set to be equal and the detuning of the coupling field is decreased step-wise from zero in -20 MHz steps. The measured and theoretical probe transmission spectra are displayed in figure 4.7. Qualitatively, we observe a change from enhanced absorption at small Δ_c (dark region) to the formation of three narrow transparencies at large Δ_c (light regions). The position of the leftmost transparency tends to $\Delta_p = 0$ while the middle transparency tends to $\Delta_p = \Delta_c/3$ and the rightmost transparency tends to $\Delta_p = \Delta_c$.

We now consider a particular coupling field detuning ($\Delta_c^{lab}/2\pi = -457$ MHz), which clearly displays the three separate transparencies, and discuss the observed spectral features with reference to the theoretically calculated velocity map. The velocity map and associated transmission spectrum are

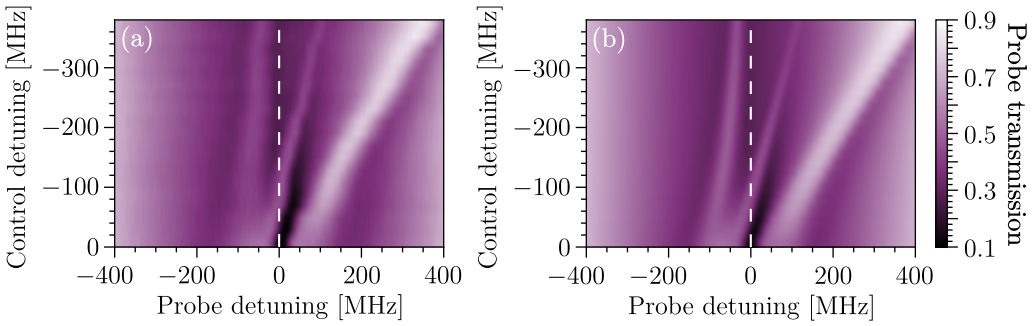

Figure 4.7: Dependence of EIA probe transmission spectra on the detuning of the coupling field. Both the experimental (a) and theoretical (b) spectra display a transition from enhanced absorption at zero detuning, to three narrow transparencies at large detuning. The transparencies have different detuning dependencies which are explainable in terms of avoided crossings which are associated with resonances involving multiple coupling photons. The white dashed lines are a guide to the eye.

shown in figure 4.8. Compared with the probe-only transmission spectrum [dotted black line in (b)], there are three distinct transparencies in the transmission spectrum [solid line in (b)], at detunings indicated by the vertical grey lines. The transparencies appear due to interference between the one-photon (probe-only) and many-photon resonances. The various atom velocities and probe frequencies corresponding to these multi-photon resonances (equations 4.1 and 4.2) are plotted on top of the velocity map as orange lines. Making use of this, we now discuss the origin of the observed spectral features.

Previously we discussed the case of a resonant control field, where the cancellation of light-shifts due to each of the two coupling beams led to a large number of atoms absorbing strongly in a narrow range of probe frequencies around resonance. However, in the case of an off-resonant coupling field the two light-shifts no longer cancel. Instead, where the probe-only absorption resonance coincides with a multi-photon resonance involving the coupling field, an avoided crossing leads to a small window of transparency for the probe field.

In the following we describe the origins of the spectral features labelled (i-iii)

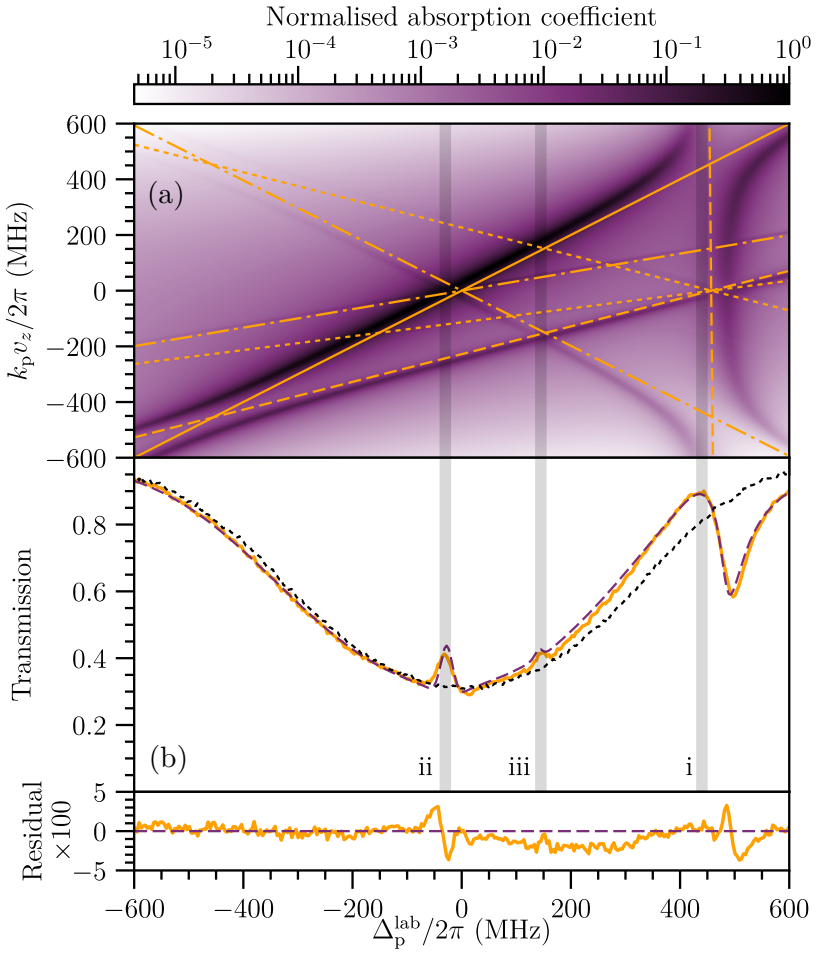

Figure 4.8: Probe transmission spectra obtained for an off-resonant standing-wave coupling field. Panel (a) shows the absorption coefficient of different atomic velocity classes in the vapour. Resonances involving 1, 2 and 3 coupling photons are shown for positive detunings by the dashed, dot-dashed and dotted lines respectively. The crossing of these resonances with each other and the main two-level absorption line (solid line) produces the multiple transparencies at the detunings indicated by the vertical grey lines. Panel (b) shows the experimentally measured probe transmission spectrum (solid line) along with a theoretical model (dashed line) which is obtained by integrating panel (a) over all velocities. The residuals (experiment-model) are plotted below. The parameters chosen for the colour-map in (a) are the result of a numerical fit, with resulting parameters: $\Omega_-/2\pi = 169$ MHz, $\Omega_+/2\pi = 163$ MHz, $\gamma_{10}/2\pi = 12$ MHz, $\gamma_{20}/2\pi = 16$ MHz and $\Delta_c^{lab}/2\pi = -457$ MHz. The dotted (black) line shows the transmission spectrum with both coupling beams switched off.

in figure 4.8. Firstly, (i) is the usual feature associated with off-resonant Doppler-free EIT. This corresponds to the crossing of the probe resonance (solid line described by $\Delta_{\mathrm{p}}^{\mathrm{lab}} = k_{\mathrm{p}} v_z$) with the two-photon resonance involving the counter-propagating coupling beam (dashed line described by $\Delta_{\mathrm{p}}^{\mathrm{lab}} = -\Delta_{\mathrm{c}}^{\mathrm{lab}} + (k_{\mathrm{p}} - k_{\mathrm{c}})v \approx -\Delta_{\mathrm{c}}^{\mathrm{lab}}$). Secondly, (ii) appears primarily due to the crossing of the probe resonance with the resonances described by equation 4.2 with $m = \pm 2$ (dot dashed lines). More generally, resonances involving even number of coupling photons do not depend on the coupling detuning, and all cross at $v_z = 0$, $\Delta_{\mathrm{p}}^{\mathrm{lab}} = 0$. As a result, we predict and observe a probe transparency around resonance, which is strongly independent of the coupling detuning. Experimentally, we see that the transparency does not occur exactly at $\Delta_{\mathrm{p}}^{\mathrm{lab}} = 0$. This can be understood as the light-shift of state $|1\rangle$ due to coupling of the states $|1\rangle$ and $|2\rangle$ by the off-resonant coupling field. We therefore expect the shift to reduce with increasing coupling detuning, which is observed experimentally [figure 4.7(a)]. Finally, (iii) is associated with a four-photon transition occurring when the probe resonance crosses the resonance described by equation 4.1 with $m = -3$. Although there are in theory infinitely many resonances involving an infinite number of coupling photons, in practice their amplitude very quickly becomes negligible.

4.5 Summary

In summary we have observed EIA for the first time in a non-degenerate three-level ladder system, demonstrating that a 4-level system is not required to observe EIA. Our model, adapted from [109], shows excellent agreement with experimental transmission spectra and clearly reveals the origin of enhanced absorption in these systems where fast velocity classes contribute strongly to the overall absorption.

Switching on the co-propagating field also leads to a change from normal to anomalous dispersion, which allows for switching between subluminal and superluminal propagation of pulses in the medium. Indeed, such an observation

merits further investigations of pulse propagation in media exhibiting this type of EIA, however these are beyond the scope of this thesis.

In the following chapter we extend our investigation to four levels coupled by three driving fields, under which conditions we observe the appearance of another nonlinear phenomenon, four-wave mixing.

Chapter 5

Four-wave mixing (FWM)

This chapter is based on the following publication:

D. J. Whiting, R. S. Mathew, J. Keaveney, C. S. Adams, and I. G. Hughes, *Four-wave mixing in the hyperfine Paschen-Back regime*, to appear in Journal of Modern Optics arXiv:1705.01855.

5.1 Introduction

Continuous resonant driving of a 2-level atomic medium sets up spatial and temporal polarisation oscillations in the medium [6] (called a *spin wave*). These polarisation oscillations lead to the emission of an EM-field that has the same frequency as the driving field but is exactly out of phase. The destructive interference between the two leads to the extinction of the driving field which we have so far described by the "absorption" coefficient α.

In a system of four atomic levels (and four dipole transitions) coupled by three-driving fields (figure 5.1), a component of the atomic polarisation oscillates at the sum or difference frequency of the driving fields, leading to the emission of light on the uncoupled transition. This process is called non-degenerate four-wave mixing (FWM) [111].

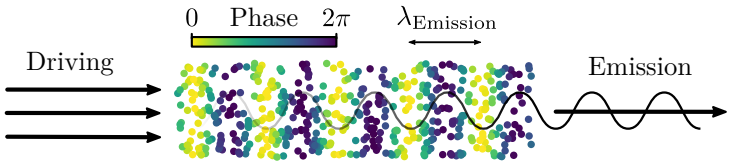

Figure 5.1: Illustration of a spin wave. Under phase-matched conditions the driving fields create a polarisation grating (spin wave) with a period equal to the wavelength of the emitted light, leading to highly directional emission.

FWM continues to generate much interest within the atomic physics community, with a growing list of applications that include: precision spectroscopic measurements [112]; displacement measurements in electro-mechanical cantilevers [113]; investigations of motional dephasing [114] and photon storage [115] in pulse-seeded Rydberg systems; producing correlated photon-pairs and single-photons [116, 21] for use in quantum information protocols; relative intensity squeezing [117]; creating entangled imaging systems [118] and transspectral transfer of orbital angular momentum carrying light fields [119].

In a spatially-extended medium, where the dimensions of the atom-light interaction region are greater than the wavelength of the light, the radiation pattern of the emitted field depends on the spatial variation of the driving fields. Under so-called phase-matched conditions, the fields emitted by all atoms add constructively in a particular direction (illustrated in figure 5.1). This phase-matching criterion is key to many of the applications of FWM.

The phase-matching condition takes the form of momentum conservation for the incoming and outgoing photons. Depending on the particular level scheme and wavelengths, there are a variety of configurations of beam angles that fulfil this criteria. Various arrangements of energy levels have been used to generate FWM: the double lambda [120, 121, 122, 123, 21]; double ladder [124, 125, 75] and the diamond [126, 74, 127] schemes being the most widely reported. In our case we will consider the diamond energy-level scheme in rubidium[1] that is shown in figure 5.2(a). This diamond scheme has the

[1]Note that we have changed to using the $5D_{3/2}$ state as the $5P_{1/2} \rightarrow 5D_{5/2}$ transition is electric dipole forbidden.

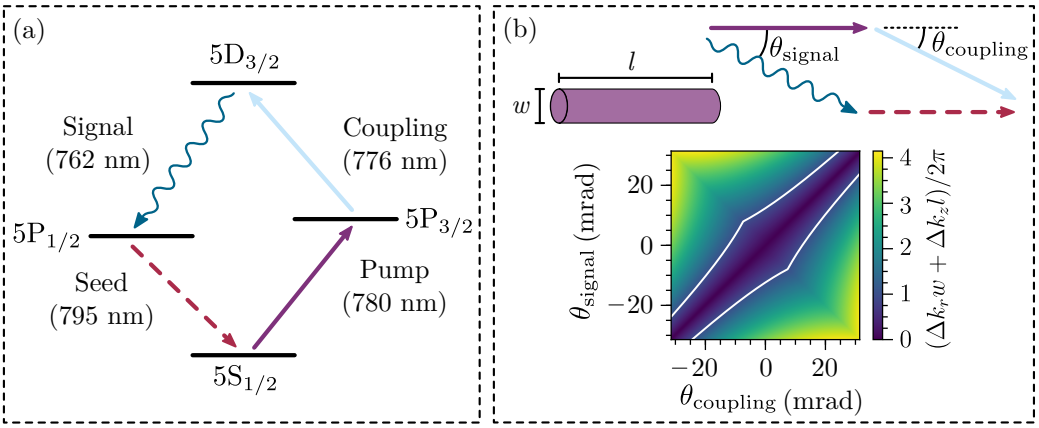

Figure 5.2: Four-wave mixing scheme. (a) Diamond energy-level configuration in rubidium. (b) Phase matching configuration with small angles θ_{coupling} and θ_{signal}. The phase mismatch over the cylindrical interaction region (with diameter w and length l) for different beam angles. The solid white lines are a contour marking a phase-mismatch equal to 1.

advantage that the emitted field (signal) with a wavelength of 762 nm can be easily separated from the background of the driving fields with wavelengths of 780 nm (pump), 776 nm (coupling) and 795 nm (seed). This can be achieved simply with the use of narrowband interference filters as opposed to the significantly more complex optical cavity based filter methods [128].

In our experiment we use a geometry with all four fields propagating in the forward direction [shown in figure 5.2(b)]. In this geometry perfect phase-matching is achieved by having all four fields exactly co-propagating. In practice it is not necessary that perfect phase matching be achieved, only that for all positions in the interaction region $\vec{r}$, the phase mismatch $|\Delta\vec{k}\cdot\vec{r}| \ll \pi$, where the wavevector mismatch $\Delta\vec{k} = \vec{k}_{\text{p}} + \vec{k}_{\text{c}} - \vec{k}_{\text{signal}} - \vec{k}_{\text{seed}}$. The pump and seed beams are perfectly overlapped on a polarising beam splitter and the coupling beam is set up to cross at a small angle θ_{coupling} which enables easy separation of the beams after the vapour cell. For the 2 mm long vapour cell and beams waists of approximately 50 μm that are used in the experiment, the interaction region is roughly cylindrical. The phase-matched angles for signal emission are shown in figure 5.2(b) as a function of the angle θ_{coupling}. The solid white lines are a contour marking $\Delta k_r w + \Delta k_z l = 2\pi$, where $\Delta k_{r,z}$

are the radial and axial components wavevector mismatch respectively and $w = 50$ μm and $l = 2$ mm are the dimensions of the interaction region. From this it is clear that the phase-matching requirement is relatively relaxed in this geometry: the coupling beam angle can be changed significantly and the phase-matching dictates that the signal beam (762 nm) is emitted at the same angle.

In this chapter we will use a 0.6 T magnetic field to enter the HPB regime, and comprehensively characterise four-wave mixing in this regime. Further, we will show that in this regime the observed FWM signals can be mapped to an isolated four-level system that can easily be modelled using only simple 4-level optical Bloch equations.

In figure 5.3 we show the general principle of the experiment. In the absence of an applied magnetic field (left), the hyperfine splitting of the $5S_{1/2}$, $5P_{3/2}$, $5P_{1/2}$ and $5D_{3/2}$ terms creates many paths to generate a FWM signal. Four-wave mixing is a coherent process where the electric fields from different paths interfere with one another, complicating the observed FWM signal which becomes difficult to predict. In a thermal atomic vapour, the hyperfine splitting of the 5P and 5D states is smaller than the Doppler width, so many sub-states are simultaneously excited amongst different atomic velocity groups. Additionally, although strong pumping (with high Rabi frequencies) is often desirable in order to obtain high conversion efficiencies, Rabi frequencies similar to the hyperfine structure splitting can also lead to this multi-path interference [127, 70]. The bottom-left panel of figure 5.3 shows an example FWM spectrum illustrating the effect of multiple excitation pathways. However, when a large enough magnetic field is applied (in the HPB regime), adjacent levels in the 5S manifold are separated by much more than the Doppler width and, due to selection rules for electronic transitions, individual two- [40, 45], three- [82, 47] and four-level systems can be coupled separately, as shown on the right of figure 5.3. The FWM signal in this case is much simpler, consisting of an Autler-Townes split doublet that results from the strong dressing by the coupling laser.

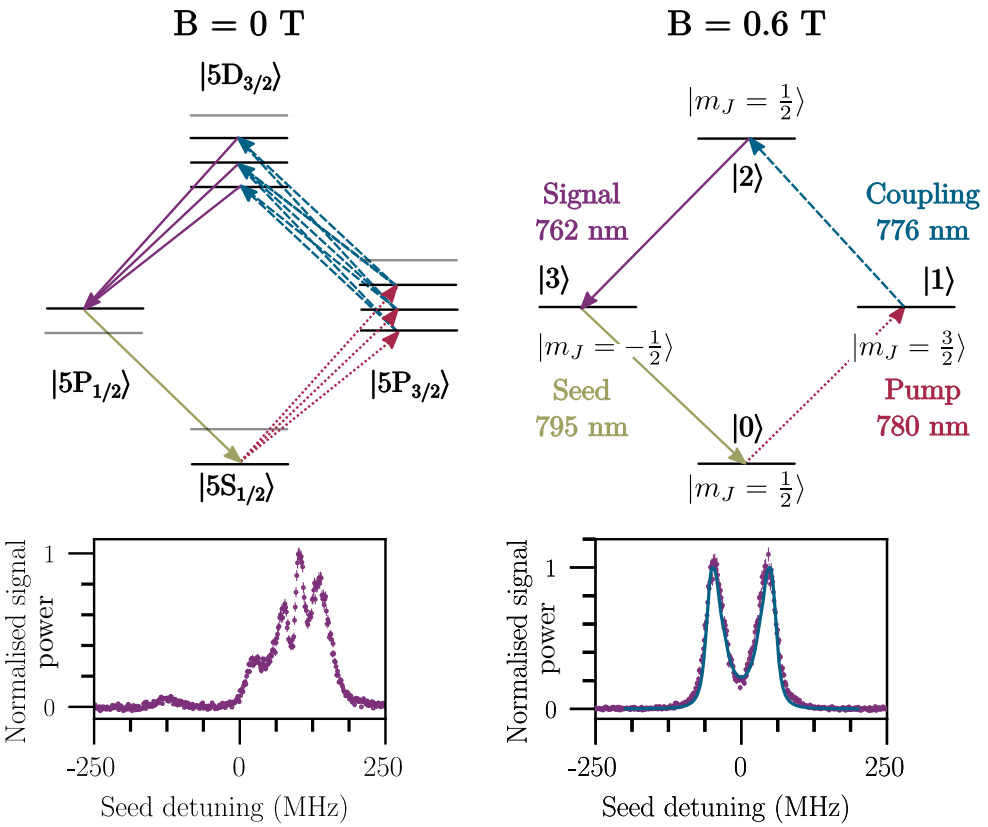

Figure 5.3: Energy levels in the rubidium diamond scheme and example experimental four-wave mixing spectra in the absence (left) and presence (right) of a magnetic field of strength 0.6 T. In its absence, interference along multiple paths results in four-wave mixing spectra that are both highly sensitive to experimental conditions and difficult to model. The magnetic field removes the multiple-path interference, resulting in textbook four-wave mixing spectra that can be quantitatively modelled. The states labelled 0–3 are those used in the model.

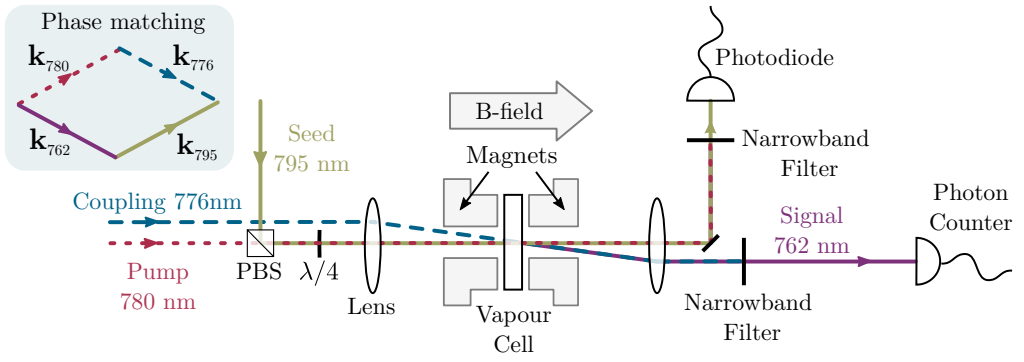

Figure 5.4: Schematic of the experimental setup. Three continuous-wave laser beams are focused through a heated vapour cell of length 2 mm, which contains isotopically enriched ^{87}Rb and is placed in a permanent magnetic field of strength B = 0.6 T directed along the pump beam axis. The coupling beam crosses the pump beam at an angle of 10 mrad (not to scale). The phase-matching condition is fulfilled as shown in the inset. The pump and seed beams are combined on a polarising beam splitter (PBS) and their polarisations are set by a quarter-waveplate ($\lambda/4$).

5.2 Experimental details

A schematic of the experimental setup is shown in figure 5.4. As in previous chapters we use a 2 mm long vapour cell containing isotopically enriched rubidium ($> 98\%$ ^{87}Rb), which is positioned in a permanent magnetic field of strength 0.6 T that is uniform to level of 1 mT (the field profile is discussed in appendix A). The vapour pressure, and hence the atomic number density, is controlled via the cell temperature. In the magnetic field, the circularly polarised pump beam at 780 nm drives the σ^+ transition between the $|5S_{1/2}, m_J = \frac{1}{2}\rangle$ and $|5P_{3/2}, m_J = \frac{3}{2}\rangle$ states. The pump beam is overlapped in the cell with the coupling (776 nm) and seed (795 nm) beams, which drive the $|5P_{3/2}, m_J = \frac{3}{2}\rangle \rightarrow |5D_{3/2}, m_J = \frac{1}{2}\rangle$ and $|5S_{1/2}, m_J = \frac{1}{2}\rangle \rightarrow |5P_{1/2}, m_J = -\frac{1}{2}\rangle$ transitions, respectively. Only states with $m_I = \frac{3}{2}$ are resonantly coupled by the driving fields. In order to achieve the necessary high intensities, the driving fields are focussed by a plano-convex lens with a 200 mm focal length to $1/e^2$ radii of between 50 μm and 60 μm at the centre of the cell. The phase-matching condition is fulfilled as shown in the inset of figure 5.4. The pump

and seed beams are co-propagating, whilst the coupling beam crosses at a small angle. This is so that the signal and seed beams can be easily separated from the pump and coupling beams by the use of narrowband interference filters. The signal beam is detected using a photon counting module and the transmitted seed light is measured on a high gain photodiode. The pump and seed powers are set to 1 μW whilst the coupling power is 34 mW. These correspond to peak Rabi frequencies of approximately 10 MHz and 180 MHz respectively. The relatively low Rabi frequencies on the D_1 and D_2 lines are chosen to be close to the saturation intensities of these transitions whereas the larger Rabi frequency of the coupling field is necessary to display the effect of Autler-Townes splitting on the four-wave mixing spectrum.

5.3 Four-level model

We model a system of four-levels $|0-3\rangle$, labelled anti-clockwise from the ground-state in figure 5.3, interacting with three CW driving fields with Rabi frequencies Ω_p, Ω_c, Ω_seed and detunings Δ_p, Δ_c, Δ_seed. Note that these are angular detunings whereas linear detunings ($\Delta/2\pi$) are used in the spectra that appear in the following figures. We write the interaction Hamiltonian (in the rotating wave approximation) as

$$\hat{H} = \frac{\hbar}{2}\begin{pmatrix} 0 & \Omega_\mathrm{p} & 0 & \Omega_\mathrm{seed} \\ \Omega_\mathrm{p} & -2\Delta_\mathrm{p} & \Omega_\mathrm{c} & 0 \\ 0 & \Omega_\mathrm{c} & -2(\Delta_\mathrm{p}+\Delta_\mathrm{c}) & 0 \\ \Omega_\mathrm{seed} & 0 & 0 & -2\Delta_\mathrm{seed} \end{pmatrix},$$

and solve the Lindblad master equation to find the steady-state density matrix ρ. The atomic polarisation density at any point can be expanded in the usual way (equation 2.3) as

$$\vec{P} = N\langle\hat{d}\rangle = N(\vec{d}_{01}\rho_{10} + \vec{d}_{12}\rho_{21} + \vec{d}_{03}\rho_{30} + \vec{d}_{32}\rho_{23}), \tag{5.1}$$

where for simplicity we have included only the positive frequency components of the dipole allowed transitions. The component of the polarisation that oscillates at the frequency of the signal transition ω_{signal} is $\vec{P}_{\text{signal}} = N\vec{d}_{32}\rho_{23}$. The oscillating dipoles radiate an electric field with a strength proportional to $\vec{P}_{\text{signal}}$. The total radiated field will be the sum of the fields emitted from each atom, and thus the intensity will be proportional to $|\sum_n \rho_{23}|^2$ where the sum is over all atoms. In general one should consider the back-action of the emitted field on the atoms. However, in our case the emitted field is weak enough to ignore any back-action. Additionally, we find that we do not need to consider any propagation effects (absorption and dispersion) on the emitted field as the polarisation, and thus the refractive index, is sufficiently small. We do however need to take into account three effects in calculating the total radiated field. Firstly, we must sum over all the atomic velocity classes which experience different, Doppler-shifted, detunings of the driving fields. Secondly, the pump and seed fields experience a significant amount of absorption on propagation through the medium. We calculate their respective absorption coefficients from the density matrix elements ρ_{10} and ρ_{30} as described in section 2.1.3, and propagate them through the medium. Finally, we find it is necessary to sum over the radial intensity profiles of the driving fields. We do this by assuming that all of the driving fields have Gaussian intensity profiles in the radial direction r (which is consistent with our measurements) and are perfectly overlapped. The radiated field is then calculated for radial shells over which constant intensities can be assumed. In the experiment we detect the signal using a single-mode optical fibre and a photon counting module. The effect of the optical fibre collection is modelled as a Gaussian spatial filter acting on the emitted FWM field and therefore we calculate the theoretical signal amplitude as

$$S \propto \int_0^\infty |\langle\rho_{23}\rangle|^2 \exp(-2r^2/w_{\text{D}}^2)\ r\text{d}r, \tag{5.2}$$

where $w_{\text{D}} \sim 90\ \mu$m is the measured waist of the optical fibre detection mode at the position of the cell, and the angled brackets $\langle\rangle$ refer to integration over the velocity distribution and the length of the medium in the propagation

direction.

5.4 Results

Figure 5.5 shows a typical spectrum as the seed laser frequency is scanned. In panel (a) we show, for reference, a theoretical transmission spectrum [29] of the Rb D1 line with (solid line) and without (dashed line) the applied magnetic field. Note that the spectrum without field is for a naturally abundant vapour cell while the spectrum with field is for an isotopically enriched ^{87}Rb cell. Zero detuning is the weighted D1 line centre of naturally abundant rubidium in zero magnetic field [80]. In panel (b) we scan the seed laser over the leftmost absorption line [unshaded region in panel (a)] and measure its transmission spectrum in the absence of the pump and coupling fields (olive dashed line). Adding the resonant 780 nm pump beam (red dotted line) creates a V-system which exhibits a small peak at line-centre due to EIT. When the strong coupling laser is also added (blue solid line), it dresses the pump transition and the EIT feature is split into an Autler-Townes doublet. Where the three lasers are resonant with the dressed states of the system, we observe a FWM signal, shown in panel (c). The maximum FWM signal coincides in frequency with the position of the Autler-Townes doublet in panel (b). The combined use of narrowband interference filters and photon-counting modules to detect the FWM signal yields a high signal-to-noise ratio. This is necessary because we use a low temperature and low pump and seed powers, resulting in a small absolute FWM signal (pW). Experimentally we observe that changing the alignment of the beams modifies the lineshapes; we conjecture that this is due to the presence of back-reflections since the cell is not anti-reflection coated. We optimise the alignment to ensure that the Autler-Townes splitting is maximised.

We now look at how the observed FWM signal changes with a selection of the experimental parameters. The complete parameter space is too large to fully explore here, but we show the results of a range of experiments along

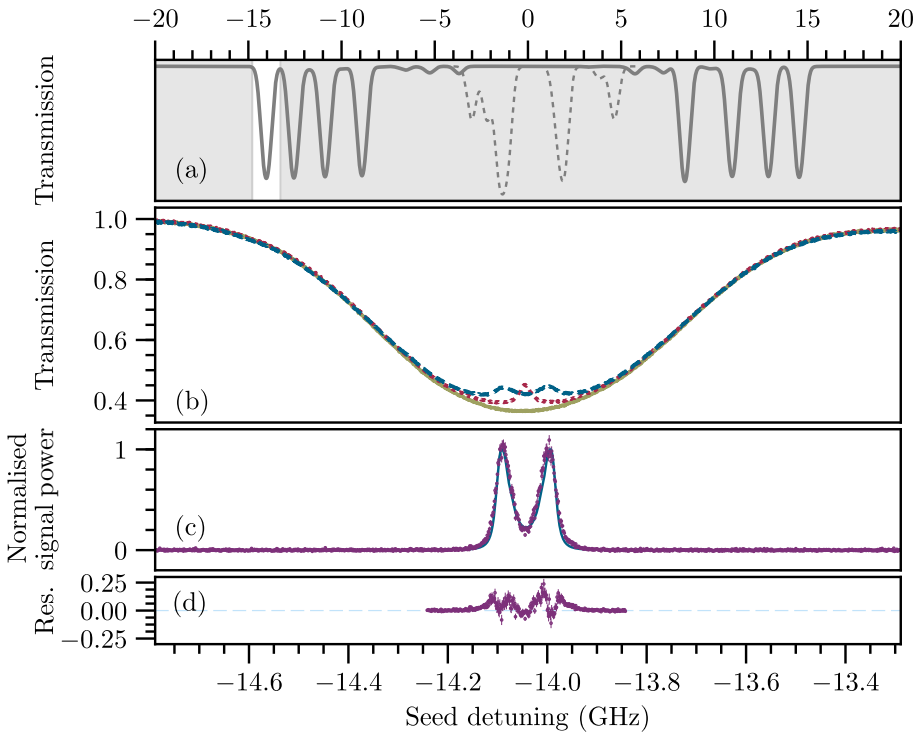

Figure 5.5: (a) Theoretical transmission spectrum of the rubidium D1 (795 nm) line in the presence (thick grey line) and absence (dotted grey line) of a 0.6 T magnetic field at a temperature of 80°C. The shaded region highlights the detuning range for the experimental data shown below. (b) Experimentally measured seed laser transmission spectra. The seed-only spectrum is displayed by the solid olive line. Switching on a resonant pump laser results in V-type EIT resonance (red dotted line). Additionally switching on a resonant coupling laser (dashed blue line) splits the EIT feature as a result of the strong dressing of the $5P_{3/2}$ state. (c) Four-wave mixing spectrum where the splitting is also evident; the solid line is the model as given by Eq. (5.2), with $\alpha = 35$ and Ω_c reduced by 14% from the measured value. (d) Residuals (experiment minus theory) are plotted (Res.).

with the theoretical model demonstrating the success of the 4-level model in the HPB regime.

5.4.1 Model parameters

The natural decay rates of the relevant atomic states are $\Gamma_{10} = 2\pi \times 6$ MHz, $\Gamma_{30} = 2\pi \times 5.7$ MHz, $\Gamma_{21} = 2\pi \times 0.17$ MHz, $\Gamma_{23} = 2\pi \times 0.43$ MHz and $\Gamma_{20} = 2\pi \times 0.07$ MHz [110]. In the model, the decay rates Γ_{21}, Γ_{23} and Γ_{20} are multiplied by a factor α which includes contributions from broadening of the excited-state transitions due to collisions with background gases [79] and the effect of magnetic field inhomogeneity. We find good agreement with the experimental spectra using a value of $\alpha = 35$, corresponding to an additional broadening of ~ 20 MHz, which is in agreement with previously measured values [47]. We have independently measured the collision-broadened linewidths $\Gamma_{10}/2\pi, \Gamma_{30}/2\pi = 13$ MHz and so these values are fixed in the model.

The blue line in figure 5.5 panel (c) shows the results of the model using independently determined values of all parameters except for: Ω_c, which has been reduced by 14% from the value calculated using the measured Gaussian beam waist, $\alpha = 35$ and an overall scaling factor. Given the lack of free-parameters we find that the model is in excellent agreement with the data as indicated by the small residuals. However, there is clearly additional broadening of the lines that is not currently accounted for by the model. We expect that the main source of discrepancy between experiment and theory is that the model used to account for the optical fibre collection mode is not sufficiently detailed. Other possible sources of discrepancy include imperfect alignment of the driving fields (perfect overlap is assumed in the model), the fact that we do not consider a full propagation model, e.g. the Maxwell-Bloch model [129], that fully accounts for back-action of the medium on the driving fields as they propagate. The relative simplicity of our system, with only 4 coupled atomic levels, means that it could be an ideal test-bed for such models.

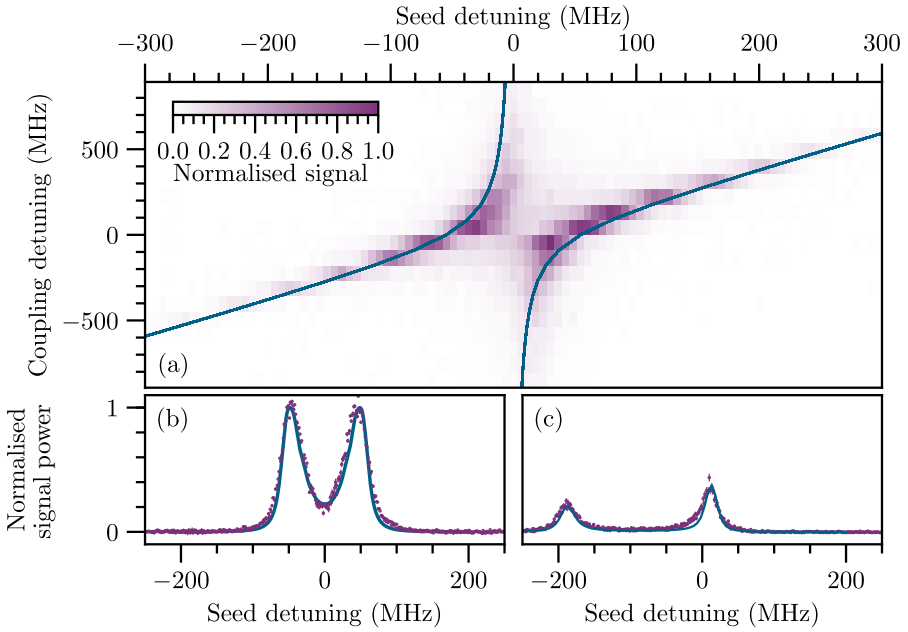

Figure 5.6: Four-wave mixing signal as a function of both coupling (776 nm) and seed beam (795 nm) detunings. The system exhibits an avoided crossing, which is characteristic of Autler-Townes splitting. The solid lines in the panel (a) are a plot of $\Delta_{\text{seed}} = k_{\text{seed}} v_{2\text{photon}}$ where $v_{2\text{photon}}$ is given by Eq. (5.3). Panel (b) and (c) show the FWM signals at coupling detunings of 0 MHz and -360 MHz respectively, where the solid lines are the model as given by Eq. (5.2) with $\alpha = 35$ and Ω_c reduced by 14% from the measured value.

5.4.2 Dependence on coupling detuning

In figure 5.6 we plot the normalised signal level against the detunings of both coupling and seed lasers. The strong coupling laser dresses the pump transition, creating two pathways to the 5D state. Hence we observe two features in the FWM signal that correspond to the resonances with these dressed states. In the limit of low Ω_c and low Ω_{seed}, the seed laser weakly probes the two-photon absorption resonance $|0\rangle \rightarrow |2\rangle$. For a resonant pump laser (Δ_c) the atoms that are two-photon resonant have axial speeds (equation 3.5)

$$v_{2\text{photon}} = \frac{\Delta_c k_c}{a} \pm \sqrt{\frac{\Delta_c^2 k_c^2}{a^2} + \frac{\Omega_c^2}{2a}}, \tag{5.3}$$

where $a = 2(k_p^2 + k_p k_c)$.

In figure 5.6 we plot $\Delta_{seed} = k_{seed} v_{2photon}$ [solid blue line in panel (a)] where k_{seed} is the seed transition wavenumber and Ω_c is the measured peak Rabi frequency reduced by 14% for the coupling beam. The model agrees reasonably well with the positions of the FWM resonances, as is expected for seed and pump Rabi frequencies that are significantly smaller than the coupling Rabi frequency, but there is a clear overestimation of the Autler-Townes splitting for $\Delta_c = 0$. This is to be expected since the total FWM signal is obtained from the entire spatial profile of the coupling field, resulting in a reduced effective Rabi frequency.

5.4.3 Dependence on coupling power

The dressed-state resonance frequencies depend on both the coupling detuning (figure 5.6) and also the coupling laser power, which is plotted in figure 5.7. The coupling laser Rabi frequency, Ω_C, is proportional to the square-root of the coupling laser power. When the pump and coupling lasers are both on resonance with the bare atomic states, the dressed states are symmetrically split, with the well-known Autler-Townes splitting energy $\hbar\Omega_C$ [6].

The dotted lines in figure 5.7(b) show the expected square-root behaviour of the splitting with laser power, which coincide well with the observed peak FWM signals. Note these dotted lines are a guide to the functional form of the splitting, not a fit to the data. Note also that since the seed and coupling lasers are not actively frequency stabilised there is some drift of the laser frequencies between measurements (typically on the order of 100 MHz per hour). In the case of the displayed data we have attempted to correct for the drift of the seed laser in post-processing by fitting the centre frequency of the broad Gaussian line shapes in the (simultaneously measured) seed transmission spectra.

As the coupling laser power is increased, the dressed-state energy levels split as expected, but the peak power of the FWM signal quickly saturates.

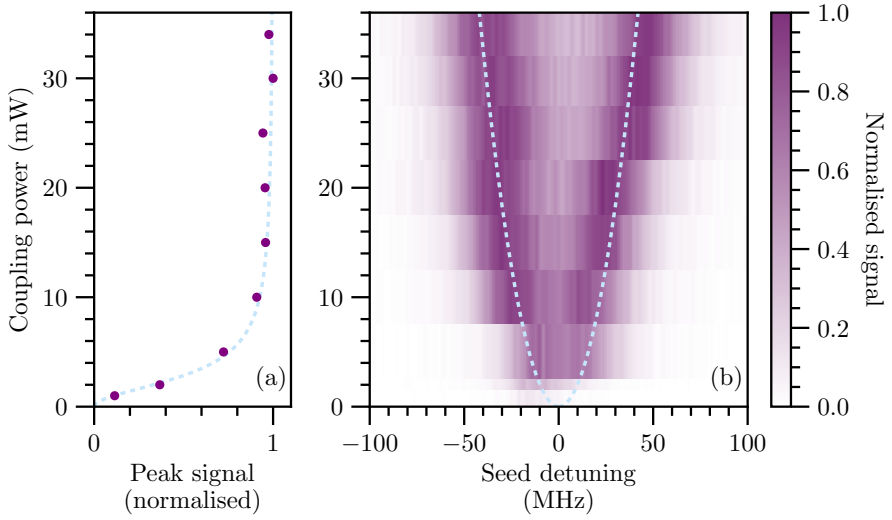

Figure 5.7: (a) Four-wave mixing signal as a function of the coupling beam power, with pump and coupling fields on resonance with the bare atomic transitions. For powers larger than ~ 10 mW the signal saturates, but the spectral dependence on seed detuning in panel (b) continues to evolve. Autler-Townes splitting is clearly visible as the coupling power increases and shows the expected square root dependence as shown by the dashed lines. The seed detunings have been shifted to correct for the frequency drift of the seed laser.

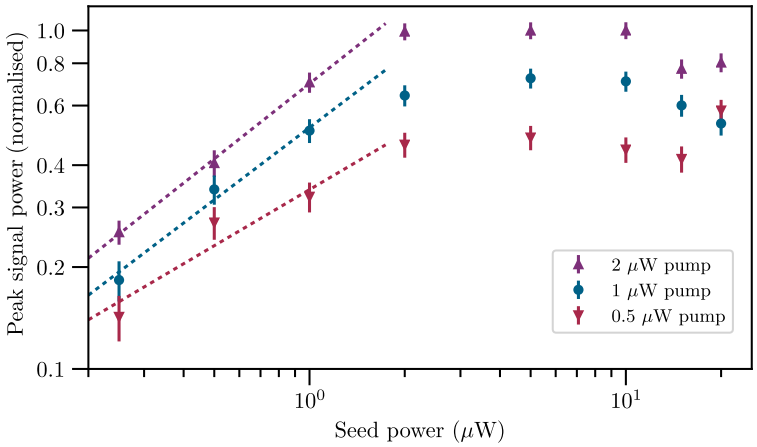

Figure 5.8: Four-wave mixing signal as a function of the power of the seed beam. The three curves correspond to pump powers of 2 μW (purple ▲), 1 μW (blue •) and 0.5 μW (red ▼). After an initial sharp rise in signal with seed power, the signal saturates. The peak signal power at saturation is higher for the different pump powers, however the saturation point is unchanged. The dashed lines are power-law fits to the lowest three powers of each data set.

This fits well to a simple saturation model given by $1 - \frac{1}{(1+P^2/A^2)}$ with fit parameter $A = 2.8 \pm 0.1$ mW, and physically corresponds to the saturation of the number of excitations in the medium for given values of both seed and pump laser power [dotted line in figure 5.7(a)].

5.4.4 Dependence on seed power

Figure 5.8 shows the peak signal intensity as a function of seed power, for 3 different pump powers. Increasing the seed power initially results in a sharp increase in the FWM signal, but this quickly saturates after a seed power of around P_{sat}= 2.5 μW. Fitting the initial increase to the (power law) function αP^β with free parameters α and β, results in the dashed lines shown in figure 5.8. For the pump powers of 2 μW, 1 μW and 0.5 μW the fitted values of the exponent β are 0.74 ± 0.03, 0.7 ± 0.1 and 0.6 ± 0.1 respectively.

With additional pump power, the peak signal increases, but P_{sat} does not change. For very high seed powers, the signal decreases which we attribute to power broadening of the pump transition.

5.4.5 Dependence on atomic number density

In figure 5.9 we plot the resonant FWM signal power as a function of atomic number density, with the corresponding vapour temperature on the bottom axis (the abscissae are the same for both panels). The total emitted electric field scales linearly with the number of atoms since FWM is a coherent effect. Therefore the signal intensity initially scales quadratically with atomic density [solid blue line in panel (a)]. A quadratic fit (i.e. with an exponent of 2) for the data in the unshaded region in panel (a) yields a reduced chi-squared value of 0.1 [81], indicating a good fit. If the exponent is allowed to vary in the fit, we obtain a best-fit exponent of 2.1 ± 0.3. Outside of this region, at densities above $\sim 5 \times 10^{18}$ m^{-3} (temperature around 90°C), the 2 mm long vapour becomes optically thick for the ground state transitions, and this reduces the FWM signal, since the resonant pump and seed beams on the D2 and D1 transitions are strongly scattered by the medium. The extinction can be described by the Beer-Lambert law. When phase-matching is present, the total electric field from all atoms is simply the constructive superposition of the individual fields. The intensity is then given by [130]

$$I \propto \left(\frac{N}{d_{\text{opt}}}\right)^2 \left[1 - \exp\left(-\frac{d_{\text{opt}}}{2}\right)\right]^2, \tag{5.4}$$

where the medium has a density N and optical density d_{opt}.

The dotted blue line in panel (a) indicates reasonable agreement with the model described by Eq.(5.4). With the same optical depth, we expect transmission of the driving fields given by the dotted blue line in panel (b). Although the functional form of the model agrees with the measured seed transmission (yellow circles), the model predicts a higher optical density at any given cell temperature. In the experiment, both seed and pump lasers are being strongly

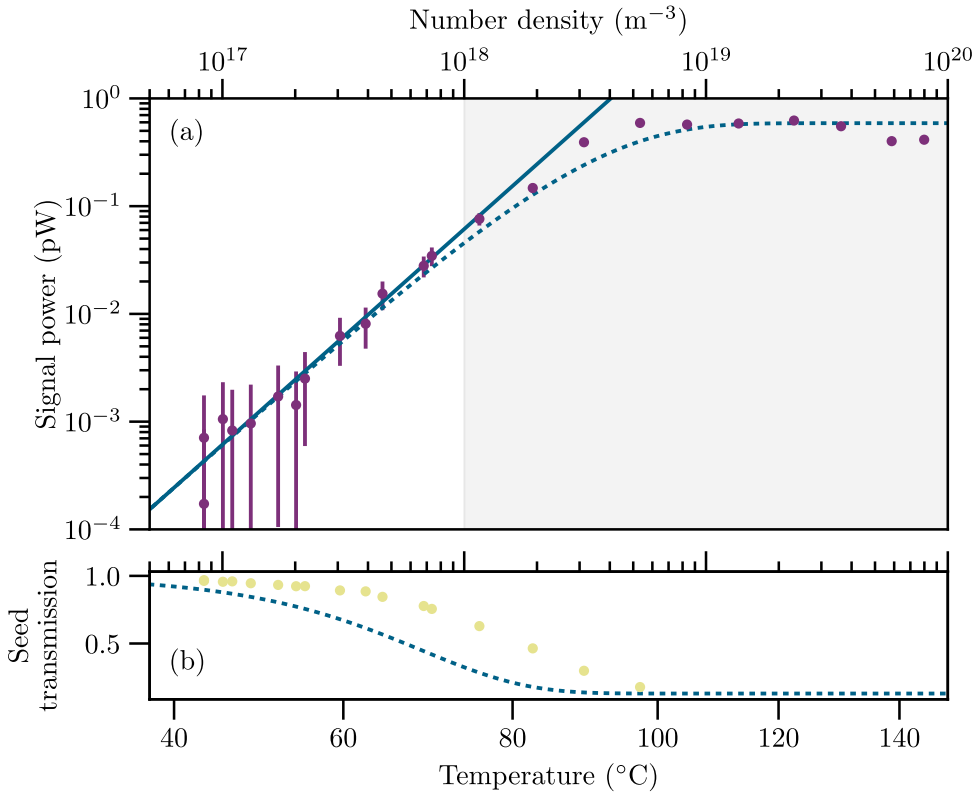

Figure 5.9: Resonant FWM peak power and seed transmission as a function of atomic number density and temperature. After an initial quadratic rise (solid blue line), the maximum signal is reached at a temperature of $\sim 90°C$. The dotted line in (a) is a fit using equation 5.4 and shows good agreement with the data. Comparing the extracted optical depth from this model [dashed line in (b)] suggests the saturation is caused primarily by the pump laser absorption, rather than the seed absorption [olive points in (b)].

absorbed by the vapour, with the pump being more strongly absorbed (the D_2 line is stronger than the D_1 line). Clearly, a model that takes into account the absorption of both seed and pump lasers is required in order to expect better agreement with the experimental data.

5.5 Summary

We have presented an experimental study of seeded non-degenerate FWM in the HPB regime where the relevant atomic energy levels are reduced to a simple four-level system. The applied magnetic field removes multi-path interference and therefore allows for quantitative agreement with a simple theoretical model, based on 4-level optical Bloch equations, even in the regime of strong driving. We have investigated how the FWM signal depends on laser detunings, powers and the atomic density of the vapour, finding excellent agreement between theory and experiment. This study adds to previous related works [82, 47] demonstrating how many nonlinear optical phenomena can be simplified in thermal vapours by the application of a large magnetic field, allowing for detailed quantitative modelling. Following on from the development of a range of technologies based on linear atom-light interactions [131, 41, 42, 43], we envision that similar comprehensive modelling of nonlinear systems will enable the design and optimisation of future devices.

Chapter 6

Heralded single-photon generation

This chapter is based on the following publication:

D. J. Whiting, N. Šibalić, J. Keaveney, C. S. Adams, and I. G. Hughes, *Single-photon interference due to motion in an atomic collective excitation*, Physical Review Letters **118**, 253601 (2017), 10.1103/PhysRevLett.118.253601.

6.1 Introduction

The engineering of quantum states is a critical component in the development of quantum technologies, such as quantum communication and computation [132, 133], quantum simulation [134, 135] and quantum metrology [136]. Optical quantum states are of particular interest in quantum information transfer because of their typically weak interactions with the environment, meaning they can be transmitted over large distances without significant losses. The generation of optical quantum states also has important consequences for fundamental physics research. Historically, the development of sources of single photons, based on radiative atomic cascades and spontaneous

parametric down conversion (SPDC), enabled some of the first experiments on the quantum nature of light: quantum interference of single photons [137, 138] and Hong-Ou-Mandel interference [139]. More recently, squeezed light has been employed to improve the sensitivity of the LIGO instrument in the detection of gravitational waves [140]. For these reasons, optical quantum state engineering continues to be a rapidly growing field of research spanning a wide range of subject areas within physics. Each having their own advantages and disadvantages, there are a veritable smorgasbord of emerging technologies.

Sources of engineered quantum states fall broadly into two categories: those that are heralded, and those that are on-demand. In a heralded source the state preparation is inherently stochastic but is temporally correlated with a measurable 'herald' event, i.e. the detection of a herald signals the preparation of the state. These sources usually operate at low enough rates to reduce the likelihood of more than one emission event occurring simultaneously, thereby modifying the heralded state. In contrast, on-demand sources are much sought-after since they hold the potential for much higher rates of communication and computation.

In the solid-state [141], quantum dots [142] and nitrogen vacancy centres [143] hold tremendous potential as on-demand sources, however there are still major obstacles to be overcome. One challenge is to achieve reproducibility of the devices: the typical production method involves the manufacture of many devices and the ones with the desired properties are post-selected. Another challenge is that the spectral widths of the generated optical states are typically several THz [142]. Apart from resulting in a low spectral brightness (the number of photons per second per unit bandwidth), this limits their compatibility with many existing technologies, including atomic quantum memories. In order to interface efficiently with atomic systems, the photon spectrum should be compatible with the atomic transition in both its bandwidth (typically < 1 GHz) and central frequency. Some progress has been made to reduce the bandwidth by inserting these devices inside high-finesse optical cavities [144] or by using narrowband atomic filters based on the

Faraday effect [145]. However, these methods are based on filtering a portion of a wider bandwidth and come at the expense of increased experimental complexity.

Atomic media are an attractive alternative [20], with well-defined optical transitions, long coherence times, strong nonlinearities that produce controllable phase shifts [28] and established coherent control protocols based on slow-light and adiabatic following [4].

Trapped single atoms [146] and ions [147] are an obvious choice for on-demand single-photon production since preparation in an excited state guarantees the emission of one and only one photon. Unfortunately the emission can be difficult to collect efficiently, since the radiation modes (e.g. dipole modes) have a large spread in angles. The more loss that is introduced into the collection, the more stochastic a source becomes, losing its on-demand character. The collection efficiencies that have been attained to-date are typically on the order of 1% [146]. A solution exists in the form of trapping the single atom [148, 149] or ion [150] inside a high finesse optical cavity. Within the modes of the cavity, the density of states of the atomic emission pattern is increased, hence the photons have a higher probability of being emitted into a cavity mode, with increased collection efficiency. Another interesting method involves trapping a single ion at the focus of a parabolic mirror, allowing the full dipole emission pattern of the ion to be collected with high efficiency [151].

A completely different approach is to use extended atomic media: thermal vapours and cold trapped ensembles. Since these sources usually contain many independent emitters, the state preparation is stochastic and must be heralded, rather than on-demand. However, the emitted photons are naturally frequency and bandwidth matched to atomic quantum memories, enabling the conversion from a heralded source into an on-demand source [27]. A major advantage of such schemes is that through collective interactions with the same free-space optical modes, the atoms can preferentially emit photons in a single direction, negating the need to use high finesse optical

cavities [152]. Another advantage is that the state preparation is highly robust to single-atom loss, due to the large numbers of atoms involved in the state-generation. Finally, it is pertinent to mention experiments that involve extended atomic media, but which also make use of the Rydberg blockade phenomenon, in an effort to achieve on-demand single-photon generation. That the medium is extended allows for collectively enhanced emission into a single direction while the Rydberg blockade guarantees that only a single atomic excitation exists within the medium [153, 65].

While methods involving room-temperature atomic vapours currently lack the high levels of control that can be gained by the cooling and trapping of atoms, they have the very important advantage of being easily scalable, since they do not rely on cryogenic cooling or vacuum chambers. This scalability has led to the development of many practical devices including chip-scale atomic clocks [30], brain sensors [31] and microwave electrometers [33]. For this reason, optical quantum-state engineering in thermal atomic vapours is already an established field of research. One of the most significant early advances in this field was the development of the double-lambda scheme in alkali-metal atoms [120, 154]. Experiments on this front have reported high levels of relative intensity squeezing, high-brightness single-photon sources [21] and quantum memories [24, 25, 26]. Significantly less research has been done on state-engineering using ladder excitation schemes, which, when involving Rydberg states, have the aforementioned potential to be on-demand sources. One notable example of work in this field is the development of a heralded source of telecomms-wavelength single photons [22].

Motion-induced dephasing [155] often inhibits the wider use of thermal atomic vapours in quantum state engineering applications. Because of the broad atomic velocity distribution, the prepared states typically have very short coherence times ($<$1 ns). Doppler-selective excitation schemes may be used in order to reduce the amount of dephasing. However, in such schemes it is not normally possible to address individual atomic states in a controlled manner, due to the hyperfine structure being unresolved within the Doppler-broadened absorption lines. One solution is to use optical pumping to initially prepare

the system in a single hyperfine ground-state, using buffer gases [156] or anti-relaxation coatings [157, 158] to mitigate decoherence processes. Unfortunately, for schemes relying on excited state coherence [79] or thin-cells [159] these methods cannot usually be applied. Buffer-gases lead to additional broadening of excited-state transitions [79] and vapour-cell coatings do not work at the high temperatures required to achieve usable optical densities in thin-cells [160, 78]. In these situations, an alternative solution is to apply a strong magnetic field (to achieve the HPB regime) that resolves the individual transitions (as in the previous three chapters, where this approach resulted in enhanced control of EIT, EIA and FWM).

In this chapter we investigate the generation of single-photons using a thermal rubidium vapour in the HPB regime. Using a Doppler-selective excitation scheme with strong laser-dressing, we prepare a novel quantum state that consists of a single excitation as a robust collective superposition of two velocity classes. The single excitation is emitted as a *single photon with two frequencies*. At present there is much interest in these 'bi-chromatic' photons as they could be used to entangle spatially separated quantum memories or perform spectroscopy with small numbers of photons [161, 162]. The arrival times of the single-photons display collective quantum beats [163], demonstrating the coherent nature of the splitting of the single excitation amongst atoms with primarily two different velocities.

6.2 Experimental details

The single-photon generation scheme is based on the nonlinear optical process called spontaneous four-wave mixing (SFWM) [122, 22] and is illustrated in figure 6.1. Following on from the FWM experiment of the previous chapter, the seed laser (795 nm) is removed from the set-up and the medium is left to spontaneously decay from the $5D_{3/2}$ excited state via the "herald" (762 nm) and "signal" channels (795 nm). The reason for this new naming convention will become clear in the course of the following discussion. In the chosen

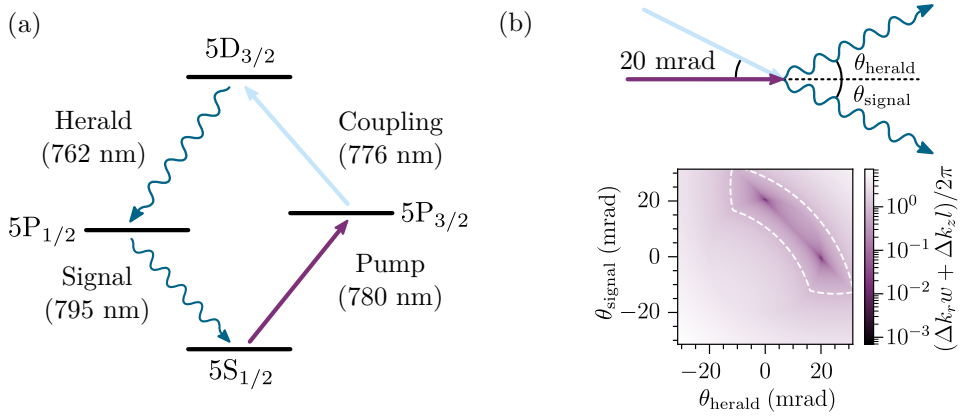

Figure 6.1: Cascade spontaneous four-wave mixing scheme in ^{87}Rb. (a) The energy levels and transition wavelengths used in the experiment. (b) The phase matching scheme with all beams almost co-propagating and the phase-mismatch as a function of the emission angles of the herald (θ_{herald}) and signal (θ_{signal}) photons.

configuration, with pump and coupling lasers almost co-propagating, a steady-state spin-wave is imprinted on the atomic vapour with wavenumber $\approx k_{\text{p}} + k_{\text{c}}$, which is approximately double that of the herald wavenumber k_{h}. This means that there is no phase-matched emission for herald photons: they are emitted uniformly in all directions. However, in the event that a herald photon is emitted in the forward direction, the resulting spin-wave (with wavenumber $k_{\text{p}} + k_{\text{c}} - k_{\text{h}} \approx k_{\text{s}}$) leads to the subsequent phase-matched emission of a signal photon in the forward direction. Figure 6.1(b) shows the herald photon emission angles that lead to phase matched emission of signal photons. The dashed white line indicates the region within which the phase mismatch is less than 2π radians. There are clearly 2 combinations of angles that are very well phase-matched, corresponding to emission in the directions of the two driving fields. Due to this phase-matching condition for photon pairs, detection of the first photon to be emitted announces (*heralds*) the subsequent emission of a photon into the phase-matched direction.

The level structure of ^{87}Rb in the magnetic field is shown in Fig. 6.2 (without the m_I structure for clarity). In the experiment the magnetic field is aligned

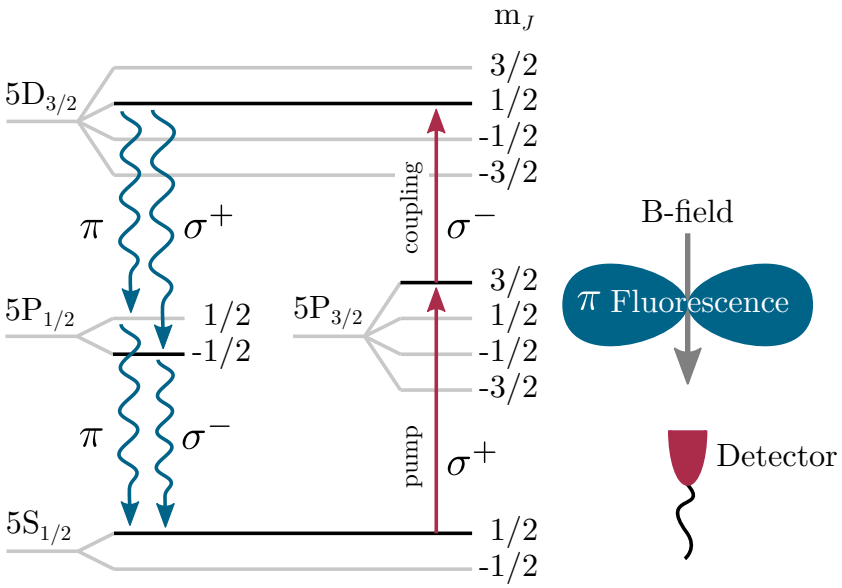

Figure 6.2: Diagram of the atomic energy levels in a large magnetic field and the optical transitions relevant to the experiment. The excited atom can decay back to the ground-state via π or $\sigma^{\pm}$ transitions. However, the applied magnetic field prevents the emission from the π transitions in the direction of the detector.

with the axis defined by the pump laser. The only transitions that can be driven by the pump and coupling fields in this geometry are σ^+ and σ^- transitions. As we have discussed in previous chapters, these transitions are separated from their neighbours in frequency by more than the Doppler broadened linewidths. The pump laser is tuned to drive the $m_I = 3/2$ state with a σ^+ transition from $5\mathrm{S}_{1/2}(m_J = 1/2) \rightarrow 5\mathrm{P}_{3/2}(m_J = 3/2)$ and the coupling laser is tuned to drive the σ^- transition $5\mathrm{P}_{3/2}(m_J = 3/2) \rightarrow 5\mathrm{D}_{3/2}(m_J = 1/2)$. Therefore only the $|5D_{3/2},\ m_J = 1/2, m_I = 3/2\rangle$ state is populated by the driving fields. From here the atoms can spontaneously decay back to the initial ground state via two paths. Because of the magnetic field the atoms that decay via the π transitions cannot emit light in the direction of the detectors. Furthermore, we apply polarization filtering to the signal mode such that only the light from the σ^- transition can be detected. Overall, this means that photons reaching the detectors must come from a single decay pathway and thus, the application of the magnetic field allows the isolation of an ideal 4-level system with which to study single photon generation by SFWM.

A measure of the correlation between the emitted herald and signal photons is called the normalised cross-correlation $g^{(2)}_{\mathrm{h,s}}(\tau)$ [54]. Experimentally this is measured in the following way. The herald and signal photons are collected by single-mode optical fibres positioned in the phase-matched directions: $\theta_{\mathrm{herald}} = 2$ mrad, $\theta_{\mathrm{signal}} = 0$. The fibres connect to single photon avalanche diodes (SPADs) which, upon detection of a photon, output an electronic pulse with a sub 1 ns rise-time and a specified 350 ps timing uncertainty (jitter). The pulse times are recorded by an electronic counting card with a 27 ps timing resolution. The time delays, τ, between herald and signal detection events are then binned to give the correlation function $G^{(2)}_{\mathrm{h,s}}(\tau)$ (also known as the joint detection probability). Finally, the histogram is normalised according to

$$g^{(2)}_{\mathrm{h,s}} = \frac{G^{(2)}_{\mathrm{h,s}}}{r_{\mathrm{h}} r_{\mathrm{s}} T \Delta\tau} \tag{6.1}$$

where $r_{\mathrm{h,s}}$ are the herald and signal channel count rates, T is the total data

acquisition time for the experiment and $\Delta\tau$ is the width of the histogram time bins. The normalised correlation function measures the probability of detecting a signal photon at time $t + \tau$ conditional on detection of a herald photon at time t, compared to the same probability when there is no correlation between herald and signal photons. For example a $g^{(2)}_{\mathrm{h,s}}$ of 10 means that upon detection of a herald photon, subsequent detection of a correlated signal photon is 9 times more likely than detection of an uncorrelated 'background' photon.

Before proceeding to present the results of the experiment, we spend some time developing a theoretical model for $g^{(2)}_{\mathrm{h,s}}$ which will prove crucial to understanding the data.

6.3 Theoretical model

The model of atom-light interactions developed in section 2.1, which has been sufficient to explain the effects discussed thus far, involved treating all of the optical fields as classical EM fields. The effects of the atoms interacting with the EM vacuum were limited to the dissipation introduced by spontaneous emission. However, in order to describe the effects of SFWM we need to explicitly consider the quantum nature of the interaction of the atoms with the EM field, keeping track of the state of the emitted photons. In this section we develop a theoretical model for heralded single-photon generation by spontaneous four-wave mixing (SFWM) in a thermal atomic vapour. Specifically, we are interested in calculating the joint detection probability $g^{(2)}_{\mathrm{h,s}}$. For comparison, a related analysis is presented in [164] for the case of cold atoms in a lambda system with strong laser dressing.

We consider the dynamics of an ensemble of N four-level atoms, enumerated with j, located at positions $\mathbf{r}_j$ and moving with velocities $\mathbf{v}_j$, that are coupled to electromagnetic (EM) field modes (Fig. 6.3). Two of these modes are the strong pump and coupling laser fields from chapter 5 that will be treated here as classical driving fields, whose driving strengths are given by the Rabi

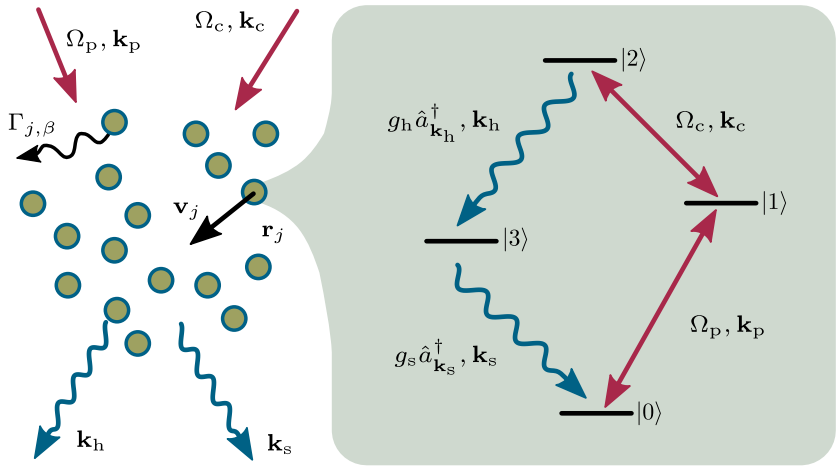

Figure 6.3: A spatially extended medium ($\max[|\mathbf{r}_i - \mathbf{r}_j|] \gg 2\pi/\mathbf{k}_\mathrm{s}$) containing N atoms, enumerated by j, located at positions $\mathbf{r}_j$, and moving with velocities $\mathbf{v}_j$. Internally (inset on the right) the atoms have four levels, and are driven by pump and coupling fields with Rabi frequencies Ω_p and Ω_c. Atoms can spontaneously decay to the herald mode $\mathbf{k}_\mathrm{h}$ and the signal mode $\mathbf{k}_\mathrm{s}$ under the influence of the operators $g_\mathrm{h}\hat{a}^\dagger_{\mathbf{k}_\mathrm{h}}$ and $g_\mathrm{p}\hat{a}^\dagger_{\mathbf{k}_\mathrm{s}}$, or to one of the other modes β with a rate of $\Gamma_{j,\beta}$. The system is analysed in the basis $\bigotimes_j |\alpha_j, \mathbf{r}_j, \mathbf{v}_j\rangle \bigotimes |\hat{n}_{\mathbf{k}_\mathrm{h}}\rangle \bigotimes |\hat{n}_{\mathbf{k}_\mathrm{s}}\rangle$, $\alpha \in \{0, 1, 2, 3\}$, which is coupled to the Markovian reservoir of all other vacuum modes.

frequencies $\Omega_{\rm p}$ and $\Omega_{\rm c}$, and directions by the wavevectors $\mathbf{k}_{\rm p}$ and $\mathbf{k}_{\rm c}$. The dynamics of two specific field modes, named the herald and signal modes, with energies corresponding to the $|2\rangle \rightarrow |3\rangle$ and $|3\rangle \rightarrow |0\rangle$ transitions, are considered separately. Their spatial directions, labelled by the wavevectors $\mathbf{k}_{\rm h}$ and $\mathbf{k}_{\rm s}$ respectively, are defined by the directions of the single-mode inputs of the single-photon detectors used to detect herald and signal photons in the experiment. All of the empty EM field modes, except the herald and signal modes, will be treated with the usual coupling to the Markovian reservoir, giving rise to spontaneous emission from each level α with rates $\Gamma_{j,\alpha}$. The system is analysed in the basis $\bigotimes_j |\alpha_j, \mathbf{r}_j, \mathbf{v}_j\rangle \bigotimes |\hat{n}_{\mathbf{k}_{\rm h}}\rangle \bigotimes |\hat{n}_{\mathbf{k}_{\rm s}}\rangle$, $\alpha \in \{0,1,2,3\}$.

6.3.1 The Hamiltonian

The dynamics of the internal degrees of freedom are modelled using the Hamiltonian $\bar{\mathcal{H}} = \bar{\mathcal{H}}_1 + \bar{\mathcal{H}}_2$ (with $\hbar = 1$), where

$$\begin{aligned}\bar{\mathcal{H}}_1 &= \sum_j \left[\omega_1 |1_j\rangle\langle 1_j| + \omega_2 |2_j\rangle\langle 2_j| + \omega_3 |3_j\rangle\langle 3_j|\right] \\ &\quad + \sum_j \left[\frac{\Omega_{\rm p}}{2}\, {\rm e}^{i\mathbf{k}_{\rm p}\mathbf{r}_j(t) - i\omega_{\rm p}t}\, |1_j\rangle\langle 0_j| + \frac{\Omega_{\rm c}}{2}\, {\rm e}^{i\mathbf{k}_{\rm c}\mathbf{r}_j(t) - i\omega_{\rm c}t}\, |2_j\rangle\langle 1_j| + h.c.\right]\end{aligned}$$

describes the four level system driven, in the rotating wave approximation (RWA), by strong pump and coupling laser fields with respective frequencies ω_p and ω_c, driving the transitions $|0\rangle \leftrightarrow |1\rangle$ and $|1\rangle \leftrightarrow |2\rangle$. The energies of the states $|\alpha\rangle$ are ω_α. Additionally,

$$\bar{\mathcal{H}}_2 = \sum_j \left[g_{\rm h}\, {\rm e}^{-i\mathbf{k}_{\rm h}\mathbf{r}_j(t) + i\omega_{\rm h}t}\, \hat{a}^\dagger_{\mathbf{k}_{\rm h}}\, |3_j\rangle\langle 2_j| + g_{\rm s}\, {\rm e}^{-i\mathbf{k}_{\rm s}{\rm r}_j(t) + i\omega_{\rm s}t}\, \hat{a}^\dagger_{\mathbf{k}_{\rm s}}\, |0_j\rangle\langle 3_j| + h.c.\right]$$

describes the coupling of atom, in the RWA, to the herald and signal detection modes. The coupling strengths between the atom and the vacuum modes, $g_{\rm h}$ and $g_{\rm s}$ for herald and signal channels respectively, formally correspond to $g_{\rm s,h} = \sum_{\mathbf{k}\in\mathbf{k}_{\rm s,h}\pm\Delta\mathbf{k}} g_{23,30}$ where $|\Delta\mathbf{k}| \ll |\mathbf{k}|$ defines the range of emitted photon

directions that hit the detector's sensitive area, and $g_{23,30}$ are the vacuum Rabi coupling frequencies on the herald and signal transitions respectively. The coupling of the atoms to all other EM field modes is described by the Lindblad super-operator

$$L[\hat{\rho}_N] = \sum_{j,\beta}(L_{j,\beta}\hat{\rho}_N L_{j,\beta}^{\dagger} - \frac{1}{2}L_{j,\beta}^{\dagger}L_{j,\beta}\hat{\rho}_N - \frac{1}{2}\hat{\rho}_N L_{j,\beta}^{\dagger}L_{j,\beta}), \tag{6.2}$$

where $\hat{\rho}_N$ is the N-atom density matrix and $L_{j,\beta}$ are the decay channels of atom j, enumerated by β. In our case coupling of the atom to the herald and signal modes, described by $\mathcal{H}_2$, is negligible compared with the coupling to all the other spatial modes. Therefore, the decay of states $|2\rangle$ and $|3\rangle$ is still described, to an excellent approximation, by the usual spontaneous decay rates Γ_2 and Γ_3. Evolution of the external degrees of freedom, due to atomic motion, is accounted for by setting $\mathbf{r}_j(t) = \mathbf{r}_j(0) + \mathbf{v}_j t$.

6.3.2 Rotating frame transformation

Before solving for the dynamics, we transform the equations into a convenient basis by applying the unitary transformation operator

$$\hat{U} = \exp\Bigg(\mathrm{i}\sum_j \{[\omega_\mathrm{p} t - \mathbf{k}_\mathrm{p}\cdot\mathbf{r}_j(t)]|1_j\rangle\langle 1_j| + \omega_3 t|3_j\rangle\langle 3_j| \\ + [(\omega_\mathrm{p}+\omega_\mathrm{c})t - (\mathbf{k}_\mathrm{p}+\mathbf{k}_\mathrm{c})\cdot\mathbf{r}_j(t)]|2_j\rangle\langle 2_j|\}\Bigg),$$

such that a new evolution Hamiltonian $\mathcal{H}_1+\mathcal{H}_2 = \hat{U}^\dagger\bar{\mathcal{H}}\hat{U} - i\hat{U}^\dagger\frac{\mathrm{d}\hat{U}}{\mathrm{d}t}$ is obtained. Thus

$$\mathcal{H}_1 = \sum_j \left[-\Delta_\mathrm{p}|1_j\rangle\langle 1_j| - \delta|2_j\rangle\langle 2_j|\right] + \sum_j \left[\frac{\Omega_p}{2}\ |1_j\rangle\langle 0_j| + \frac{\Omega_c}{2}\ |2_j\rangle\langle 1_j| + h.c.\right], \tag{6.3}$$

$$\begin{aligned}\mathcal{H}_2 = \sum_j \Big\{ & g_\mathrm{h}\ \mathrm{e}^{i(\mathbf{k}_\mathrm{p}+\mathbf{k}_\mathrm{c}-\mathbf{k}_\mathrm{h})\cdot\mathbf{r}_j(t)+i(\omega_\mathrm{h}+\omega_3-\omega_\mathrm{p}-\omega_\mathrm{c})t}\ \hat{a}^\dagger_{\mathbf{k}_\mathrm{h}}\ |3_j\rangle\langle 2_j| \\ & + g_\mathrm{s}\ \mathrm{e}^{-i\mathbf{k}_\mathrm{s}\cdot\mathbf{r}_j(t)+i(\omega_\mathrm{s}-\omega_3)t}\ \hat{a}^\dagger_{\mathbf{k}_\mathrm{s}}\ |0_j\rangle\langle 3_j| + h.c.\Big\},\end{aligned} \tag{6.4}$$

where $\Delta_\mathrm{p} \equiv \omega_p - \mathbf{k}_\mathrm{p}\cdot\mathbf{v}_j - \omega_1$, $\delta \equiv \omega_p + \omega_c - (\mathbf{k}_\mathrm{p}+\mathbf{k}_\mathrm{c})\cdot\mathbf{v}_j - \omega_2$ are the pump and two-photon detunings respectively.

6.3.3 Perturbative dynamics

Since $g_\mathrm{h}\hat{a}^\dagger_{\mathbf{k}_\mathrm{h}}, g_\mathrm{s}\hat{a}^\dagger_{\mathbf{k}_\mathrm{s}} \ll \Omega_\mathrm{p}, \Omega_\mathrm{c}$, we treat the dynamics due to $\mathcal{H}_2$ perturbatively. In the zeroth-order approximation ($\mathcal{H}_2 = 0$), the system density matrix evolves only under driving $\mathcal{H}_1$ and dissipation L (equation 6.2). This evolution is described by the master equation $\frac{\mathrm{d}}{\mathrm{d}t}\hat{\rho}_N = -i[\hat{\rho}_N, \mathcal{H}_1] + L[\hat{\rho}_N] \equiv \mathcal{L}[\hat{\rho}_N]$, which reaches a steady state $\hat{\rho}_N^{(0)}$ under the Liouvillian $\mathcal{L}$. The system evolution under $\mathcal{H}_1$ decomposes to the evolution of individual atoms $\hat{\rho}_N = \bigotimes_j \hat{\rho}_j \bigotimes |0_{\mathbf{k}_\mathrm{h}} 0_{\mathbf{k}_\mathrm{s}}\rangle$, where $\hat{\rho}_j$ is the single atom density matrix for the j-th atom. In particular, atoms with the same velocity $\mathbf{v}$ at different spatial locations will evolve under $\mathcal{H}_1$ to the same single-atom density matrix $\hat{\rho}(\mathbf{v})$. From this it appears that relative atomic positions are irrelevant. However, we shall see that the relative positions of atoms in the ensemble will play a crucial role due to the phase factor in $\mathcal{H}_2$.

In order to obtain the herald-signal joint-detection correlation function $g^{(2)}_{\mathrm{h,s}}(\tau)$ we are interested in calculating $\langle\hat{E}^\dagger_\mathrm{s}(t+\tau)\hat{E}_\mathrm{s}(t+\tau)\hat{E}^\dagger_\mathrm{h}(t)\hat{E}_\mathrm{h}(t)\rangle$. The simplest non-zero contribution to this element originates from the second-order perturbation by $\mathcal{H}_2$. Initially, $\mathcal{H}_2$ perturbatively acts on the steady-state $\hat{\rho}_N^{(0)}$ at some time t, causing the emission of a herald photon. After the first-order

perturbation the new density matrix $\rho_N^{(0)}(t) = \mathcal{H}_2(t)\ \rho_N^{(0)}\ \mathcal{H}_2^\dagger(t)$. Subsequently, the system will evolve under $\mathcal{L}$ before at some time τ later, under the influence of $\mathcal{H}_2(t+\tau)$, a signal photon is emitted:

$$\langle \hat{E}_{\rm s}^\dagger(t+\tau)\hat{E}_{\rm s}(t+\tau)\hat{E}_{\rm h}^\dagger(t)\hat{E}_{\rm h}(t)\rangle = {\rm Tr}\left[\hat{E}_{\rm s}^\dagger(t+\tau)\hat{E}_{\rm s}(t+\tau)\hat{E}_{\rm h}^\dagger(t)\hat{E}_{\rm h}(t)\ \hat{\rho}_N^{(2)}\right], \tag{6.5}$$

$$\hat{\rho}_N^{(2)} = \mathcal{H}_2(t+\tau)\ {\rm e}^{-i\mathcal{L}\tau}\rho_N^{(1)}(t)\ \mathcal{H}_2^\dagger(t+\tau),$$

where the trace is over all the atomic degrees of freedom and the herald and signal field modes.

6.3.4 Herald photon emission

Analysing the time dependence of the atom coupling to the herald mode, i.e. the terms containing $\hat{a}_{\mathbf{k}_{\rm h}}$ in $\mathcal{H}_2$ [Eq.(6.4)], we see that for atoms with a velocity $\mathbf{v}$ the dominant decay is to a mode with frequency $\omega_{\rm h} = \omega_{\rm p} + \omega_{\rm c} - \omega_3 - (\mathbf{k}_{\rm p} + \mathbf{k}_{\rm c} - \mathbf{k}_{\rm h})\cdot\mathbf{v}_j$. Starting from the steady state density matrix $\hat{\rho}_N^{(0)}$, the emission of a photon in the herald mode acts on the states as

$$\hat{\rho}_N^{(1)}(t) \equiv \mathcal{H}_2(t)\hat{\rho}_N^{(0)}\mathcal{H}_2^\dagger(t) \propto \sum_i c_i \left[\sum_{j_1} c'_{j_1}\ g_{\rm h}\ {\rm e}^{i(\mathbf{k}_{\rm p}+\mathbf{k}_{\rm c}-\mathbf{k}_{\rm h})\cdot\mathbf{r}_{j_1}(t)}|\ldots 3_{j_1}\ldots 1_{\mathbf{k}_{\rm h}}\rangle\right] \times \left[\sum_{j_2} c'_{j_2}\ g_{\rm h}\ {\rm e}^{-i(\mathbf{k}_{\rm p}+\mathbf{k}_{\rm c}-\mathbf{k}_{\rm h})\cdot\mathbf{r}_{j_2}(t)}\langle\ldots 3_{j_2}\ldots 1_{\mathbf{k}_{\rm h}}|\right].$$

We see that emission, and subsequent detection of the herald photon, projects the system into a state where *a single excitation is stored collectively as a coherent spin-wave* with a periodic phase variation given by the wavevector $\mathbf{k}_{\rm p}+\mathbf{k}_{\rm c}-\mathbf{k}_{\rm h}$. The broadband detection scheme does not discern the frequency of the herald photon $\omega_{\rm h}$, since $\hat{E}_{\rm h} = \sum_{\omega_{\rm h}} \hat{a}_{\mathbf{k}_{\rm h}}$ where the sum over $\omega_{\rm h}$ encompasses the full Doppler broadened emission profile from the vapour. Therefore the system will be projected in a state where *the excitation is stored in all atomic velocity classes.*

6.3.5 Signal photon emission

Subsequently, for a time τ the atoms move to new locations $\mathbf{r}_j(t+\tau) = \mathbf{r}_j(t) + \mathbf{v}_j\tau$. During this time the internal state of the system changes only due to the atoms in state $|3\rangle$, since all other atoms are already in a stationary state of $\mathcal{L}$. This state is decoupled from $\mathcal{H}_1$ [Eq. (6.3)], but evolves due to spontaneous decay and dephasing collisions under L (equation 6.2), resulting in an amplitude reduction of $\exp(-\gamma\tau)$. Upon signal photon emission, the system will be left in the state

$$\begin{aligned}
\hat{\rho}_N^{(2)}(t+\tau) &\equiv \mathcal{H}_2(t+\tau)\ \hat{\rho}_N^{(1)}(t+\tau)\ \mathcal{H}_2^\dagger(t+\tau) \\
&\propto \exp(-2\gamma\tau) \\
&\quad\times \left\{ \sum_{j_1} e^{-i(\mathbf{k}_\mathrm{h}+\mathbf{k}_\mathrm{s}-\mathbf{k}_\mathrm{p}-\mathbf{k}_\mathrm{c})\cdot\mathbf{r}_{j_1}(t)+i(\omega_\mathrm{s}-\mathbf{k}_\mathrm{s}\cdot\mathbf{v}_{j_1}-\omega_3)\tau}\ |\ldots 0_{j_1}\ldots 1_{\mathbf{k}_\mathrm{h}} 1_{\mathbf{k}_\mathrm{s}}\rangle \right\} \\
&\quad\times \left\{ \sum_{j_2} e^{i(\mathbf{k}_\mathrm{h}+\mathbf{k}_\mathrm{s}-\mathbf{k}_\mathrm{p}-\mathbf{k}_\mathrm{c})\cdot\mathbf{r}_{j_2}(t)-i(\omega_\mathrm{s}-\mathbf{k}_\mathrm{s}\cdot\mathbf{v}_{j_2}-\omega_3)\tau}\ \langle\ldots 0_{j_2}\ldots 1_{\mathbf{k}_\mathrm{h}} 1_{\mathbf{k}_\mathrm{s}}| \right\} \\
&\quad + \ldots,
\end{aligned}$$

where we have explicitly omitted terms that do not contribute to the correlated emission of photons in the herald and signal channels. In order for this event to have a significant probability of occurring at any time $t+\tau$, the emitted signal photon must comprise frequencies centred on $\omega_\mathrm{s} = \omega_3 + \mathbf{k}_\mathrm{s}\cdot\mathbf{v}_j$, i.e. the moving atom must emit the photon within the linewidth of the signal-transition. In other words, velocity classes differing by $\delta\mathbf{v}$ will emit photons with frequencies differing by $\mathbf{k}_\mathrm{s}\cdot\delta\mathbf{v}$, with *well defined initial relative phases and amplitudes* set by the emission of an initial herald photon. Crucially, since the signal detector does not discern the close energies of the emitted photons, in calculating the amplitude for the detection event $\hat{E}_\mathrm{s} = \sum_{\omega_\mathrm{s}} \hat{a}_{\mathbf{k}_\mathrm{s}}$ we must sum over the range of ω_s corresponding to the detector bandwidth, and in this way we *do not measure which velocity class emitted the photon.*

The amplitudes of photon emission from different atoms will interfere, leading to directional emission, provided that the photons *do not leave any*

information in the medium about which atom stored the excitation. States that fulfil this condition have atoms j_1 and j_2 in a coherent superposition where one is excited to $|2\rangle$ and the other is in the ground state $|0\rangle$, i.e. $|\ldots 0_{j_1} \ldots 2_{j_2} \ldots\rangle$ and $|\ldots 2_{j_1} \ldots 0_{j_2} \ldots\rangle$. Since after two-photon decay both of these states end up with both of the atoms in the ground state $|\ldots 0_{j_1} \ldots 0_{j_2} \ldots\rangle$, there is no information left in the medium conveying which of the two atoms decayed. This leads to interference of the decay amplitudes (to the ground-state), obtained as a sum of decays from different atoms. Therefore, in calculating [Eq. (6.5)] the dominant non-zero elements[1] will originate from $\langle \ldots 0_{j_1} \ldots 2_{j_2} \ldots | \hat{\rho}_N^{(0)} | \ldots 2_{j_1} \ldots 0_{j_2} \ldots\rangle$ and the corresponding conjugate. Given that the dynamics under $\mathcal{L}$ decompose into the single-atom dynamics, the contributing matrix elements traced over all atoms other than j_1, j_2 are equal to $\hat{\rho}_{02}(\mathbf{v}_{j_1})\ \hat{\rho}_{20}(\mathbf{v}_{j_2})$, where $\hat{\rho}(\mathbf{v})$ is the steady-state single-atom density matrix. Therefore the initial relative phases and amplitudes of photon emission from different velocity classes in state $|3\rangle$ are inherited, by the herald emission process, from $\hat{\rho}_{20}$. Equation 3.1 in chapter 3 can be used to calculate the steady-state value of ρ_{20}.

6.3.6 Joint detection probability

Overall, the joint detection probability [Eq. (6.5)] can be written as

$$\langle \hat{E}_{\mathrm{s}}^{\dagger}(t+\tau)\hat{E}_{\mathrm{s}}(t+\tau)\hat{E}_{\mathrm{h}}^{\dagger}(t)\hat{E}_{\mathrm{h}}(t)\rangle \propto$$

$$\left| \sum_j g_{\mathrm{h}} g_{\mathrm{s}}\ \hat{\rho}_{20}(\mathbf{v}_j)\ \exp(-\gamma\tau)\ \exp(-i\mathbf{k}_{\mathrm{s}} \cdot \mathbf{v}_j \tau)\ \exp[i(\mathbf{k}_{\mathrm{p}} + \mathbf{k}_{\mathrm{c}} - \mathbf{k}_{\mathrm{h}} - \mathbf{k}_{\mathrm{s}}) \cdot \mathbf{r}_j(t)] \right|^2 .$$

In order to obtain non-zero values, summation over random atomic positions $\mathbf{r}_j$ must produce a constant value, which gives rise to the condition $\mathbf{k}_{\mathrm{p}} + \mathbf{k}_{\mathrm{c}} - \mathbf{k}_{\mathrm{h}} - \mathbf{k}_{\mathrm{s}} = 0$ which is the usual *phase matching condition* for wave-mixing processes in extended media. When this condition is fulfilled, the remaining

[1] Terms proportional to ρ_{22} do not interfere, so emission is not significantly enhanced in the signal direction. They are therefore much smaller than the interfering terms and can be neglected.

time dependence can be written as an integral over all velocity classes

$$\langle \hat{E}_{\mathrm{s}}^{\dagger}(t+\tau)\hat{E}_{\mathrm{s}}(t+\tau)\hat{E}_{\mathrm{h}}^{\dagger}(t)\hat{E}_{\mathrm{h}}(t)\rangle \propto \left| \underbrace{\int_{\mathbf{v}} \mathrm{d}\mathbf{v}\ p(\mathbf{v})\ \rho_{20}(\mathbf{v}) \exp(-\gamma\tau)\ \exp(-i\mathbf{k}_{\mathrm{s}}\mathbf{v}\tau)}_{\equiv\Psi} \right|^2 , \tag{6.6}$$

where $p(\mathbf{v})$ is the probability density function that an atom has velocity $\mathbf{v}$. We note that this calculation only includes the contribution from correlated decays. There is also a constant background of uncorrelated decays produced by other events. For example, following herald emission in channels other than $\mathbf{k}_{\mathrm{h}}$ there is no clear phase matching condition for the signal emission, which can then still end up in $\mathbf{k}_{\mathrm{s}}$. Furthermore, in collisional processes population can be transferred non-radiatively from $|1\rangle$ to $|3\rangle$, causing additional background emission. Due to this the normalised signal for detection, with low heralding efficiency, will have the form

$$\frac{\langle \hat{E}_{\mathrm{s}}^{\dagger}(t+\tau)\hat{E}_{\mathrm{s}}(t+\tau)\hat{E}_{\mathrm{h}}^{\dagger}(t)\hat{E}_{\mathrm{h}}(t)\rangle}{\langle \hat{E}_{\mathrm{s}}^{\dagger}\hat{E}_{\mathrm{s}}\rangle\langle \hat{E}_{\mathrm{h}}^{\dagger}\hat{E}_{\mathrm{h}}\rangle} = 1 + c\langle\Psi|\Psi\rangle,$$

where c is a constant dependent on the background level.

6.3.7 Discussion

In order to gain some insight into the results of this model we can consider three limiting cases. In all three cases we assume that the velocity distribution $p(v)$ is Gaussian and that $k_{\mathrm{s}}p(v)$ is much wider than the linewidth of the coherence on the signal transition γ. A sketch of the limiting cases ((1) – (3)) is shown in figure 6.4.

(1) Firstly, in the case that the distribution of the excitation $\rho_{20}(v)$ is uniform (independent of velocity), the joint detection probability is a Gaussian decay with a width inversely proportional to the width of the velocity distribution. This limit makes clear the origin of motional dephasing in thermal vapours.

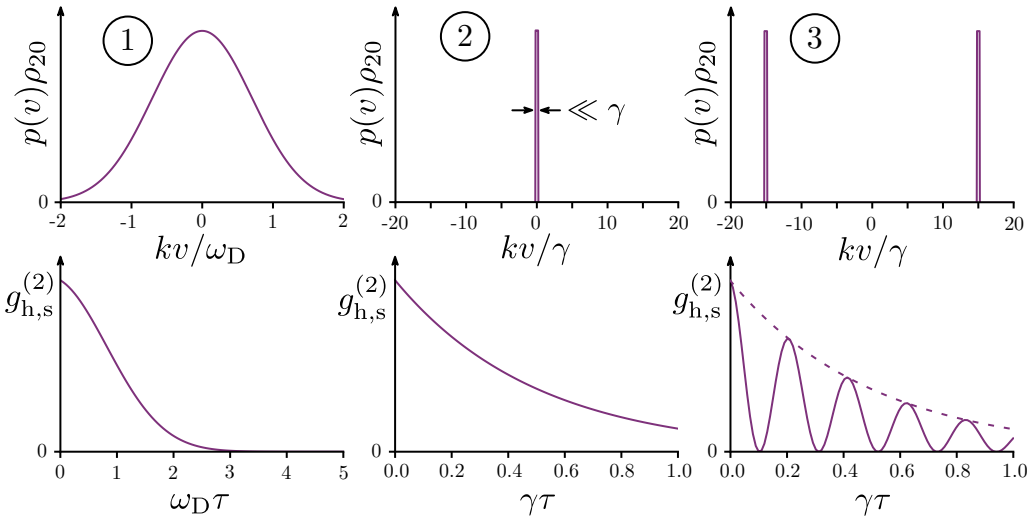

Figure 6.4: Illustration of three limiting cases of the theoretical model for the joint detection probability $g^{(2)}_{\mathrm{h,s}}$. The distribution of the excitation amongst the atomic velocity classes is shown on top and the corresponding $g^{(2)}_{\mathrm{h,s}}(\tau)$ is shown below. (1) A Gaussian distribution of excitation with a width determined by the Doppler-width results in a Gaussian decay with a lifetime inversely proportional to the Doppler-width. (2) A distribution of excitation much narrower than the natural linewidth γ results in an exponential decay over the natural lifetime $1/\gamma$. (3) Interference of the emission from two narrow groups of atoms results in oscillations with a frequency proportional to their difference in velocity with an amplitude decaying over the natural lifetime.

(2) Secondly, in the case that the distribution of the excitation $k_s\rho_{20}(v)$ is much narrower than γ, the joint detection probability is simply an exponential decay with a lifetime determined by the coherence lifetime $1/\gamma$. We note here that the same result is obtained in the case that $k_s p(\mathbf{v})$ is much narrower that γ, which is the usual situation in cold atom experiments [23].

(3) A final limiting case is that the distribution of the excitation $k_s\rho_{20}(v)$ is composed of two groups of atoms, each with a width much narrower than γ. In this case, there is interference between the light emitted by each group of atoms, resulting in beats in the detection probability, with a frequency proportional to the difference in velocity. Since the widths of the two velocity groups are much narrower than γ the overall decay is still determined by γ.

These situations are good approximations in several regimes of the experimental parameters, and will therefore assist in our interpretations of the results.

6.4 Results

6.4.1 Resonant driving with strong dressing

We first consider the situation of resonant pump and coupling fields, with powers of 10 μW and 34 mW respectively. The cell temperature, measured using a thermocouple, is 80°C. The experimentally measured normalised cross-correlation is displayed in figure 6.5(a) (blue circles). In contrast with the three special cases that we previously discussed (figure 6.4), the correlation does not display a maximum at $\tau = 0$. The difference here is that the excitation distribution $p(v_z)\rho_{20}(v_z)$ is complex valued with a velocity dependent argument (phase). The theoretically calculated magnitude and phase distributions of $\Psi(v_z)$ (equation 6.6) are shown in figure 6.5(b) for different delays. The blue lines show the distributions immediately after heralding ($\tau = 0$). The form of

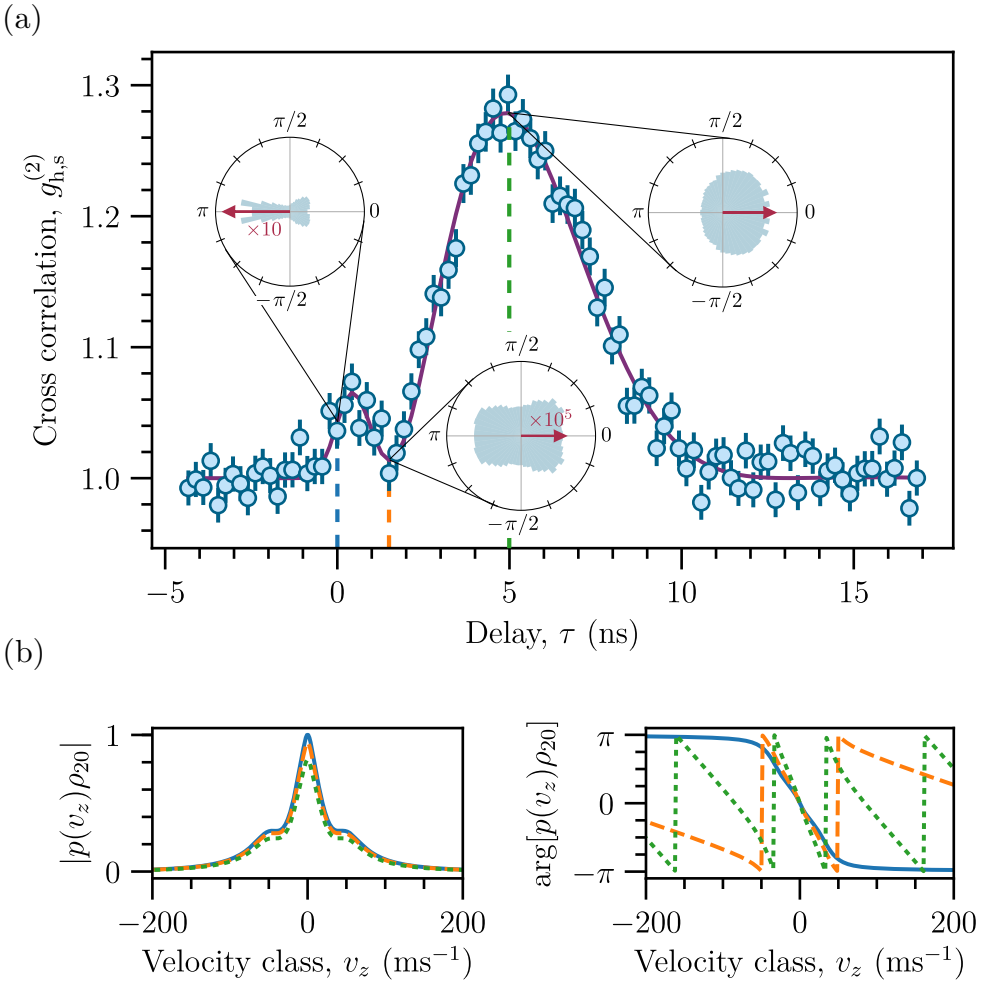

Figure 6.5: Interference gives rise to structure in the joint detection probability. (a) The measured cross correlation for resonant driving fields is shown (blue circles) for time delays (τ) between herald and signal photon detection. A fit to the theoretical model developed in the text is also shown (solid purple line). (b) The theoretical amplitude and phase distributions (resulting from the fit parameters) of the two-photon coherence amongst the atomic velocity classes are plotted for several delays: $\tau = 0$ (solid blue lines), $\tau = 1.5$ ns (dashed orange lines) and $\tau = 5$ ns (dotted green lines). In (a), amplitude-weighted histograms of the theoretical phase distributions are plotted for the same three delays as indicated by the blue, orange and green vertical dashed lines.

the magnitude distribution is quite complicated due to the strong dressing by the pump and coupling fields, with peak Rabi frequencies of 35 MHz and 280 MHz respectively. In the calculation of $\Psi(v_z)$ we sum over the measured Gaussian intensity profiles of the pump and coupling fields. The variation of the Rabi frequencies leads to broadening of the lines and a resultant lineshape that is quite complicated. However, we can highlight some simple features in order to make sense of the resulting correlation.

Firstly, all of the dynamics occurs within a time window of ∼10 ns, during which time the magnitude of the excitation is only marginally decreased by spontaneous decay. This can be seen by the dashed orange and dotted green lines in figure 6.5(b) which correspond to time delays of $\tau = 1.5$ ns and $\tau = 5$ ns respectively. Therefore the observed dynamics are predominantly determined by the atomic motion resulting in Doppler-shifted emission which is described by the $\exp(-\mathrm{i}k_\mathrm{s}v_z\tau)$ term in equation 6.6. This term gives rise to the phase wrapping observed in the phase distribution [figure 6.5(b)]. A more intuitive way to display the same information, is to histogram the theoretically calculated phases of different velocity classes, weighted by their magnitudes. Three of these histograms are displayed as polar plots in panel (a) for the delays $\tau = 0, 1.5, 5$ ns, with red arrows indicating the (scaled) $g^{(2)}_{\mathrm{h,s}}$. For $\tau = 0$, the phase rapidly changes by 2π through resonance ($v_z = 0$) resulting in a significant amount of destructive interference and a low correlation. Even though the magnitude is significantly smaller for fast velocity classes, the phase varies slowly around π and there is therefore constructive interference between these atoms. The phases associated with the fast-moving atoms evolve rapidly to the point, at $\tau = 1.5$ ns, where the interference with the slow moving atoms is almost perfectly destructive (the red arrow has been scaled by 10^5 in order to be visible). Subsequent evolution decreases this destructive interference to the point, at $\tau = 5$ ns, where the maximum correlation is reached. A measure of the amount of interference is given by $|\langle\Psi(v_z)\rangle_{v_z}|/\langle|\Psi(v_z)|\rangle_{v_z}$, where the angled bracket notation refers to the integration over v_z. Values of 1 and 0 correspond to complete constructive and destructive interference respectively. Even at $\tau = 5$ ns, when there is the maximum correlation,

$|\langle\Psi(v_z)\rangle_{v_z}|/\langle|\Psi(v_z)|\rangle_{v_z} \approx 0.2$ showing that the correlation is significantly hampered by this destructive interference. Any method to post-select herald photons with a particular frequency, corresponding to a particular velocity class, would result in a significantly increased correlation, albeit at the cost of a decreased rate of single photons.

The overall detection rate of correlated photon pairs can be calculated by summing the raw cross-correlation histogram and subtracting the number of uncorrelated counts: Pair rate $= \sum_{\tau=t_0}^{t_1} G^{(2)}_{\mathrm{h,s}}(\tau) - r_{\mathrm{h}} r_{\mathrm{s}}(t_1 - t_0)T$, where t_0 and t_1 should in principle be $-\infty$ and ∞ but in practice it is sufficient to choose cut-offs at -5 ns and 20 ns. With this we calculate a pair rate of 87 Hz which is compared to the individual herald and signal detector count rates of 127 kHz and 470 kHz respectively. The rate of correlated photon pairs is more than one thousand times smaller than the rate of uncorrelated photons. The heralding efficiency (uncorrected for losses in the detection), which is the probability of detecting a signal photon, conditional on the detection of a herald, is therefore very low ($< 0.1\%$) compared to the best SPDC sources (83% uncorrected for losses [165]).

The origin of the large background is not yet fully understood, however we can give some suggestions as to its origin. Firstly, any steady-state population in the excited state $|2\rangle$ may decay to state $|3\rangle$ emitting herald photons in any-direction since there is no well-defined phase-relation on this transition. The herald photon emission angles that give rise to phase-matched emission of signal photons are displayed in figure 6.1(b). If herald photons that are emitted in other directions are detected (due to having a large optical fibre detection mode), there will be no correlated detection of a signal photon. Additionally, the efficiency of the detection system plays a crucial role since signal photons can be lost en-route to the detector. The quantum efficiency of the detectors is approximately 60% at 780 nm and we estimate the optical fibre collection efficiency to be on the order of 50%. Additionally, the optical fibres used for collection have a built-in 50-50 beam splitter which results in another $\sim$50% loss. The losses in the narrowband interference filters are less than 5% for each filter (typically 3 filters are used) and the total loss

due to reflection at the vapour cell surfaces is measured to be ∼8%. Thus the total efficiency of the detection system for each of the herald and signal modes is estimated to be in the range of 10%. Finally, signal photons emitted by atoms with different velocities have different relative phases (figure 6.5). Destructive interference in the emission from different atoms therefore leads to non-phase matched emission. At high temperatures, the medium becomes optically thick to the signal photons, resulting in a significantly decreased heralding efficiency as we will see in the following section.

6.4.2 Dependence on temperature

We now consider the effect of varying the atomic number density via the cell temperature, across a range of 55-142°C. The experimentally measured count-rates on the herald and signal detectors are displayed in figure 6.6(a). The blue circles show the count-rates on the herald detector (762 nm). The measured count-rates on the signal detector are the sum of the orange and empty green circles, where the empty green circles are the count-rates with the coupling beam switched off. The lines are fits to a simple theoretical model which is developed as follows.

For a weak pump laser, ρ_{20} and ρ_{22} are proportional to the pump electric field and intensity respectively. Upon propagation by distance z through the medium of length L, the pump intensity decreases exponentially following the Beer-Lambert law. Furthermore, the emitted photons can be re-scattered by the remaining length of medium. In order to calculate the total rate of emitted photons we should integrate ρ over the whole length of the medium. In this case the total count-rates for uncorrelated emission are expected to follow

$$\text{Countrate} = AN \int_0^L \exp(-BNz)\ \exp[-CN(L-z)]\ \mathrm{d}z \tag{6.7}$$

$$= \frac{A}{B-C}[\exp(-CNL) - \exp(-BNL)], \tag{6.8}$$

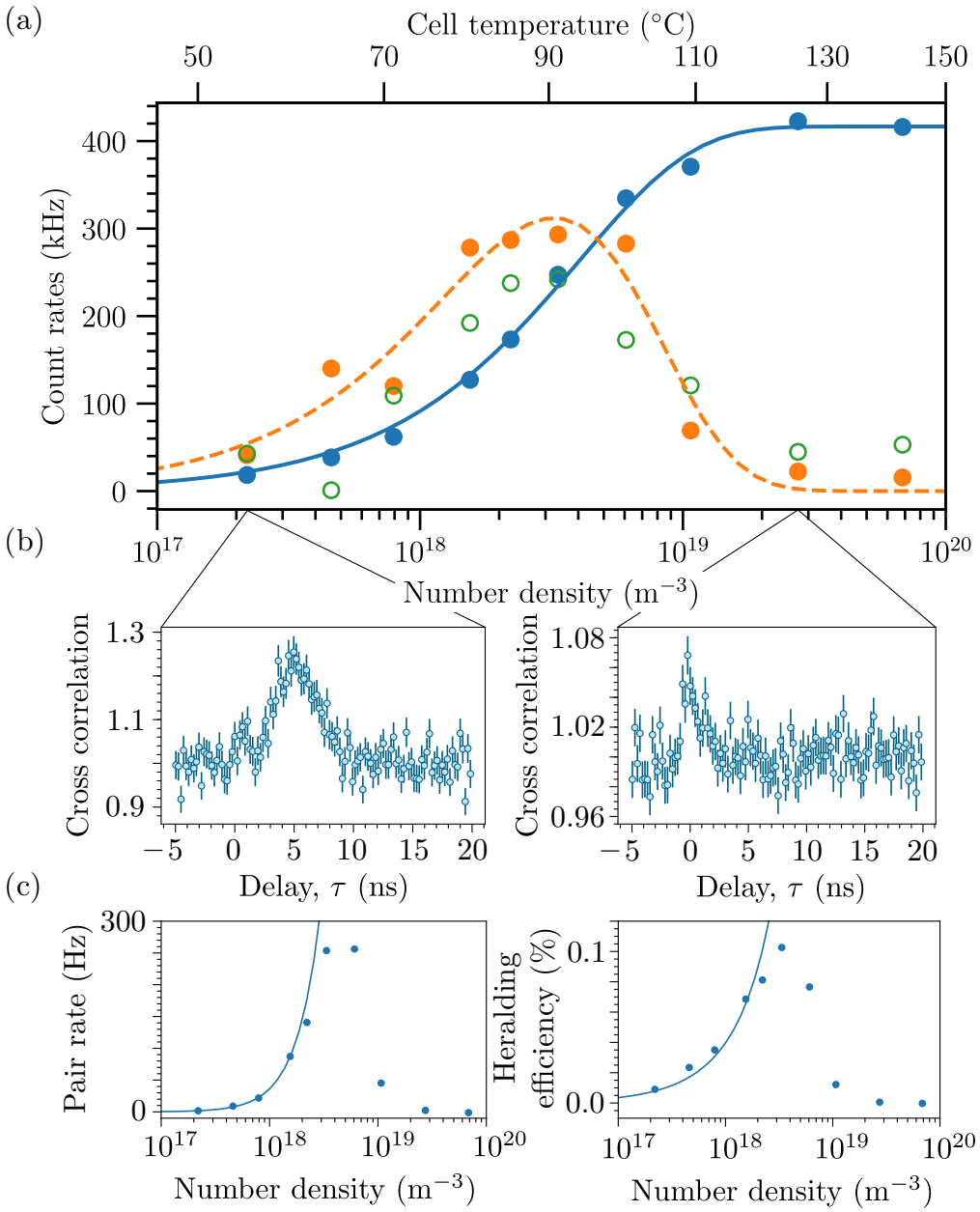

Figure 6.6: Temperature dependence of heralded single-photon generation with resonant driving fields. (a) The individual count rates of herald and signal photons are shown by the blue and orange circles respectively. The empty green circles show the background count rate of signal photons when the coupling laser is switched off. (b) The cross correlations measured at cell temperatures of 55°C and 125°C. (c) The measured rate of photon pairs and the heralding efficiency. The lines in (a) and (c) are fits to a simple model described in the text.

where A is an overall scaling parameter, BN is the absorption coefficient for the pump field and CN is the absorption coefficient for the emitted photons. For the herald photons, CN is assumed to be zero since the steady-state population of state $|3\rangle$ is negligible. This simple model finds good agreement with the data from the herald detector for constants $A = 420$ kHz and $B = 2.5 \times 10^{-19}$ m^3 [blue line in figure 6.6(a)], despite the fact that the pump is well above the saturation intensity of the $5P_{3/2} \rightarrow 5P_{3/2}$ transition. The large difference in the value of A between the herald and signal detectors appears due to the poor collection efficiency of the herald detection system.

The large remaining background of uncorrelated signal photons present when the coupling laser is switched off is a surprising result. One explanation is that this appears due to collisional population transfer between one $5P_{3/2}$ excited atom and one ground-state atom [166] (known as fine structure changing collisions) or between two excited $5P_{3/2}$ atoms [167] (known as energy pooling). The subject of energy transfer in dense thermal vapours is a substantial research area in itself and this uncorrelated background light may have a significant limiting effect on the levels of correlation attainable in this type of system. For these reasons, investigations into the origin of this energy transfer are currently ongoing. In the context of this thesis, we will only concern ourselves with the dynamics of the heralded single photons produced in this experiment, which are unaffected by the background photons.

At high densities the re-scattering of the signal photons has a significant effect on the time dependence of the correlation [figure 6.6(b)]. At low densities the peak $g^{(2)}_{\mathrm{h,s}}$ occurs at approximately $\tau = 5$ ns. At high densities, the large optical density (OD) on-resonance means that the emission from the slow velocity-classes is re-scattered, leaving mainly the off-resonant emission, due to fast velocity-classes, to be detected. As we discussed in the previous section, these atoms are initially in-phase but due to the large spread in velocities, they rapidly dephase resulting in the observed short coherence time.

The experimentally measured pair-rates are plotted as blue circles in figure 6.6(c) along with a simple model (solid line) which is described by

Pair rate $= CN^2$, where C is an overall scaling parameter. The model has been fitted to the first four data points. In the low density regime the number of herald photons scales linearly with N. Emission and detection of *each* herald photon projects the atoms into a collective superposition state and the directionality of the photons emitted from this state scales linearly with the number of atoms. In total this gives rise to the N^2 dependence that is observed in the data.

6.4.3 Dependence on coupling detuning

We have already seen that the time dependence of the correlation between herald and signal photons is dictated by the distribution of the two-photon coherence ρ_{20} amongst the atomic velocity classes. With resonant pump and coupling fields, the strong dressing of the coupling laser (with a peak Rabi frequency of $\Omega_c \approx 270$ MHz) results in the symmetric Autler-Townes splitting of the two-photon absorption line. Detuning the coupling laser increases the splitting (and introduces an asymmetry) to the dressed states. This is reflected in the distribution of the excitation amongst the velocity classes as a function of coupling detuning, as is shown in figure 6.7. The strong dressing by the coupling laser leads to the excitation of two narrow velocity-groups (with well defined relative phases) satisfying the condition $2kv_z \approx \frac{1}{2}(\Delta_c \pm \sqrt{\Delta_c^2 + 2\Omega_c^2})$ (equation 3.5 defining $k \equiv k_p \approx k_c$). The emission of a herald photon coherently splits a single excitation into a superposition of these two velocity groups and, subsequently, the emitted signal fields interfere due to their Doppler shifted frequencies. This interference results in the appearance of beats in the measured cross-correlations (figure 6.8).

In this experiment the pump power was set to 4 μW and the coupling power was 40 mW. The data clearly displays an increase in oscillation frequency with detuning, as expected due to the increased difference in velocity between the two excited groups of atoms. The intermediate detunings correspond to case (3) in figure 6.4 while for larger detunings the fast atoms are predominantly excited, leading to less visible beats and a simpler exponential decay

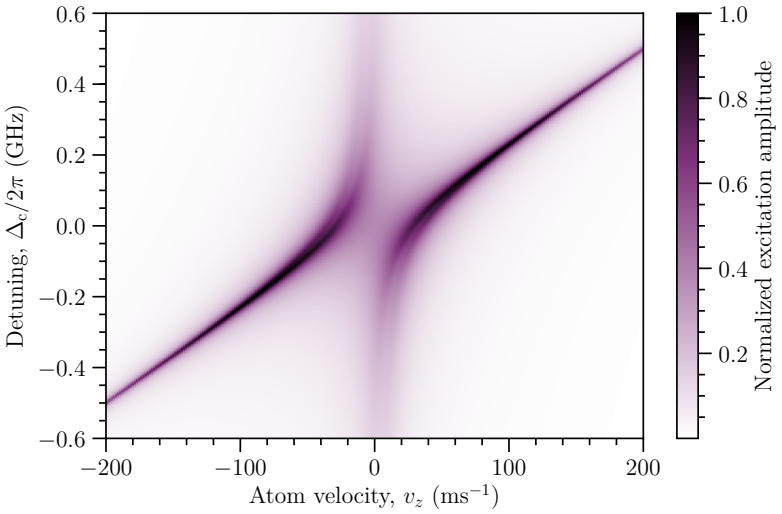

Figure 6.7: Theoretical magnitude distribution of two-photon coherence $|\rho_{20}|$ amongst the atomic velocity classes as a function of the coupling beam detuning Δ_c.

corresponding to the narrow Lorentzian excitation distribution amongst these atoms: case (2) in figure 6.4. The solid lines are fits to the experimental data using chi-squared minimization [81] with common fit parameters for all data-sets displayed. Overall we find excellent agreement between the developed theoretical model and the experimental temporal correlation data.

6.4.4 Dependence on pump detuning

Setting the coupling laser on resonance, we observe that detuning the pump laser has a dramatic effect on the magnitude and shape of the observed photon correlations [figure 6.9(a-c)]. At a detuning of −560 MHz we observe the appearance of oscillations in the cross-correlation similar to those in figure 6.8. As before these result from the splitting of the dressed $5P_{3/2}$ and $5D_{3/2}$ states and the beat frequency increases with detuning in the same fashion. At much larger detunings, the oscillatory component of the correlation vanishes and we are left with a narrow peak at $\tau = 0$ which has a maximum correlation that increases rapidly with detuning. The reason for the sharp increase in

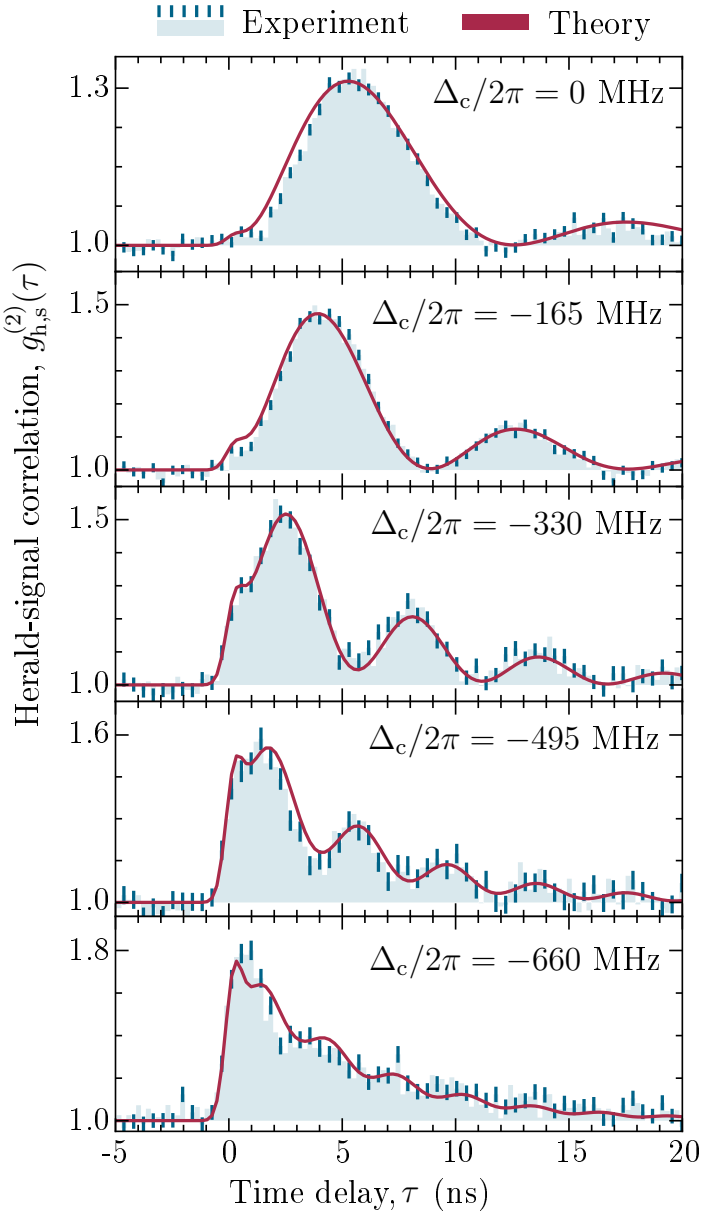

Figure 6.8: Experimental data (blue) showing interference resulting from coherent splitting of a single excitation across two groups of atoms with relative motion. The Doppler shift leads to beats in the state readout with a frequency proportional to the relative velocity. The detuning of a strong dressing laser, Δ_c, sets the velocities of the excited atoms and thereby determines the beat frequency. A theoretical model (red) finds excellent agreement with the data across the entire range of detunings studied. The error bars on the experimental data are calculated assuming Poissonian noise on the individual histogram bins [81].

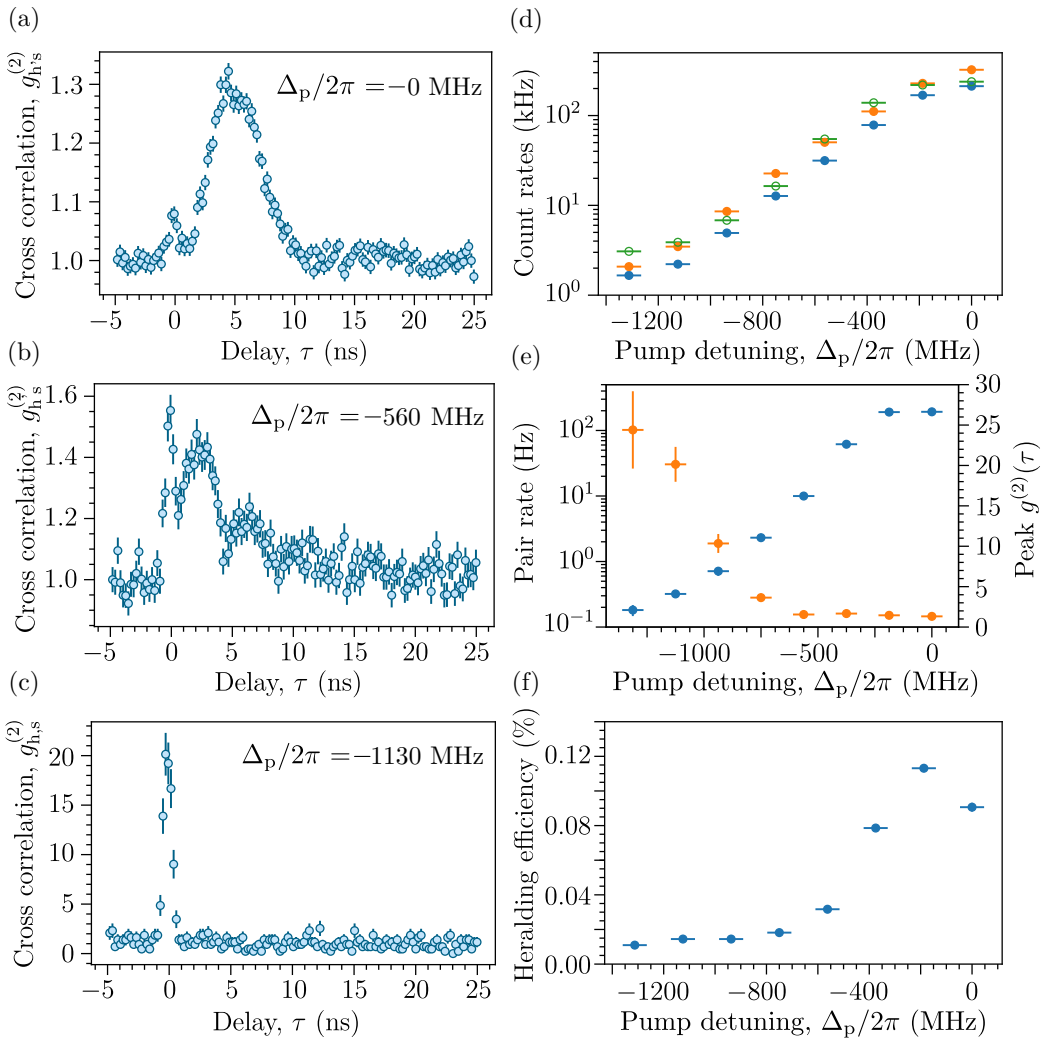

Figure 6.9: The effect of detuning the pump field (with a resonant coupling field) on photon pair generation. (a-c) Measured cross-correlations for three pump detunings (the detunings are shown on the plots). (d) Count rates on the herald (blue) and signal (orange) detectors as a function of pump detuning. The signal count rates have had the background (green) subtracted, which was measured in each case with the coupling beam off. (e) Pair rates (blue) and the peak value of $g^{(2)}_{\mathrm{h,s}}(\tau)$ (orange). (f) Heralding efficiency.

correlation is postulated to be as follows. In the case that the pump detuning exceeds the Doppler width, only a small number of atoms are directly two-photon resonant with the pump and coupling lasers, the majority fall within the long tail ($1/\Delta_{\mathrm{p}}^2$) of the Lorentzian line-shape of ρ_{20}. When the detuning is sufficiently large (typically two Doppler-widths or more for alkali metal vapours [168]), the total coherence due to the off resonant interactions is stronger than that due to resonant interactions (the excitation distribution is near Gaussian as in case (1) of figure 6.4). This has two effects: Firstly, far from resonance the phase of the coherence is independent of detuning (velocity) and the emitted fields add constructively. Secondly, the coherence ρ_{20} decreases more slowly with detuning than the population ρ_{22}. Given that the major source of background photons in our experiment appears from the population ρ_{22}, the correlation increases with detuning.

Clearly, as the detuning is increased the overall rates of single and pairs will decrease and there is a trade-off between having a strong correlation and a high pair rate. This can be clearly seen in figure 6.9(e) where we see that while the on-resonance pair rate is ∼200 Hz, the off-resonance pair rate (to obtain a $g_{\mathrm{h,s}}^{(2)} > 20$) is less than 1 Hz. The cross-correlations that we have observed for a detuned pump field are expected to be in violation of the Cauchy-Schwarz inequality. We therefore devote the next section to an explanation and measurement of this inequality.

6.4.5 Cauchy-Schwarz violation

The Cauchy-Schwarz inequality is a measure of the non-classicality of a light source. For a light source that contains only classical intensity correlations, the square of the cross-correlation is bounded by the product of the auto-correlations for each of the two modes [54] (herald and signal):

$$R = \frac{[g_{\mathrm{h,s}}^{(2)}(\tau)]^2}{g_{\mathrm{h}}^{(2)}(0) g_{\mathrm{s}}^{(2)}(0)} \leq 1. \tag{6.9}$$

The measured cross- and auto-correlation functions for pump detunings of $\Delta_p/2\pi = -750 \pm 50$ MHz and $\Delta_p/2\pi = -1130 \pm 50$ MHz are displayed in figure 6.10. Note that owing to only having two photon detectors, we measured each of the correlation functions during independent experimental runs. The total data-aquisition time of the runs varied between 10^3 and 10^4 seconds. The unheralded light in each of the herald and signal modes is expected to display bunching, as is typical of thermal chaotic light sources [54]. The photon bunching is be observed as a peak at $\tau = 0$ in the auto-correlation measurement. For a thermal chaotic light source the expected auto-correlation functions are Gaussian, with a width that is inversely proportional to the velocity-distribution of the emitters [54]. In our case, this Gaussian should be further broadened by timing jitter in the photon detection. With the exception of the signal channel for -750 MHz pump detuning [figure 6.10 panel (e)], the auto-correlation functions are not well-resolved due to the relatively low count rates. In the one well-resolved case we fit a Gaussian function $g_s^{(2)}(\tau) = 1 + A\exp(-x^2/w^2)$ to the data which results in good agreement with parameters $A = 0.39$ and $w = 0.92$ ns. The narrow $g^{(2)}$ is indicative of the broad distribution of excitation that is produced via off-resonant excitation [168].

Using $\tau = 0$ we obtain $R = 5.7 \pm 0.7$ and $R = (6 \pm 3) \times 10$ at the pump detunings of 750 and 1130 MHz respectively. While the value of R is larger in the case of the more detuned pump, the significantly smaller pair-rate means that accumulating the statistics takes substantially longer. We therefore observe a much stronger violation in the less detuned case: 6.7 standard deviations.

At this point it is pertinent to note that in principle we have only shown a strong (and non-classical) correlation between two different optical fields, by using the twin-beam Cauchy-Schwarz inequality [54]. However, we have not shown that upon a heralding detection, the signal field is a single-photon state (or that it is non-classical). To do so requires measurement of the single-mode Cauchy-Schwarz inequality for the signal mode upon each heralding event. We have attempted to make such a measurement, however, the single-photon

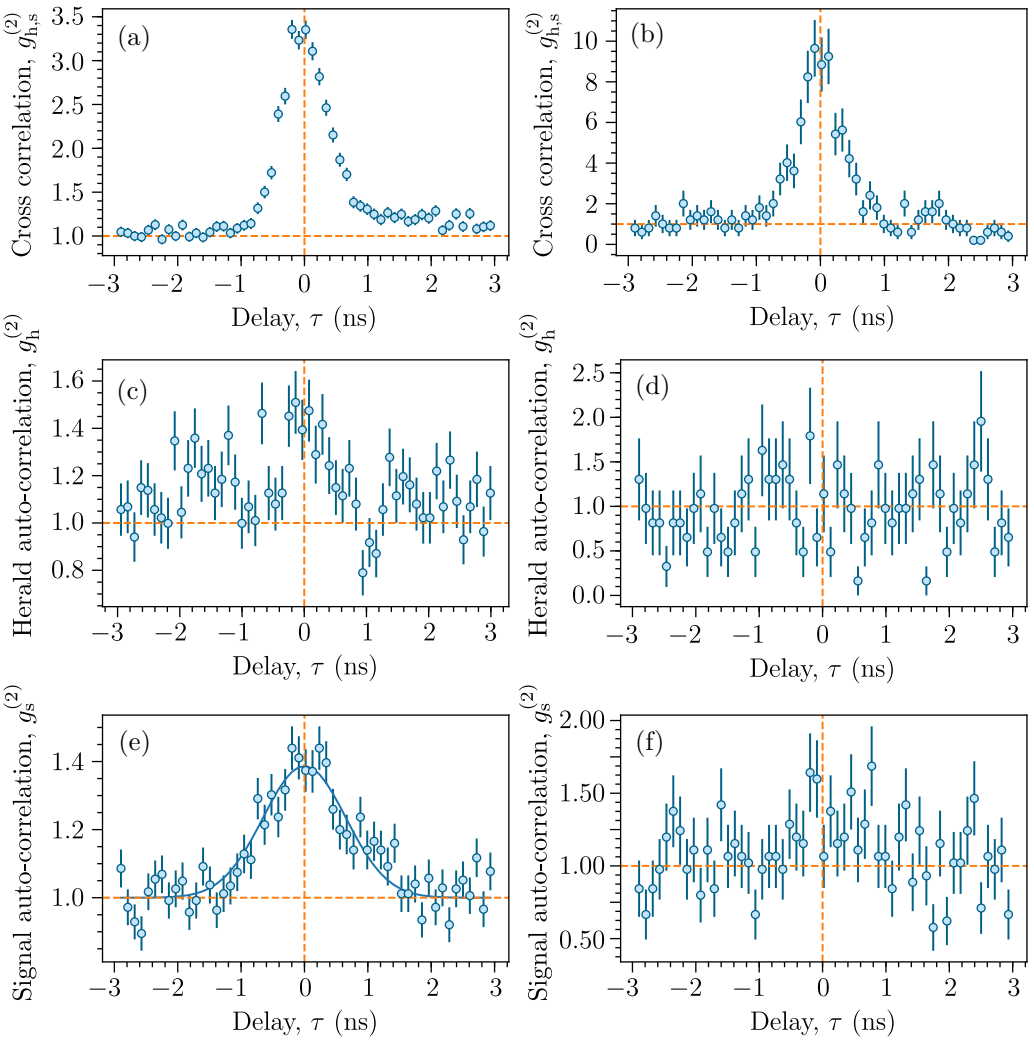

Figure 6.10: Measured cross- and auto-correlations for two different pump detunings: −750 MHz (left) and −1130 MHz (right). The upper row shows the cross-correlation between herald and signal channels, the middle row shows the auto-correlation on the herald channel and the lower row the auto-correlation of the signal channel. The dashed orange lines are guides to the eye.

rates in our experiment were too low to make any meaningful measurement of the inequality in the time frame available.

6.5 Discussion

In our system, we cannot observe conventional *single-atom* quantum beats that originate due to state superposition within the single atom structure [169, 170, 171]. This is because the strong magnetic field enforces only a single decay pathway that can emit photons in the detector direction. Instead, we have observed *collective* beats that originate due to a superposition of atoms with different velocities being in the same internal excited state $|3\rangle$. We note that if one chooses a different geometry where light from the π transitions can be detected, the single-atom quantum beat frequency will be of the order of 10s of GHz due to the large splitting of the intermediate states.

Beating of light fields emitted by two groups of atoms with different velocities has previously been observed in superradiant emission from thermal ensembles after pulsed excitation [172]. However, these superradiant beats cannot be observed on a single photon level, since which-path information is stored in the excited state regarding which atoms decay in the process; one could in principle check, for each emitted photon, which velocity class is in the excited state. Similarly, if one were to use an energy resolving detector in our system, that could distinguish which velocity class emitted the photon, the beats would cease to be observed. Finally, we note that single photon beats have been observed in cold atoms (only one velocity class) by using an additional laser to dress the levels involved [164, 173].

With near resonant driving, the observed lifetime of the collective coherence is on the order of the excited state lifetime. During this coherence time, atoms in different velocity groups can be independently perturbed by external fields, e.g. by exploiting their Doppler shifted optical resonances with coherent driving. An applied perturbation would imprint a different phase on the excitation stored in each velocity group, which could be directly measured

by the accompanying change in the herald-signal correlation. In future an inverted-Y scheme could be used, combining a typical Λ scheme with an additional laser that strongly dresses the intermediate state [174]. This would enable storage and deterministic retrieval of the split single-photon, due to the long lived ground-state coherences and longer spin-wave period [175]. During the storage time the usual qubit rotation operations could be performed by applying off-resonant driving that imprints a relative phase via the AC-Stark shift.

By detuning the coupling field we can engineer the situation that the heralded single-photon has primarily two frequency components, corresponding to the two excited atomic velocity groups. By choosing the detuning Δ_c and driving strength Ω_c of the coupling laser, with wavevector k, one can set the velocities v_z of the two excited velocity groups and thereby tune the two frequency components of the single photon. Such a two-color photon may be a useful resource for entangling two spatially separated atomic quantum memories. In such a scheme each memory would absorb one part of the two-color photon. A symmetric resource state can be prepared by resonant driving ($\Delta_c = 0$) that symmetrically excites two velocity classes, moving in opposite directions with velocities $\pm\Omega_c/(k\sqrt{8})$ set by the coupling laser power through Ω_c. Alternate diamond schemes in rubidium, that utilise the $6S_{1/2}$ level instead of the $5D_{3/2}$ level, would allow for the generation of telecoms-wavelength single photons [116].

6.6 Summary

In summary, we have investigated SFWM in the HPB regime as a source of heralded single-photons. The excellent agreement between theory and experiment demonstrates that atoms in strongly-dressed thermal vapors [176] offer a reliable platform for quantum-state engineering. The addition of external magnetic fields allows for selective excitation and observation of well-defined simple systems that can be completely and accurately modelled [82, 47].

The excellent understanding and control of the state preparation achieved in our experiment compares very favourably to the cases without control over the initial state, like recent experiments in pulse-seeded four-wave mixing [130, 115]. Collective excitation of two velocity groups is an example of an entangled state that is robust against single-atom loss and dephasing [177]. With the emission of two-color heralded single photons providing a direct relative phase measurement, and tunability of the atomic response through adjustments to the dressing laser, these states can be further explored in protocols for quantum state control of atoms and light.

Chapter 7

Summary and Outlook

7.1 Summary

We initially set out to investigate nonlinear optical phenomena in the regime of a large magnetic field, known as the hyperfine Paschen-Back (HPB) regime. One of the main motivations behind this was that previous investigations of the HPB regime in rubidium vapours revealed the ability to selectively interact with atoms in a single quantum state, despite the usual problem of motional broadening, and without the need for complex state preparation techniques. This state-selection is particularly promising for applications involving nonlinear phenomena, where high levels of control are often required to achieve optimum operation of devices. We have therefore investigated the nonlinear effects of electromagnetically induced transparency (EIT) and absorption (EIA) and four-wave mixing (FWM) in the HPB regime.

In chapter 3 we experimentally investigated EIT. We found that the state selection previously observed in two-level systems also applies in this case, meaning that the observed EIT resonances are, to a very good approximation, due only to individual 3-level systems. This enabled us to achieve excellent agreement between experiment and theory in fitting the transmission lineshapes. Making use of this agreement, we directly measured an excited-state dipole

matrix element, which has hitherto only been possible indirectly through lifetime measurements. We measured the value of the rubidium $5P_{3/2} \rightarrow 5D_{5/2}$ transition to be $|\langle 5P_{3/2}||er||5D_{5/2}\rangle| = (2.27 \pm 0.002_{\text{stat}} \pm 0.04_{\text{syst}})\ ea_0$.

In chapter 4 we observed resonant EIA for the first time in a non-degenerate three-level ladder system, demonstrating that a 4-level system is not required. A second coupling beam was added, in a standing-wave geometry, to a standard Doppler-free EIT configuration. This resulted in the dramatic change from resonant EIT to a narrow window of enhanced absorption. Again, we found that the state-selection allowed for excellent agreement between the experimental transmission spectra and the developed 3-level theory. Further, the relative simplicity of the model clearly exposes the origin of enhanced absorption in these systems where fast velocity classes contribute strongly to the overall absorption. On resonance, the light shift of the excited state (normally resulting in EIT) is cancelled by the additional laser field for all velocity classes, resulting in enhanced absorption. The resultant line-shapes provide an explanation of structure observed in the residuals in the dipole matrix element measurement.

In chapter 5 we conducted an experimental study of seeded non-degenerate FWM in the HPB regime. In zero magnetic field the FWM spectra exhibit multi-path interferences which are difficult to model and obscure the underlying physics. Applying the magnetic field removed the multi-path interference so that we observed text-book FWM resonances that could be quantitatively explained with a simple 4-level model even in the regime of strong driving. We investigated the dependence of the FWM signal on laser detunings, powers and the atomic density of the vapour, on the whole finding excellent agreement between theory and experiment.

Finally, in chapter 6 we studied spontaneous FWM as a heralded source of single photons. The addition of external magnetic fields allowed for selective excitation of a single internal state of the atoms. Strong laser dressing and heralding lead to the collective excitation of two well-defined atomic velocity classes, which is an example of an entangled state that is robust against single

atom loss and dephasing [177]. The collective state emits a bi-chromatic single photon, the two-frequency nature of which is observed as oscillations in the photon detection probability over time. Finally, we observed a strong violation (6.7 standard deviations) of the Cauchy-Schwarz inequality using off resonant driving. Operating in the HPB regime allowed for excellent understanding and control of the system, demonstrated by the high levels of agreement found between experiment and theory. Similar operation can be obtained over a wide range of operating frequencies by tuning of the magnetic field.

In general, the more atomic states involved in a particular process, the more computationally demanding it becomes to accurately model. In many cases, this means that there is a trade-off between speed and accuracy in the modelling. Since working in the HPB regime can reduce the number of coupled states, it can significantly decrease the time taken to accurately model the system. Following on from the development of a range of technologies based on linear atom-light interactions in strong magnetic fields [131, 41, 42, 43], we envision that similar comprehensive modelling of nonlinear systems will enable the design and optimisation of future devices. Finally, we would like to point out that the simplifications afforded by working in the HPB regime are not only applicable to fundamental physics research, but may also find application in teaching laboratories, where it would allow for a more foundational approach. The permanent magnets used to gain access to the HPB regime are inexpensive and readily available and would make an excellent addition to any optics laboratory.

7.2 Outlook

The work contained within this thesis is by no means a complete study of all nonlinear effects in the HPB regime. There are several avenues of investigation that we have been unable to pursue due to time limitations. In this final section we will put forward some ideas for future investigations.

In the investigation of EIA we showed that by controlling the power in the co-propagating coupling laser, it is possible to switch from reduced absorption (EIT) to enhanced absorption (EIA) in a narrow frequency window. This being the case, further investigations could lead to the implementation of simpler and more efficient all-optical switching protocols. In addition, concomitant with the change from EIT to EIA is a change from normal to anomalous dispersion, which may be interesting to study as a method of rapidly switching between subluminal and superluminal propagation of pulses in the medium.

In the single-photon generation experiment, we chose to use a Doppler-selective beam geometry as the velocity selection enabled the generation of photons with spectral widths matched to atomic transitions. It would be interesting to extend our investigation to Doppler-free geometries. In such a geometry, all velocity classes are excited, resulting in a high brightness source of single photons, although at the cost of short coherence times for the emitted photons [75]. Another modification worth considering is the change from focussed to unfocussed driving fields. Currently, a lens must be used for collection of the photon pairs. Unfortunately this also collimates the uncorrelated fluorescence which leads to a large background, low correlation and low heralding efficiency. Using larger beams would mean the collection lens could be moved further from the atoms, reducing the number of collected background photons. Working in the Voigt geometry (with the magnetic field orientation perpendicular to the driving fields), the photons can even be generated on-resonance with the zero-field transitions, for compatibility with existing technologies.

Another exciting possibility is the study of quantum memories in the HPB regime. An illustration of a Λ-type quantum memory (based on the DLCZ scheme [178]) is shown in figure 7.2. The operation of this type of quantum memory can be described as follows. Initially the atomic population is prepared in a single ground-state $|g_1\rangle$. Occasionally, a photon is scattered from the weak control field into a detector, signalling the storage of a single excitation in the second long-lived ground-state $|g_2\rangle$. The control field can then be switched off. After some time, a different laser field can be applied in

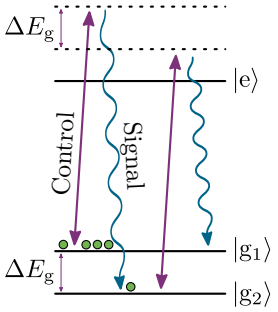

Figure 7.1: Illustration of a Λ-type quantum memory.

order to coherently retrieve the stored excitation. Currently, one of the effects limiting the efficiency of atomic quantum memories is parasitic FWM [179, 180]. In this process, the efficiency of the memory is limited because the initial control field that stores the excitation, also immediately retrieves it. Due to the usually small energy separation of the ground states ΔE_g, the coupling field is near resonant with the transition $|g_2\rangle \leftrightarrow |e\rangle$, which leads to a significant amount of this parasitic FWM. In the HPB regime, the ground state splitting can be increased dramatically, which would significantly reduce this effect.

Over the course of this work we have demonstrated that working in the HPB regime vastly reduces the complexity of modelling nonlinear atom-light interactions in thermal vapours. We note however, that we have only investigated a fraction of the nonlinear phenomena that may be enhanced or at least simplified by making use of the HPB regime. We hope that our investigation opens up new possibilities for studying coherent phenomena in many-level systems. As for nonlinear optics in thermal vapours, there is light at the end of the tunnel, and it's single photons.

Appendix A

Magnetic-field profile

To generate the strong magnetic field needed to study the HPB regime we use a pair of cylindrical top-hat shaped permanent magnets separated by 15 mm. A cross sectional view with the magnet dimensions is shown in figure A.1(a) along with an image of the magnets held in place by an aluminium block in (b). The magnetic field B_z along the axis of symmetry z of a single annular magnet, which is positioned at z_0, is given by [181]

$$B_z(z) = \frac{B_r}{2}\left(\frac{z+z_0+t}{\sqrt{(z+z_0+t)^2+R^2}} - \frac{z+z_0-t}{\sqrt{(z+z_0-t)^2+R^2}}\right) \tag{A.1}$$

$$- \frac{B_r}{2}\left(\frac{z+z_0+t}{\sqrt{(z+z_0+t)^2+r^2}} - \frac{z+z_0-t}{\sqrt{(z+z_0-t)^2+r^2}}\right) \tag{A.2}$$

where B_r is the remanence of the magnet, and $2t$, R and r are the thickness, outer radius and inner radius of the magnet respectively. The magnets are axially magnetised and are made from N52 grade NdFeB alloy with a remanence previously measured to be 1.42 T [40]. The two magnets are arranged in a Helmholtz geometry, such that the fields add constructively at $z = 0$. Via the superposition principle, the total magnetic field is given by the sum of equation A.2 over each of the four annular rings of magnetic material. Based on the specified magnet proporties, the calculated axial

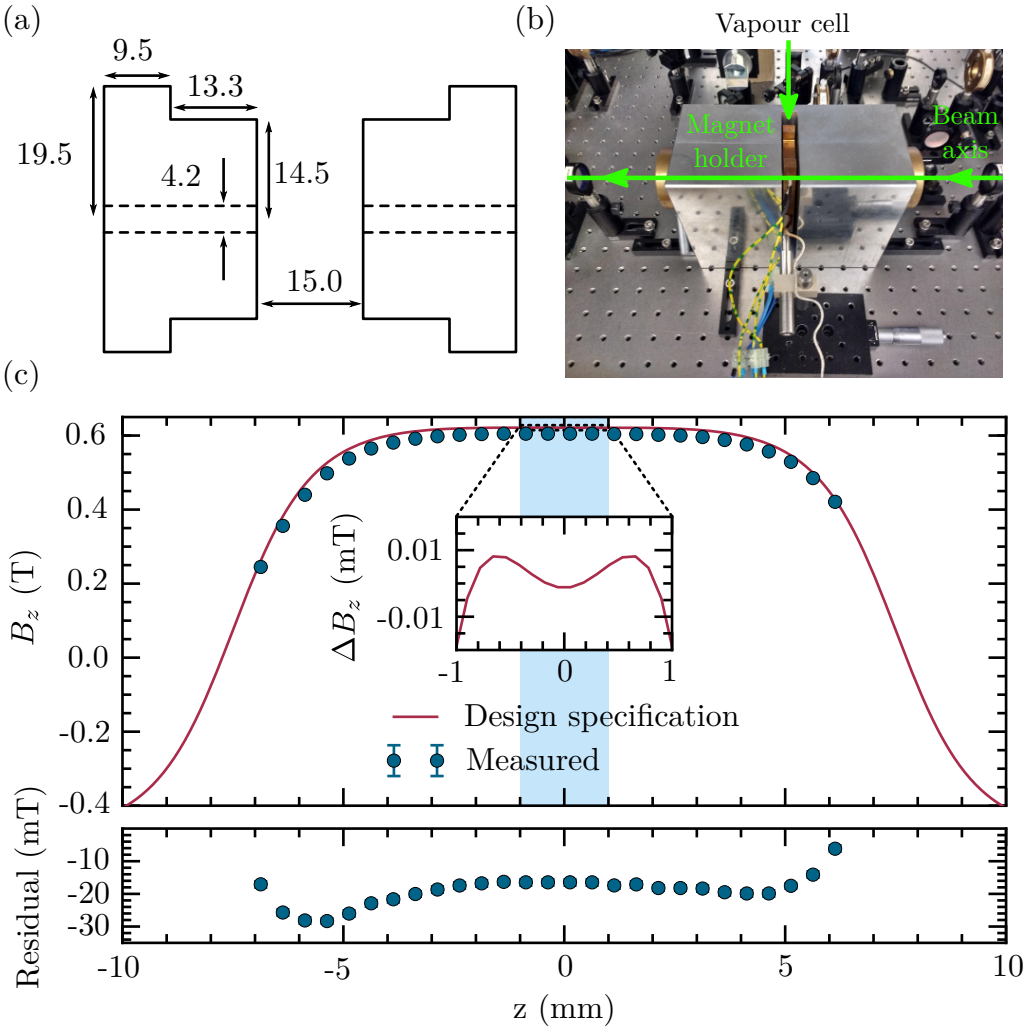

Figure A.1: (a) The dimensions of the magnets and their separation in mm. (b) An image of the magnets held in an aluminium block. (c) The axial magnetic field profile between the magnets. The blue dots show the measured values with error bars two small to see. The solid red line shows the predicted magnetic field for the design specification. The difference of ~ 20 mT seen in the residuals is likely due to a slight demagnetization of the Neodymium since purchase. The inset shows the field variation over the space normally occupied by the vapour cell (blue shaded region) which has an rms variation of 4 μT.

magnetic field is displayed in figure A.1(c) as a function of z. With this magnet specification we expect a B-field at $z = 0$ of 0.62 T, which is more than sufficient to enter the HPB regime for rubidium. In the region occupied by the vapour cell ($-1 < z < 1$ mm) the magnetic field variation (shown in the inset) should be less than 4 μT. A variation this small lead to less than 0.1 MHz broadening of the rubidium D_2 transitions. The axial magnetic field was experimentally measured with a Hall probe and the results are shown by the blue dots in figure A.1(c). The maximum measured value of the field was 0.605 ± 0.005 T, which has been independently verified by fitting of the weak probe D_2 transmission spectra using the ElecSus code [29]. The difference of ~ 20 mT (clearly seen in the residuals) is likely due to a slight demagnetization of the Neodymium since purchase. The measurements of the field variation over the region occupied by the vapour cell are in agreement with the theoretical calculation, showing zero variation within the 1 mT measurement uncertainty.

The theoretically calculated variation of the magnetic field (4 μT) assumed that the vapour cell was positioned exactly between the two magnets and that the magnets were separated by exactly 15 mm. In fact, the rms variation depends strongly on the axial position of the vapour cell, as is show in figure A(a). From the theoretical model we find that the cell must be positioned centrally between the magnets to a precision of better than $\sim$1 mm in order to avoid additional broadening of the transition lines. Maintaining this alignment can be challenging given that often the cell must be tilted to reduce unwanted back reflections of the beams within the vapour. Furthermore it is important to set the separation of the magnets correctly. In the case of our magnets design specification, we find that the separation must be set to 15.0 ± 2 mm to avoid additional line broadening [figure A(b)]. Finally, we note that these values are calculated based on the rms variation of the field and the $\sim$14 MHz/mT shift of the Rb ground-state energy levels in an applied B-field. If we choose to use the peak to peak variation of the B-field as a measure for the additional line-broadening, clearly the requirements on the positioning of the vapour cell and magnets become more stringent.

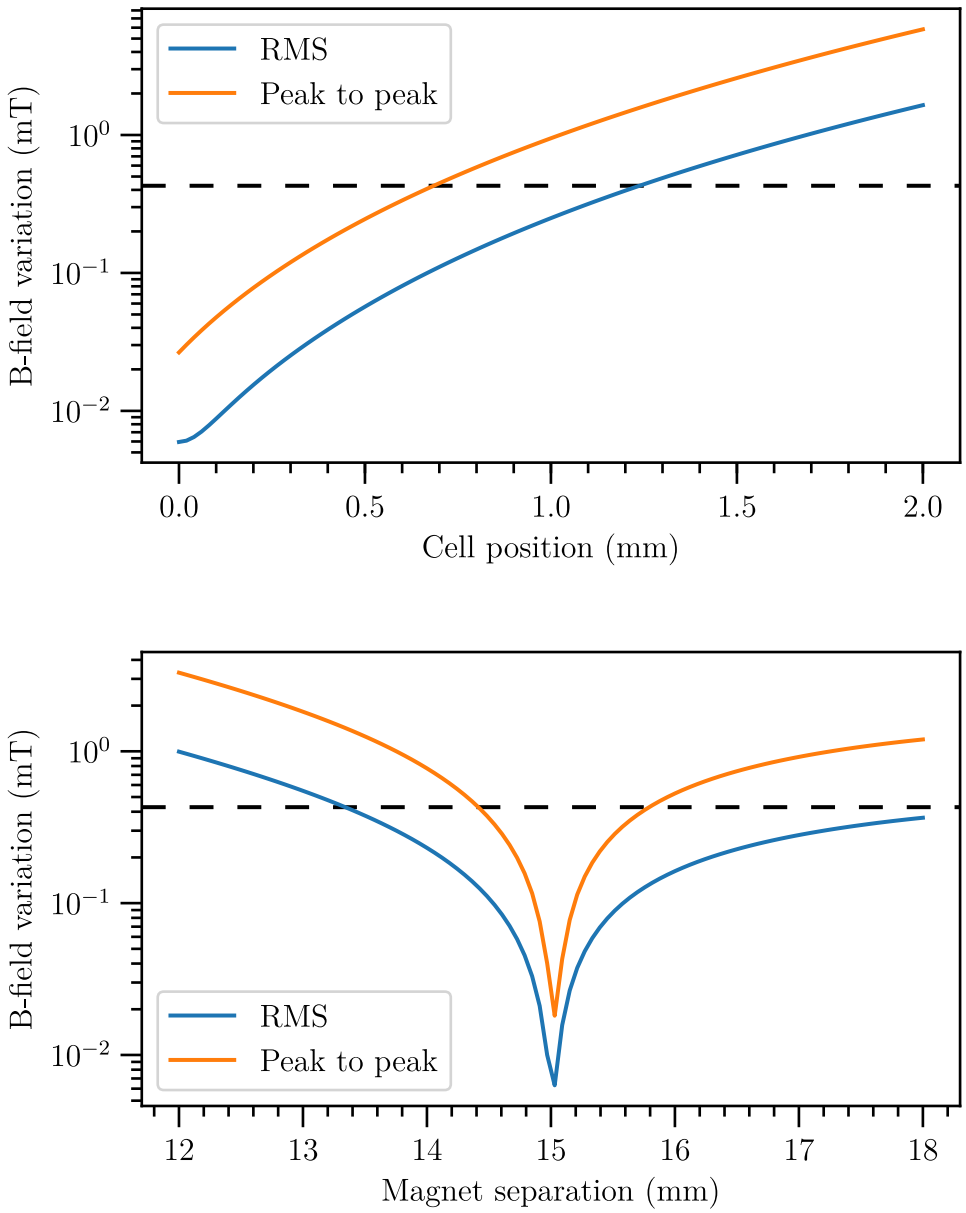

Figure A.2: The rms and peak-to-peak variation of the axial B-field over the extent of the vapour cell as a function of the cell position and the separation of the magnets. The dashed horizontal lines show the rms variation that corresponds to a broadening of rubidium D_2 σ-transitions by approximately 6 MHz.

Appendix B

The weak-probe regime

In figure 2.2 we showed the theoretical transmission spectra of a weak probe field on a closed transition. As the intensity of the probe field is increased, the steady-state population of the excited state increases until it saturates at half the ground state population. The saturation is caused by the appearance of stimulated emission which drives population out of the excited state. In a fully saturated medium the rates of absorption and stimulated emission are equal and therefore any additional photons in the driving field are transmitted. Thus saturation appears as the increased transmission of a driving field of increasing intensity. The saturation of the on-resonance absorption coefficient for a gas of stationary atoms is characterised by $\alpha = \alpha_0/(1 + I/I_{\text{sat}})$ where the saturation intensity $I_{\text{sat}} = 2\pi^2\hbar c/(3\lambda^3\tau)$ [182]. In the case of a thermal vapour however, not all of the atoms interact resonantly with the driving field, since their motion Doppler shifts the driving field out of resonance. This has two effects: firstly, for an equal atomic number density, the value of α_0 is significantly reduced, and secondly, there is a new form of saturation behaviour $\alpha = \alpha_0'/\sqrt{1 + I/I_{\text{sat}}}$ [183].

In rubidium atoms the excited-state population can usually decay to several ground-states where it is no longer coupled to the driving field (optical pumping). This can lead to a massive reduction in the effective I_{sat} [55].

In practice the field has a finite extent and atoms leaving the interaction region will remain optically pumped until they undergo ground-state hyperfine changing collisions with other atoms or the vapour cell walls. Therefore the populations of the atomic states depend strongly on the beam size, the amount of buffer gases present and whether or not the vapour cell walls are anti-relaxation coated. Furthermore, atoms transit the beam before reaching a steady state and transit-time effects must be considered [184]. Indeed, even the concept of a saturation intensity becomes questionable when a steady-state is not reached.

A more practical definition of the weak-probe regime is where the absorption coefficient becomes independent of the driving field intensity. The experimentally measured transmission or resonance with the D_2 $|\frac{1}{2},\frac{3}{2}\rangle \rightarrow |\frac{3}{2},\frac{3}{2}\rangle$ transition, is plotted for various probe intensities in figure B.1.

The data clearly show that saturation occurs for probe powers much larger than I_{sat}. We have fitted to the data the expected saturation function for a thermal vapour with I_{sat} scaled by the free parameter b. We find qualitative agreement with the formula using $b = 5.4 \pm 0.1$. i.e. we find that saturation occurs at significantly higher beam intensities than the theoretical I_{sat}! One potential explanation of this increase is transit time effects due to the small ($1/e^2$ radius 50 μm) beam size. For an approximate calculation, consider an atom moving at the most probable speed, $v_{\text{p}} = \sqrt{2k_{\text{B}}T/m} \approx 255$ ms^{-1} for $T = 70$ C. The time taken to cross the beam is $\sim$200 ns whereas the time taken for resonant atoms to reach a steady-state is much shorter, on the order of the excited state lifetime (27 ns). From this calculation we would therefore expect negligible transit-time effects since, at any one time, most of the atoms in the beam should be in the steady-state. Clearly a more detailed study is required and this will be the subject of an ongoing investigation.

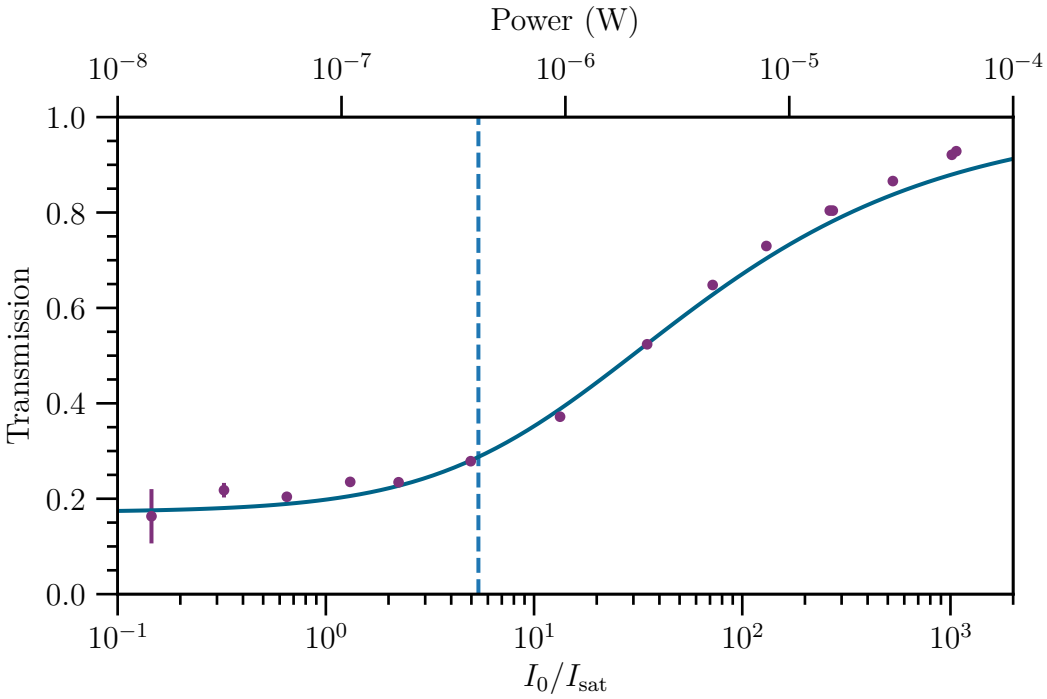

Figure B.1: Experimental measurements of the weak-probe regime with focussed laser beams. The transmission on resonance with the D_2 $|\frac{1}{2}, \frac{3}{2}\rangle \rightarrow |\frac{3}{2}, \frac{3}{2}\rangle$ transition is plotted for various beam intensities (purple points). A model for saturation (described in the text) has been fitted to the data (blue line). The dashed vertical blue line shows the saturation intensity determined by the fit.

Appendix C

Laser-frequency stabilisation

Throughout the course of the experiments presented in this thesis several different laser-frequency stabilisation methods have been used. For the data presented in chapter 3 the laser frequencies were not actively stabilised.

C.1 Optical cavity method

In chapter 4 the experiment required frequency stabilisation of the coupling laser (776 nm), which was achieved using the following method.

Firstly, an additional laser which we call the reference laser, has its frequency actively stabilised to that of an atomic transition. An error signal is generated by polarisation spectroscopy of rubidium [185] and the feedback electronics follow a standard PID configuration [186]. Secondly, the transmission of light from the reference laser, through an optical cavity, is monitored on a high-gain photo diode. Application of a periodic linear voltage ramp (at a frequency of $\sim$100 Hz) to a piezo-electric stack attached to one of the cavity mirrors, changes the length of the cavity by several wavelengths, generating a comb of cavity transmission lines in the photo-diode signal. Simultaneously monitoring the transmission of the coupling laser through the cavity (on a

second photo diode), we observe another comb of transmission lines. Since the reference-laser comb provides an absolute frequency reference, stabilising the coupling laser amounts to maintaining the offset (in time) between the two combs. The outputs of the two photo-diodes are monitored by comparator chips which transfer the analogue inputs into digital outputs that are logic high above a manually set threshold voltage, and logic low otherwise. These outputs are monitored by a micro-controller that is programmed to output, via an digital to analogue converter (DAC), a PID feedback signal to stabilise the laser frequency via the voltage applied to its scan control.

This method enables the stabilisation frequency to be tuned arbitrarily which was important in obtaining the detuning-map presented in figure 4.7(a). One limitation of the method is that the cavity transmission signals are susceptible to noise (including acoustic noise) on the cavity which translates into instability. Additionally, the feedback response rate is limited by the cavity scan rate, which cannot be increased beyond the mechanical response rate of the piezo driving the motion of the cavity mirror.

C.2 Faraday-rotation method

In chapters 5 and 6 the experiments required active stabilisation of the pump laser (780 nm). The stabilisation scheme is based upon the measurement of optical rotation due to the Faraday effect near an atomic resonance.

For an atomic medium in an external magnetic field, the refractive indices for left- and right-hand circularly polarised light differ. Therefore, on propagating through the vapour, light that is initially linearly polarised will have its plane of polarisation rotated by an amount proportional to the (real part of the) refractive index difference. The amount of rotation depends on the detuning of the light from the atomic transitions and this dependence forms the basis of our laser-frequency stabilisation. The rotation can be measured with the Stokes-parameter $S_1 = I_x - I_y$ [187] which is the difference between the intensities of the orthogonal linear polarisation components of the light. Each

full (2π) rotation of the polarisation leads to a zero crossing in S_1 which we can stabilise the laser frequency to by using a PID feedback loop. In order to create a suitable zero crossing at the intended frequency of laser operation, a large magnetic field is applied (of strength 0.3-0.6 T), pushing the atoms into the HPB regime. Faraday rotation in this regime has been investigated in detail in [45]. The set-up in figure C.2(a) is used to measure S_1.

The vapour cell has a thickness of 1 mm and contains isotopically enriched ^{87}Rb. It is placed between a pair of permanent magnets with the same design specifications as those used in the main part of the experiment but with a larger separation to reduce the field strength in the vapour cell. Light from the pump laser is prepared in a linear polarisation by a polarising beam splitter (PBS). It then passes through a half-wave plate which is set to rotate the plane of polarisation by 45°. After propagating through the atomic vapour it is split into orthogonal linear polarisation components I_x and I_y (by a PBS) which are measured by a differencing photo-diode circuit. The theoretical weak-probe transmission spectrum (at 80°C) and S_1 spectrum (at 125°C), for a magnetic field strength of 0.6 T, are shown in figure C.2(b,c).

The zero-crossing most frequently used for stabilisation in the experiments is indicated by an arrow on panel (b) of the figure. On either side of resonance the dispersion (and therefore rotation) has the opposite sign, this means that half-way between two resonances of the same strength the light is not rotated. The position of this zero-crossing in the spectrum is therefore only weakly dependent on the number density (typically < 1 MHz/°C) meaning that the cell temperature need not be actively stabilised. However, we most often require the laser to be stabilised to a different frequency. This is simply achieved by changing the separation between the magnets which shifts the atomic resonances, and therefore shifts the zero-crossing to the necessary frequency.

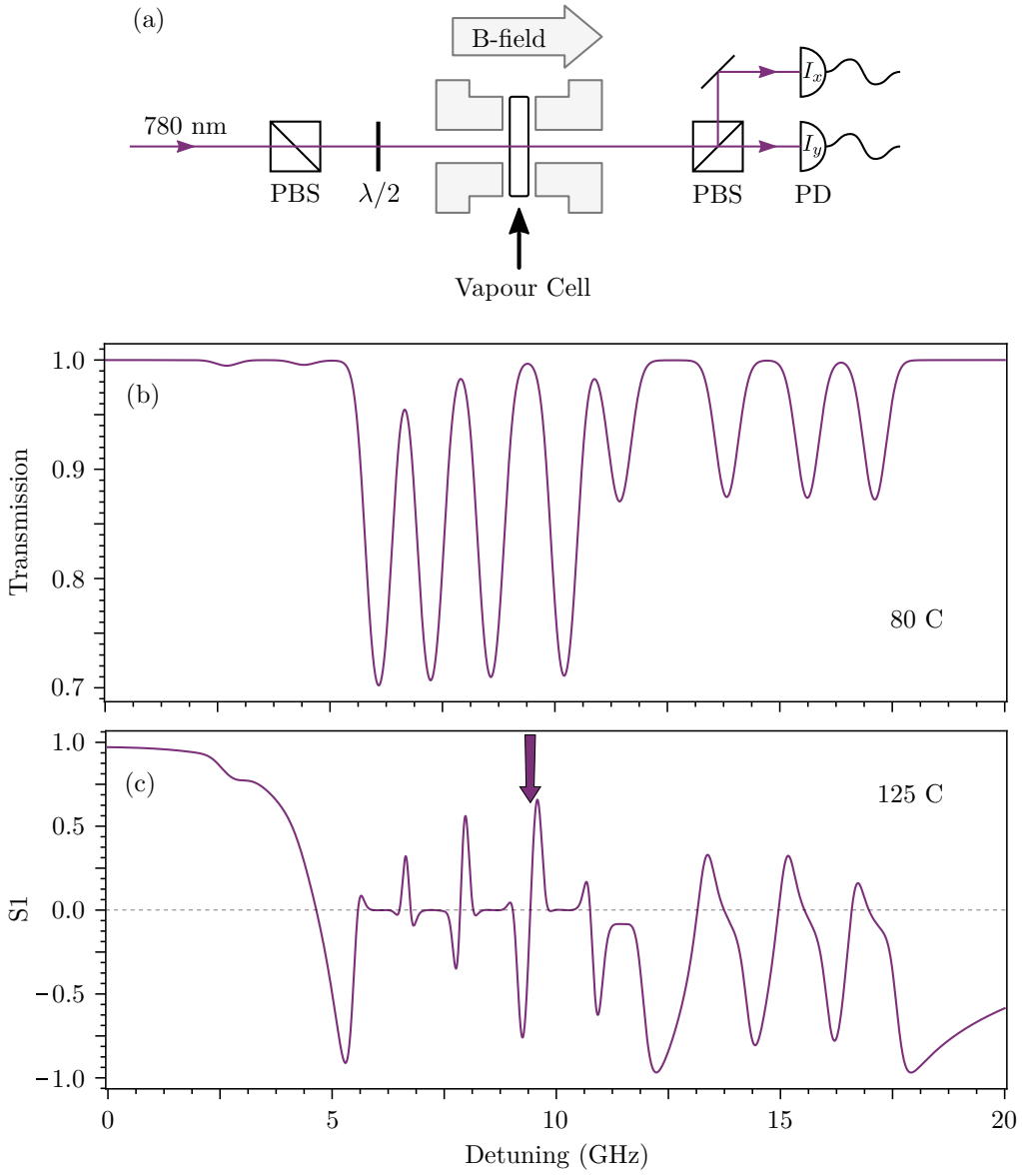

Figure C.1: Laser frequency stabilisation using Faraday rotation. (a) the experimental set-up used to measure the rotation signal $S_1 = I_x - I_y$. The half-wave plate $\lambda/2$ is set to rotate the plane of polarisation by 45°. (b) the theoretical weak-probe transmission spectrum ($S_0 = I_x + I_y$) for a temperature of 80°C. (c) the theoretical S_1 spectrum for a temperature of 125°C with an arrow indicating the zero crossing which is most-often used for frequency stabilisation.

Appendix D

Frequency calibration of atomic spectra

Many of the data presented in this thesis take the form of atomic spectra where some electronic signal is measured over time as the frequency of a laser is scanned. In order to convert the raw signals over time (acquired using an oscilloscope) into quantitative spectra with known frequencies, we simultaneously measure the transmission of light from the same laser through an optical cavity. The optical cavity has a measured free-spectral range of 375 ± 1 MHz. By extracting the locations (in time) of the cavity transmission peaks and fitting a polynomial of order 5, we are able to convert between time and (relative) frequency units and also to account for any non-linearity of the laser scan frequency over time. Additionally, the absolute frequencies can be determined by simultaneously performing hyperfine pumping spectroscopy [88] in a second vapour cell (in zero magnetic field), measuring the frequencies of the rubidium hyperfine transitions, and comparing to the known values. In a typical experimental run we obtain an absolute frequency calibration uncertainty of ~ 1 MHz for the weighted line-centre of naturally abundant Rb.

In the case of chapter 4, the optical cavity was used for laser frequency

stabilisation and was therefore unavailable for use as a frequency reference. Instead, the frequency axis of the probe transmission spectrum was calibrated by measuring the vapour-cell temperature to calculate the Doppler width and subsequently fitting the theoretical Voigt lineshape [80, 188].

Bibliography

[1] R. W. Boyd. *Nonlinear Optics*. Elsevier Science (2003). [Cited on page 1.]

[2] T. H. Maiman. *Stimulated Optical Radiation in Ruby*. Nature **187**, 493 (1960). [Cited on page 2.]

[3] M. Jain, H. Xia, G. Y. Yin, A. J. Merriam, and S. E. Harris. *Efficient Nonlinear Frequency Conversion with Maximal Atomic Coherence*. Physical Review Letters **77**, 4326 (1996). [Cited on page 2.]

[4] M. Fleischhauer and M. D. Lukin. *Dark-State Polaritons in Electromagnetically Induced Transparency*. Physical Review Letters **84**, 5094 (2000). [Cited on pages 2 and 89.]

[5] M. D. Lukin and A. Imamoğlu. *Nonlinear Optics and Quantum Entanglement of Ultraslow Single Photons*. Physical Review Letters **84**, 1419 (2000). [Cited on page 2.]

[6] M. Fleischhauer, A. Imamoglu, and J. P. Marangos. *Electromagnetically induced transparency: Optics in coherent media*. Reviews of Modern Physics **77**, 633 (2005). [Cited on pages 2, 23, 59, 69, and 81.]

[7] S. E. Harris. *Electromagnetically Induced Transparency*. Physics Today **50**, 36 (1997). [Cited on pages 2 and 51.]

[8] H. R. Gray, R. M. Whitley, and C. R. Stroud. *Coherent trapping of atomic populations*. Optics Letters **3**, 218 (1978). [Cited on pages 2 and 51.]

[9] T. Hong, C. Cramer, W. Nagourney, and E. N. Fortson. *Optical Clocks Based on Ultranarrow Three-Photon Resonances in Alkaline Earth Atoms*. Physical Review Letters **94**, 050801 (2005). [Cited on page 2.]

[10] R. Santra, E. Arimondo, T. Ido, C. H. Greene, and J. Ye. *High-Accuracy Optical Clock via Three-Level Coherence in Neutral Bosonic ^{88}Sr.* Physical Review Letters **94**, 173002 (2005). [Cited on page 2.]

[11] V. I. Yudin, A. V. Taichenachev, Y. O. Dudin, V. L. Velichansky, A. S. Zibrov, and S. A. Zibrov. *Vector magnetometry based on electromagnetically induced transparency in linearly polarized light.* Physical Review A **82**, 033807 (2010). [Cited on pages 2 and 24.]

[12] L. V. Hau, S. E. Harris, Z. Dutton, and C. H. Behroozi. *Light speed reduction to 17 metres per second in an ultracold atomic gas.* Nature **397**, 594 (1999). [Cited on page 2.]

[13] J. Keaveney, A. Sargsyan, U. Krohn, I. G. Hughes, D. Sarkisyan, and C. S. Adams. *Cooperative Lamb Shift in an Atomic Vapor Layer of Nanometer Thickness.* Physical Review Letters **108**, 173601 (2012). [Cited on pages 2, 4, and 24.]

[14] H. J. Kimble. *The quantum internet.* Nature **453**, 1023 (2008). [Cited on page 2.]

[15] M. D. Lukin, S. F. Yelin, and M. Fleischhauer. *Entanglement of Atomic Ensembles by Trapping Correlated Photon States.* Physical Review Letters **84**, 4232 (2000). [Cited on page 2.]

[16] T. Peyronel, O. Firstenberg, Q.-Y. Liang, S. Hofferberth, A. V. Gorshkov, T. Pohl, M. D. Lukin, and V. Vuletić. *Quantum nonlinear optics with single photons enabled by strongly interacting atoms.* Nature **488**, 57 (2012). [Cited on page 2.]

[17] I. Friedler, G. Kurizki, and D. Petrosyan. *Deterministic quantum logic with photons via optically induced photonic band gaps.* Physical Review A **71**, 023803 (2005). [Cited on page 2.]

[18] A. Reiserer, N. Kalb, G. Rempe, and S. Ritter. *A quantum gate between a flying optical photon and a single trapped atom.* Nature **508**, 237 (2014). [Cited on page 2.]

[19] L. Isenhower, E. Urban, X. L. Zhang, A. T. Gill, T. Henage, T. A. Johnson, T. G. Walker, and M. Saffman. *Demonstration of a Neutral Atom Controlled-NOT Quantum Gate.* Physical Review Letters **104**, 010503 (2010). [Cited on page 2.]

[20] K. Hammerer, A. S. Sørensen, and E. S. Polzik. *Quantum interface between light and atomic ensembles.* Reviews of Modern Physics **82**, 1041 (2010). [Cited on pages 2 and 89.]

[21] A. MacRae, T. Brannan, R. Achal, and A. I. Lvovsky. *Tomography of a High-Purity Narrowband Photon from a Transient Atomic Collective Excitation.* Physical Review Letters **109**, 033601 (2012). [Cited on pages 2, 70, and 90.]

[22] R. T. Willis, F. E. Becerra, L. A. Orozco, and S. L. Rolston. *Correlated photon pairs generated from a warm atomic ensemble.* Physical Review A **82**, 053842 (2010). [Cited on pages 2, 90, and 91.]

[23] B. Srivathsan, G. K. Gulati, B. Chng, G. Maslennikov, D. Matsukevich, and C. Kurtsiefer. *Narrow Band Source of Transform-Limited Photon Pairs via Four-Wave Mixing in a Cold Atomic Ensemble.* Physical Review Letters **111**, 123602 (2013). [Cited on pages 2 and 105.]

[24] D. J. Saunders, J. H. D. Munns, T. F. M. Champion, C. Qiu, K. T. Kaczmarek, E. Poem, P. M. Ledingham, I. A. Walmsley, and J. Nunn. *Cavity-Enhanced Room-Temperature Broadband Raman Memory.* Physical Review Letters **116**, 090501 (2016). [Cited on pages 2 and 90.]

[25] M. Hosseini, G. Campbell, B. M. Sparkes, P. K. Lam, and B. C. Buchler. *Unconditional room-temperature quantum memory.* Nature Physics **7**, 794 (2011). [Cited on pages 2 and 90.]

[26] A. I. Lvovsky, B. C. Sanders, and W. Tittel. *Optical quantum memory.* Nature Photonics **3**, 706 (2009). [Cited on pages 2 and 90.]

[27] J. Nunn, N. K. Langford, W. S. Kolthammer, T. F. M. Champion, M. R. Sprague, P. S. Michelberger, X.-M. Jin, D. G. England, and I. A. Walmsley. *Enhancing Multiphoton Rates with Quantum Memories.* Physical Review Letters **110**, 133601 (2013). [Cited on pages 2 and 89.]

[28] J. D. Pritchard, K. J. Weatherill, and C. S. Adams. *NONLINEAR OPTICS USING COLD RYDBERG ATOMS.* In K. W. Madison, Y. Wang, A. M. Rey, and K. Bongs (editors), *Annual Review of Cold Atoms and Molecules*, pp. 301–350. WORLD SCIENTIFIC (2013). [Cited on pages 2 and 89.]

[29] M. A. Zentile, J. Keaveney, L. Weller, D. J. Whiting, C. S. Adams, and I. G. Hughes. *ElecSus: A program to calculate the electric susceptibility*

of an atomic ensemble. Computer Physics Communications **189**, 162 (2015). [Cited on pages 3, 4, 16, 24, 33, 62, 77, and 131.]

[30] J. Kitching, S. Knappe, and L. Hollberg. *Miniature vapor-cell atomic-frequency references*. Applied Physics Letters **81**, 553 (2002). [Cited on pages 3 and 90.]

[31] T. H. Sander, J. Preusser, R. Mhaskar, J. Kitching, L. Trahms, and S. Knappe. *Magnetoencephalography with a chip-scale atomic magnetometer*. Biomedical Optics Express **3**, 981 (2012). [Cited on pages 3 and 90.]

[32] C. G. Wade, N. Šibalić, N. R. de Melo, J. M. Kondo, C. S. Adams, and K. J. Weatherill. *Real-time near-field terahertz imaging with atomic optical fluorescence*. Nature Photonics **11**, 40 (2016). [Cited on page 3.]

[33] J. A. Sedlacek, A. Schwettmann, H. Kübler, R. Löw, T. Pfau, and J. P. Shaffer. *Microwave electrometry with Rydberg atoms in a vapour cell using bright atomic resonances*. Nature Physics **8**, 819 (2012). [Cited on pages 3 and 90.]

[34] L. Cao, J. Qi, J. Du, and J. Jing. *Experimental generation of quadruple quantum-correlated beams from hot rubidium vapor by cascaded four-wave mixing using spatial multiplexing*. Physical Review A **95**, 023803 (2017). [Cited on page 3.]

[35] W. Happer. *Optical Pumping*. Reviews of Modern Physics **44**, 169 (1972). [Cited on page 3.]

[36] H. G. Robinson and C. E. Johnson. *Narrow ^{87}Rb hyperfine-structure resonances in an evacuated wall-coated cell*. Applied Physics Letters **40**, 771 (1982). [Cited on page 3.]

[37] S. J. Seltzer and M. V. Romalis. *High-temperature alkali vapor cells with antirelaxation surface coatings*. Journal of Applied Physics **106**, 114905 (2009). [Cited on page 3.]

[38] M. Faraday. *On the magnetization of light and the illumination of magnetic lines of force*. Philosophical Transactions of the Royal Society of London **136**, 1 (1846). [Cited on page 4.]

[39] A. Yariv and P. Yeh. *Photonics: Optical Electronics in Modern Communications*. Oxford University Press, 6th edition (2006). [Cited on page 4.]

[40] L. Weller, K. S. Kleinbach, M. A. Zentile, S. Knappe, C. S. Adams, and I. G. Hughes. *Absolute absorption and dispersion of a rubidium vapour in the hyperfine Paschen-Back regime*. Journal of Physics B: Atomic, Molecular and Optical Physics **45**, 215005 (2012). [Cited on pages 4, 24, 72, and 129.]

[41] L. Weller, K. S. Kleinbach, M. A. Zentile, S. Knappe, I. G. Hughes, and C. S. Adams. *Optical isolator using an atomic vapor in the hyperfine Paschen-Back regime*. Optics Letters **37**, 3405 (2012). [Cited on pages 4, 24, 86, and 125.]

[42] M. A. Zentile, D. J. Whiting, J. Keaveney, C. S. Adams, and I. G. Hughes. *Atomic Faraday filter with equivalent noise bandwidth less than 1 GHz*. Optics Letters **40**, 2000 (2015). [Cited on pages 4, 24, 86, and 125.]

[43] J. Keaveney, W. J. Hamlyn, C. S. Adams, and I. G. Hughes. *A single-mode external cavity diode laser using an intra-cavity atomic Faraday filter with short-term linewidth <400 kHz and long-term stability of <1 MHz*. Review of Scientific Instruments **87**, 095111 (2016). [Cited on pages 4, 86, and 125.]

[44] P. Zeeman. *The Effect of Magnetisation on the Nature of Light Emitted by a Substance*. Nature **55**, 347 (1897). [Cited on page 4.]

[45] M. A. Zentile, R. Andrews, L. Weller, S. Knappe, C. S. Adams, and I. G. Hughes. *The hyperfine Paschen-Back Faraday effect*. Journal of Physics B: Atomic, Molecular and Optical Physics **47**, 075005 (2014). [Cited on pages 4, 24, 52, 72, and 139.]

[46] B. A. Olsen, B. Patton, Y.-Y. Jau, and W. Happer. *Optical pumping and spectroscopy of Cs vapor at high magnetic field*. Physical Review A **84**, 063410 (2011). [Cited on page 4.]

[47] D. J. Whiting, J. Keaveney, C. S. Adams, and I. G. Hughes. *Direct measurement of excited-state dipole matrix elements using electromagnetically induced transparency in the hyperfine Paschen-Back regime*. Physical Review A **93**, 043854 (2016). [Cited on pages 4, 49, 72, 79, 86, and 120.]

[48] A. Sargsyan, E. Klinger, G. Hakhumyan, A. Tonoyan, A. Papoyan, C. Leroy, and D. Sarkisyan. *Decoupling of hyperfine structure of Cs D_1 line in strong magnetic field studied by selective reflection from a*

nanocell. Journal of the Optical Society of America B **34**, 776 (2017). [Cited on page 4.]

[49] M. Saffman, T. G. Walker, and K. Mølmer. *Quantum information with Rydberg atoms*. Reviews of Modern Physics **82**, 2313 (2010). [Cited on page 5.]

[50] C. Cohen-Tannoudji, J. Dupont-Roc, and G. Grynberg. *Atom-Photon Interactions*. Wiley-VCH Verlag GmbH, Weinheim, Germany (1998). [Cited on page 9.]

[51] K. Blum. *Density Matrix Theory and Applications*, volume 64 of *Springer Series on Atomic, Optical, and Plasma Physics*. Springer Berlin Heidelberg, Berlin, Heidelberg, 3rd edition (2012). [Cited on pages 10 and 11.]

[52] D. Suter. *The Physics of Laser-Atom Interactions*. Cambridge University Press (1997). [Cited on page 11.]

[53] H. P. Breuer and F. Petruccione. *The Theory of Open Quantum Systems*. Oxford University Press (2002). [Cited on page 12.]

[54] R. Loudon. *The Quantum Theory of Light*. Oxford University Press, Oxford (2000). [Cited on pages 13, 15, 94, 116, and 117.]

[55] B. E. Sherlock and I. G. Hughes. *How weak is a weak probe in laser spectroscopy?* American Journal of Physics **77**, 111 (2009). [Cited on pages 14, 33, 48, 52, and 133.]

[56] U. Volz and H. Schmoranzer. *Precision lifetime measurements on alkali atoms and on helium by beam-gas-laser spectroscopy*. Physica Scripta **T65**, 48 (1996). [Cited on pages 15 and 40.]

[57] C. Aminoff and M. Pinard. *Velocity selective optical pumping*. Journal de Physique **43**, 263 (1982). [Cited on page 15.]

[58] B. H. Bransden and C. J. Joachain. *Physics of Atoms and Molecules*. Pearson Education. Prentice Hall (2003). [Cited on pages 16 and 18.]

[59] G. K. Woodgate. *ELEMENTARY ATOMIC STRUCTURE*. Oxford University Press, USA (1980). [Cited on page 18.]

[60] A. Sargsyan, A. Tonoyan, G. Hakhumyan, A. Papoyan, E. Mariotti, and D. Sarkisyan. *Giant modification of atomic transition probabilities*

induced by a magnetic field: forbidden transitions become predominant. Laser Physics Letters **11**, 055701 (2014). [Cited on page 21.]

[61] S. E. Harris, J. E. Field, and A. Imamoğlu. *Nonlinear optical processes using electromagnetically induced transparency.* Physical Review Letters **64**, 1107 (1990). [Cited on pages 23 and 24.]

[62] K.-J. Boller, A. Imamoğlu, and S. E. Harris. *Observation of electromagnetically induced transparency.* Physical Review Letters **66**, 2593 (1991). [Cited on page 23.]

[63] H. Schmidt and R. J. Ram. *All-optical wavelength converter and switch based on electromagnetically induced transparency.* Applied Physics Letters **76**, 3173 (2000). [Cited on page 24.]

[64] A. K. Mohapatra, T. R. Jackson, and C. S. Adams. *Coherent Optical Detection of Highly Excited Rydberg States Using Electromagnetically Induced Transparency.* Physical Review Letters **98**, 113003 (2007). [Cited on pages 24 and 25.]

[65] D. Maxwell, D. J. Szwer, D. Paredes-Barato, H. Busche, J. D. Pritchard, A. Gauguet, K. J. Weatherill, M. P. A. Jones, and C. S. Adams. *Storage and Control of Optical Photons Using Rydberg Polaritons.* Physical Review Letters **110**, 103001 (2013). [Cited on pages 24 and 90.]

[66] H. Busche, P. Huillery, S. W. Ball, T. Ilieva, M. P. A. Jones, and C. Adams. *Contactless nonlinear optics mediated by long-range Rydberg interactions.* Nature Physics (2017). [Cited on page 24.]

[67] D. Budker, D. F. Kimball, S. M. Rochester, and V. V. Yashchuk. *Nonlinear Magneto-optics and Reduced Group Velocity of Light in Atomic Vapor with Slow Ground State Relaxation.* Physical Review Letters **83**, 1767 (1999). [Cited on page 24.]

[68] D. F. Phillips, A. Fleischhauer, A. Mair, R. L. Walsworth, and M. D. Lukin. *Storage of Light in Atomic Vapor.* Physical Review Letters **86**, 783 (2001). [Cited on page 24.]

[69] B. Zhao, Y.-A. Chen, X.-H. Bao, T. Strassel, C.-S. Chuu, X.-M. Jin, J. Schmiedmayer, Z.-S. Yuan, S. Chen, and J.-W. Pan. *A millisecond quantum memory for scalable quantum networks.* Nature Physics **5**, 95 (2009). [Cited on page 24.]

[70] S. D. Badger, I. G. Hughes, and C. S. Adams. *Hyperfine effects in electromagnetically induced transparency.* Journal of Physics B: Atomic, Molecular and Optical Physics **34**, L749 (2001). [Cited on pages 24, 40, and 72.]

[71] D. Budker, V. Yashchuk, and M. Zolotorev. *Nonlinear Magneto-optic Effects with Ultranarrow Widths.* Physical Review Letters **81**, 5788 (1998). [Cited on page 24.]

[72] A. Sargsyan, R. Mirzoyan, and D. Sarkisyan. *Splitting of the electromagnetically induced transparency resonance on ^{85}Rb atoms in strong magnetic fields up to the Paschen-Back regime.* JETP Letters **96**, 303 (2012). [Cited on pages 25 and 52.]

[73] A. Kölle, G. Epple, H. Kübler, R. Löw, and T. Pfau. *Four-wave mixing involving Rydberg states in thermal vapor.* Physical Review A **85**, 063821 (2012). [Cited on page 25.]

[74] R. T. Willis, F. E. Becerra, L. A. Orozco, and S. L. Rolston. *Four-wave mixing in the diamond configuration in an atomic vapor.* Physical Review A **79**, 033814 (2009). [Cited on pages 25 and 70.]

[75] Y.-S. Lee, S. M. Lee, H. Kim, and H. S. Moon. *Highly bright photon-pair generation in Doppler-broadened ladder-type atomic system.* Optics Express **24**, 28083 (2016). [Cited on pages 25, 52, 70, and 126.]

[76] S. H. Autler and C. H. Townes. *Stark Effect in Rapidly Varying Fields.* Physical Review **100**, 703 (1955). [Cited on pages 26 and 27.]

[77] J. Gea-Banacloche, Y.-q. Li, S.-z. Jin, and M. Xiao. *Electromagnetically induced transparency in ladder-type inhomogeneously broadened media: Theory and experiment.* Physical Review A **51**, 576 (1995). [Cited on pages 27, 46, and 52.]

[78] J. Keaveney, I. G. Hughes, A. Sargsyan, D. Sarkisyan, and C. S. Adams. *Maximal Refraction and Superluminal Propagation in a Gaseous Nanolayer.* Physical Review Letters **109**, 233001 (2012). [Cited on pages 27 and 91.]

[79] A. Sargsyan, D. Sarkisyan, U. Krohn, J. Keaveney, and C. Adams. *Effect of buffer gas on an electromagnetically induced transparency in a ladder system using thermal rubidium vapor.* Physical Review A **82**, 045806 (2010). [Cited on pages 33, 64, 79, and 91.]

[80] P. Siddons, C. S. Adams, C. Ge, and I. G. Hughes. *Absolute absorption on rubidium D lines: comparison between theory and experiment.* Journal of Physics B: Atomic, Molecular and Optical Physics **41**, 155004 (2008). [Cited on pages 35, 77, and 142.]

[81] I. G. Hughes and T. P. A. Hase. *Measurements and their Uncertainties: A Practical Guide to Modern Error Analysis.* Oxford University Press, Oxford (2010). [Cited on pages 37, 41, 84, 113, and 114.]

[82] D. J. Whiting, E. Bimbard, J. Keaveney, M. A. Zentile, C. S. Adams, and I. G. Hughes. *Electromagnetically induced absorption in a non-degenerate three-level ladder system.* Optics Letters **40**, 4289 (2015). [Cited on pages 37, 46, 47, 72, 86, and 120.]

[83] B. K. Sahoo. *Conforming the measured lifetimes of the* $5d^2D_{3/2,5/2}$ *states in Cs with theory.* Physical Review A **93**, 022503 (2016). [Cited on page 40.]

[84] M. S. Safronova, C. J. Williams, and C. W. Clark. *Relativistic many-body calculations of electric-dipole matrix elements, lifetimes, and polarizabilities in rubidium.* Physical Review A **69**, 022509 (2004). [Cited on pages 40 and 43.]

[85] M. Weissbluth. *Atoms and Molecules.* Elsevier Science (1978). [Cited on page 43.]

[86] H. Gross, B. Dörband, and H. Müller. *Polarimetry.* In *Handbook of Optical Systems*, pp. 559–642. Wiley-VCH Verlag GmbH & Co. KGaA, Weinheim, Germany (2015). [Cited on page 45.]

[87] K. Gillen-Christandl, G. D. Gillen, M. J. Piotrowicz, and M. Saffman. *Comparison of Gaussian and super Gaussian laser beams for addressing atomic qubits.* Applied Physics B **122**, 131 (2016). [Cited on page 46.]

[88] D. A. Smith and I. G. Hughes. *The role of hyperfine pumping in multilevel systems exhibiting saturated absorption.* American Journal of Physics **72**, 631 (2004). [Cited on pages 49 and 141.]

[89] U. Gaubatz, P. Rudecki, S. Schiemann, and K. Bergmann. *Population transfer between molecular vibrational levels by stimulated Raman scattering with partially overlapping laser fields. A new concept and experimental results.* The Journal of Chemical Physics **92**, 5363 (1990). [Cited on page 51.]

[90] S.-q. Kuang, R.-g. Wan, P. Du, Y. Jiang, and J.-y. Gao. *Transmission and reflection of electromagnetically induced absorption grating in homogeneous atomic media.* Optics Express **16**, 15455 (2008). [Cited on page 51.]

[91] S. A. Babin, D. V. Churkin, E. V. Podivilov, V. V. Potapov, and D. A. Shapiro. *Splitting of the peak of electromagnetically induced transparency by the higher-order spatial harmonics of the atomic coherence.* Physical Review A **67**, 043808 (2003). [Cited on page 51.]

[92] I.-H. Bae, H. S. Moon, M.-K. Kim, L. Lee, and J. B. Kim. *Transformation of electromagnetically induced transparency into enhanced absorption with a standing-wave coupling field in an Rb vapor cell.* Optics Express **18**, 1389 (2010). [Cited on page 51.]

[93] A. M. Akulshin, S. Barreiro, and A. Lezama. *Electromagnetically induced absorption and transparency due to resonant two-field excitation of quasidegenerate levels in Rb vapor.* Physical Review A **57**, 2996 (1998). [Cited on page 51.]

[94] A. Lezama, S. Barreiro, and A. M. Akulshin. *Electromagnetically induced absorption.* Physical Review A **59**, 4732 (1999). [Cited on page 51.]

[95] G. S. Agarwal, T. N. Dey, and S. Menon. *Knob for changing light propagation from subluminal to superluminal.* Physical Review A **64**, 053809 (2001). [Cited on page 52.]

[96] E. E. Mikhailov, V. A. Sautenkov, Y. V. Rostovtsev, and G. R. Welch. *Absorption resonance and large negative delay in rubidium vapor with a buffer gas.* Journal of the Optical Society of America B **21**, 425 (2004). [Cited on page 52.]

[97] H. Sun, H. Guo, Y. Bai, D. Han, S. Fan, and X. Chen. *Light propagation from subluminal to superluminal in a three-level Λ-type system.* Physics Letters A **335**, 68 (2005). [Cited on page 52.]

[98] C.-L. Cui, J.-K. Jia, J.-W. Gao, Y. Xue, G. Wang, and J.-H. Wu. *Ultraslow and superluminal light propagation in a four-level atomic system.* Physical Review A **76**, 033815 (2007). [Cited on page 52.]

[99] M. Tanasittikosol, J. D. Pritchard, D. Maxwell, A. Gauguet, K. J. Weatherill, R. M. Potvliege, and C. S. Adams. *Microwave dressing*

of Rydberg dark states. Journal of Physics B: Atomic, Molecular and Optical Physics **44**, 184020 (2011). [Cited on page 52.]

[100] A. M. Akulshin, S. Barreiro, and A. Lezama. *Steep Anomalous Dispersion in Coherently Prepared Rb Vapor.* Physical Review Letters **83**, 4277 (1999). [Cited on page 52.]

[101] A. V. Taichenachev, A. M. Tumaikin, and V. I. Yudin. *Electromagnetically induced absorption in a four-state system.* Physical Review A **61**, 011802 (1999). [Cited on page 52.]

[102] C. Goren, A. D. Wilson-Gordon, M. Rosenbluh, and H. Friedmann. *Atomic four-level N systems.* Physical Review A **69**, 053818 (2004). [Cited on page 52.]

[103] H. S. Moon and T. Jeong. *Three-photon electromagnetically induced absorption in a ladder-type atomic system.* Physical Review A **89**, 033822 (2014). [Cited on page 52.]

[104] C. Goren, A. D. Wilson-Gordon, M. Rosenbluh, and H. Friedmann. *Electromagnetically induced absorption due to transfer of population in degenerate two-level systems.* Physical Review A **70**, 043814 (2004). [Cited on page 52.]

[105] S. Ranjita Chanu, K. Pandey, and V. Natarajan. *Conversion between electromagnetically induced transparency and absorption in a three-level lambda system.* EPL (Europhysics Letters) **98**, 44009 (2012). [Cited on page 52.]

[106] M. G. Bason, A. K. Mohapatra, K. J. Weatherill, and C. S. Adams. *Narrow absorptive resonances in a four-level atomic system.* Journal of Physics B: Atomic, Molecular and Optical Physics **42**, 075503 (2009). [Cited on page 52.]

[107] E. Tilchin, A. D. Wilson-Gordon, and O. Firstenberg. *Effects of thermal motion on electromagnetically induced absorption.* Physical Review A **83**, 053812 (2011). [Cited on page 52.]

[108] A. Sargsyan, A. Tonoyan, G. Hakhumyan, C. Leroy, Y. Pashayan-Leroy, and D. Sarkisyan. *Complete hyperfine Paschen-Back regime at relatively small magnetic fields realized in potassium nano-cell.* EPL (Europhysics Letters) **110**, 23001 (2015). [Cited on page 52.]

[109] E. Kyrölä and R. Salomaa. *Probe spectroscopy in an inhomogeneously broadened three-level system saturated by an intense standing wave.* Physical Review A **23**, 1874 (1981). [Cited on pages 52, 54, and 67.]

[110] O. S. Heavens. *Radiative Transition Probabilities of the Lower Excited States of the Alkali Metals.* Journal of the Optical Society of America **51**, 1058 (1961). [Cited on pages 62 and 79.]

[111] Y. R. Shen. *The Principles of Nonlinear Optics.* Pure & Applied Optics Series: 1-349. Wiley (1984). [Cited on page 69.]

[112] P. H. S. Ribeiro, C. Schwob, A. Maître, and C. Fabre. *Sub-shot-noise high-sensitivity spectroscopy with optical parametric oscillator twin beams.* Optics Letters **22**, 1893 (1997). [Cited on page 70.]

[113] R. C. Pooser and B. Lawrie. *Ultrasensitive measurement of microcantilever displacement below the shot-noise limit.* Optica **2**, 393 (2015). [Cited on page 70.]

[114] L. Q. Chen, G.-W. Zhang, C.-l. Bian, C.-H. Yuan, Z. Y. Ou, and W. Zhang. *Observation of the Rabi Oscillation of Light Driven by an Atomic Spin Wave.* Physical Review Letters **105**, 133603 (2010). [Cited on page 70.]

[115] F. Ripka, Y.-H. Chen, R. Löw, and T. Pfau. *Rydberg polaritons in a thermal vapor.* Physical Review A **93**, 053429 (2016). [Cited on pages 70 and 121.]

[116] R. T. Willis, F. E. Becerra, L. A. Orozco, and S. L. Rolston. *Photon statistics and polarization correlations at telecommunications wavelengths from a warm atomic ensemble.* Optics Express **19**, 14632 (2011). [Cited on pages 70 and 120.]

[117] C. F. McCormick, V. Boyer, E. Arimondo, and P. D. Lett. *Strong relative intensity squeezing by four-wave mixing in rubidium vapor.* Optics Letters **32**, 178 (2007). [Cited on page 70.]

[118] V. Boyer, A. Marino, and P. Lett. *Generation of Spatially Broadband Twin Beams for Quantum Imaging.* Physical Review Letters **100**, 143601 (2008). [Cited on page 70.]

[119] G. Walker, A. S. Arnold, and S. Franke-Arnold. *Trans-Spectral Orbital Angular Momentum Transfer via Four-Wave Mixing in Rb Vapor.* Physical Review Letters **108**, 243601 (2012). [Cited on page 70.]

[120] P. R. Hemmer, D. P. Katz, J. Donoghue, M. S. Shahriar, P. Kumar, and M. Cronin-Golomb. *Efficient low-intensity optical phase conjugation based on coherent population trapping in sodium*. Optics Letters **20**, 982 (1995). [Cited on pages 70 and 90.]

[121] C. H. van der Wal. *Atomic Memory for Correlated Photon States*. Science **301**, 196 (2003). [Cited on page 70.]

[122] A. Kuzmich, W. P. Bowen, A. D. Boozer, A. Boca, C. W. Chou, L.-M. Duan, and H. J. Kimble. *Generation of nonclassical photon pairs for scalable quantum communication with atomic ensembles*. Nature **423**, 731 (2003). [Cited on pages 70 and 91.]

[123] S. V. Polyakov, C. W. Chou, D. Felinto, and H. J. Kimble. *Temporal Dynamics of Photon Pairs Generated by an Atomic Ensemble*. Physical Review Letters **93**, 263601 (2004). [Cited on page 70.]

[124] M. Parniak, A. Leszczyński, and W. Wasilewski. *Coupling of four-wave mixing and Raman scattering by ground-state atomic coherence*. Physical Review A **93**, 053821 (2016). [Cited on page 70.]

[125] A. Leszczyński, M. Parniak, and W. Wasilewski. *Phase matching alters spatial multiphoton processes in dense atomic ensembles*. Optics Express **25**, 284 (2017). [Cited on page 70.]

[126] F. Becerra, R. Willis, S. Rolston, and L. Orozco. *Nondegenerate four-wave mixing in rubidium vapor: The diamond configuration*. Physical Review A **78**, 013834 (2008). [Cited on page 70.]

[127] M. Parniak and W. Wasilewski. *Interference and nonlinear properties of four-wave-mixing resonances in thermal vapor: Analytical results and experimental verification*. Physical Review A **91**, 023418 (2015). [Cited on pages 70 and 72.]

[128] P. Palittapongarnpim, A. MacRae, and A. I. Lvovsky. *Note: A monolithic filter cavity for experiments in quantum optics*. Review of Scientific Instruments **83**, 066101 (2012). [Cited on page 71.]

[129] Y. Castin and K. Mölmer. *Maxwell-Bloch equations: A unified view of nonlinear optics and nonlinear atom optics*. Physical Review A **51**, R3426 (1995). [Cited on page 79.]

[130] B. Huber, A. Kölle, and T. Pfau. *Motion-induced signal revival in pulsed Rydberg four-wave mixing beyond the frozen-gas limit.* Physical Review A **90**, 053806 (2014). [Cited on pages 84 and 121.]

[131] A. L. Marchant, S. Haendel, T. P. Wiles, S. A. Hopkins, C. S. Adams, and S. L. Cornish. *Off resonance laser frequency stabilization using the Faraday effect.* Optics Letters **36**, 3 (2010). [Cited on pages 86 and 125.]

[132] C. H. Bennett and D. P. DiVincenzo. *Quantum information and computation.* Nature **404**, 247 (2000). [Cited on page 87.]

[133] A. Galindo and M. A. Martín-Delgado. *Information and computation: Classical and quantum aspects.* Reviews of Modern Physics **74**, 347 (2002). [Cited on page 87.]

[134] R. Blatt and C. F. Roos. *Quantum simulations with trapped ions.* Nature Physics **8**, 277 (2012). [Cited on page 87.]

[135] I. M. Georgescu, S. Ashhab, and F. Nori. *Quantum simulation.* Reviews of Modern Physics **86**, 153 (2014). [Cited on page 87.]

[136] V. Giovannetti, S. Lloyd, and L. Maccone. *Advances in quantum metrology.* Nature Photonics **5**, 222 (2011). [Cited on page 87.]

[137] J. F. Clauser. *Experimental distinction between the quantum and classical field-theoretic predictions for the photoelectric effect.* Physical Review D **9**, 853 (1974). [Cited on page 88.]

[138] P. Grangier, G. Roger, and A. Aspect. *Experimental Evidence for a Photon Anticorrelation Effect on a Beam Splitter: A New Light on Single-Photon Interferences.* Europhysics Letters (EPL) **1**, 173 (1986). [Cited on page 88.]

[139] C. K. Hong, Z. Y. Ou, and L. Mandel. *Measurement of subpicosecond time intervals between two photons by interference.* Physical Review Letters **59**, 2044 (1987). [Cited on page 88.]

[140] LIGO Scientific Collaboration. *Enhanced sensitivity of the LIGO gravitational wave detector by using squeezed states of light.* Nature Photonics **7**, 613 (2013). [Cited on page 88.]

[141] T. D. Ladd, F. Jelezko, R. Laflamme, Y. Nakamura, C. Monroe, and J. L. O'Brien. *Quantum computers.* Nature **464**, 45 (2010). [Cited on page 88.]

[142] C. Santori, D. Fattal, J. Vuckovic, G. S. Solomon, and Y. Yamamoto. *Single-photon generation with InAs quantum dots.* New Journal of Physics **6**, 89 (2004). [Cited on page 88.]

[143] E. Wu, J. R. Rabeau, G. Roger, F. Treussart, H. Zeng, P. Grangier, S. Prawer, and J.-F. Roch. *Room temperature triggered single-photon source in the near infrared.* New Journal of Physics **9**, 434 (2007). [Cited on page 88.]

[144] K. Hennessy, A. Badolato, M. Winger, D. Gerace, M. Atatüre, S. Gulde, S. Fält, E. L. Hu, and A. Imamoğlu. *Quantum nature of a strongly coupled single quantum dot?cavity system.* Nature **445**, 896 (2007). [Cited on page 88.]

[145] P. Siyushev, G. Stein, J. Wrachtrup, and I. Gerhardt. *Molecular photons interfaced with alkali atoms.* Nature **509**, 66 (2014). [Cited on page 89.]

[146] B. Darquie. *Controlled Single-Photon Emission from a Single Trapped Two-Level Atom.* Science **309**, 454 (2005). [Cited on page 89.]

[147] B. B. Blinov, D. L. Moehring, L.-M. Duan, and C. Monroe. *Observation of entanglement between a single trapped atom and a single photon.* Nature **428**, 153 (2004). [Cited on page 89.]

[148] J. McKeever. *Deterministic Generation of Single Photons from One Atom Trapped in a Cavity.* Science **303**, 1992 (2004). [Cited on page 89.]

[149] T. Wilk, S. C. Webster, A. Kuhn, and G. Rempe. *Single-Atom Single-Photon Quantum Interface.* Science **317**, 488 (2007). [Cited on page 89.]

[150] M. Keller, B. Lange, K. Hayasaka, W. Lange, and H. Walther. *Continuous generation of single photons with controlled waveform in an ion-trap cavity system.* Nature **431**, 1075 (2004). [Cited on page 89.]

[151] R. Maiwald, A. Golla, M. Fischer, M. Bader, S. Heugel, B. Chalopin, M. Sondermann, and G. Leuchs. *Collecting more than half the fluorescence photons from a single ion.* Physical Review A **86**, 043431 (2012). [Cited on page 89.]

[152] C. W. Chou, S. V. Polyakov, A. Kuzmich, and H. J. Kimble. *Single-Photon Generation from Stored Excitation in an Atomic Ensemble.* Physical Review Letters **92**, 213601 (2004). [Cited on page 90.]

[153] Y. O. Dudin and A. Kuzmich. *Strongly interacting Rydberg excitations of a cold atomic gas.* Science (New York, N.Y.) **336**, 887 (2012). [Cited on page 90.]

[154] M. D. Lukin, A. B. Matsko, M. Fleischhauer, and M. O. Scully. *Quantum Noise and Correlations in Resonantly Enhanced Wave Mixing Based on Atomic Coherence.* Physical Review Letters **82**, 1847 (1999). [Cited on page 90.]

[155] O. Firstenberg, M. Shuker, A. Ron, and N. Davidson. *Colloquium : Coherent diffusion of polaritons in atomic media.* Reviews of Modern Physics **85**, 941 (2013). [Cited on page 90.]

[156] S. Brandt, A. Nagel, R. Wynands, and D. Meschede. *Buffer-gas-induced linewidth reduction of coherent dark resonances to below* 50 *Hz.* Physical Review A **56**, R1063 (1997). [Cited on page 91.]

[157] D. Budker and M. Romalis. *Optical magnetometry.* Nature Physics **3**, 227 (2007). [Cited on page 91.]

[158] M. V. Balabas, T. Karaulanov, M. P. Ledbetter, and D. Budker. *Polarized Alkali-Metal Vapor with Minute-Long Transverse Spin-Relaxation Time.* Physical Review Letters **105**, 070801 (2010). [Cited on page 91.]

[159] A. Sargsyan, Y. Pashayan-Leroy, C. Leroy, and D. Sarkisyan. *Collapse and revival of a Dicke-type coherent narrowing in potassium vapor confined in a nanometric thin cell.* Journal of Physics B: Atomic, Molecular and Optical Physics **49**, 075001 (2016). [Cited on page 91.]

[160] S. J. Seltzer and M. V. Romalis. *High-temperature alkali vapor cells with antirelaxation surface coatings.* Journal of Applied Physics **106**, 114905 (2009). [Cited on page 91.]

[161] S. Clemmen, A. Farsi, S. Ramelow, and A. L. Gaeta. *Ramsey Interference with Single Photons.* Physical Review Letters **117**, 223601 (2016). [Cited on page 91.]

[162] P. Treutlein. *Photon Qubit is Made of Two Colors.* Physics **9**, 135 (2016). [Cited on page 91.]

[163] S. Haroche. *Quantum Beats and Time-Resolved Fluorescence Spectroscopy.* In K. Shimoda (editor), *High-Resolution Laser Spectroscopy*, pp. 253–313. Springer-Verlag, Berlin, Heidelberg, New York (1976). [Cited on page 91.]

[164] S. Du, J. Wen, and M. H. Rubin. *Narrowband biphoton generation near atomic resonance*. Journal of the Optical Society of America B **25**, C98 (2008). [Cited on pages 95 and 119.]

[165] S. Ramelow, A. Mech, M. Giustina, S. Gröblacher, W. Wieczorek, J. Beyer, A. Lita, B. Calkins, T. Gerrits, S. W. Nam, A. Zeilinger, and R. Ursin. *Highly efficient heralding of entangled single photons*. Opt. Express **21**, 6707 (2013). [Cited on page 108.]

[166] A. Gallagher and D. E. Pritchard. *Exoergic collisions of cold Na^*-Na*. Physical Review Letters **63**, 957 (1989). [Cited on page 111.]

[167] L. Barbier and M. Cheret. *Energy pooling process in rubidium vapour*. Journal of Physics B: Atomic and Molecular Physics **16**, 3213 (1983). [Cited on page 111.]

[168] I. G. Hughes. *Velocity selection in a Doppler-broadened ensemble of atoms interacting with a monochromatic laser beam*. Journal of Modern Optics **0**, 1 (2017). [Cited on pages 116 and 117.]

[169] S. Haroche, J. A. Paisner, and A. L. Schawlow. *Hyperfine Quantum Beats Observed in Cs Vapor under Pulsed Dye Laser Excitation*. Physical Review Letters **30**, 948 (1973). [Cited on page 119.]

[170] A. Aspect, J. Dalibard, P. Grangier, and G. Roger. *Quantum beats in continuously excited atomic cascades*. Optics Communications **49**, 429 (1984). [Cited on page 119.]

[171] C. G. Wade, N. Šibalić, J. Keaveney, C. S. Adams, and K. J. Weatherill. *Probing an excited-state atomic transition using hyperfine quantum-beat spectroscopy*. Physical Review A **90**, 033424 (2014). [Cited on page 119.]

[172] M. Gross, J. M. Raimond, and S. Haroche. *Doppler Beats in Superradiance*. Physical Review Letters **40**, 1711 (1978). [Cited on page 119.]

[173] S.-J. Yang, X.-H. Bao, and J.-W. Pan. *Modulation of single-photon-level wave packets with two-component electromagnetically induced transparency*. Physical Review A **91**, 053805 (2015). [Cited on page 119.]

[174] J. Wen, S. Du, Y. Zhang, M. Xiao, and M. H. Rubin. *Nonclassical light generation via a four-level inverted-Y system*. Physical Review A **77**, 033816 (2008). [Cited on page 120.]

[175] Y. O. Dudin, L. Li, and A. Kuzmich. *Light storage on the time scale of a minute*. Physical Review A **87**, 031801 (2013). [Cited on page 120.]

[176] N. Šibalić, J. M. Kondo, C. S. Adams, and K. J. Weatherill. *Dressed-state electromagnetically induced transparency for light storage in uniform-phase spin waves.* Physical Review A **94**, 033840 (2016). [Cited on page 120.]

[177] W. Dür, G. Vidal, and J. I. Cirac. *Three qubits can be entangled in two inequivalent ways.* Physical Review A **62**, 062314 (2000). [Cited on pages 121 and 125.]

[178] L.-M. Duan, M. D. Lukin, J. I. Cirac, and P. Zoller. *Long-distance quantum communication with atomic ensembles and linear optics.* Nature **414**, 413 (2001). [Cited on page 126.]

[179] K. F. Reim, P. Michelberger, K. C. Lee, J. Nunn, N. K. Langford, and I. A. Walmsley. *Single-Photon-Level Quantum Memory at Room Temperature.* Physical Review Letters **107**, 053603 (2011). [Cited on page 127.]

[180] P. S. Michelberger, T. F. M. Champion, M. R. Sprague, K. T. Kaczmarek, M. Barbieri, X. M. Jin, D. G. England, W. S. Kolthammer, D. J. Saunders, J. Nunn, and I. A. Walmsley. *Interfacing GHz-bandwidth heralded single photons with a warm vapour Raman memory.* New Journal of Physics **17**, 043006 (2015). [Cited on page 127.]

[181] K. Shiraishi, F. Tajima, and S. Kawakami. *Compact Faraday rotator for an optical isolator using magnets arranged with alternating polarities.* Optics Letters **11**, 82 (1986). [Cited on page 129.]

[182] H. J. Metcalf and P. van der Straten. *Laser Cooling and Trapping.* Graduate Texts in Contemporary Physics. Springer New York, New York, NY (1999). [Cited on page 133.]

[183] A. Corney. *Atomic and Laser Spectroscopy.* Oxford University Press, Oxford (1977). [Cited on page 133.]

[184] J. Sagle, R. K. Namiotka, and J. Huennekens. *Measurement and modelling of intensity dependent absorption and transit relaxation on the cesium line.* Journal of Physics B: Atomic, Molecular and Optical Physics **29**, 2629 (1996). [Cited on page 134.]

[185] C. P. Pearman, C. S. Adams, S. G. Cox, P. F. Griffin, D. A. Smith, and I. G. Hughes. *Polarization spectroscopy of a closed atomic transition: applications to laser frequency locking.* Journal of Physics B: Atomic, Molecular and Optical Physics **35**, 5141 (2002). [Cited on page 137.]

[186] K. J. Åström and T. Hägglund. *PID Controllers: Theory, Design, and Tuning*. International Society of Automation, 2nd editio edition (1995). [Cited on page 137.]

[187] G. G. Stokes. *On the Change of Refrangibility of Light*. Philosophical Transactions of the Royal Society of London **142**, 463 (1852). [Cited on page 138.]

[188] L. Weller, R. J. Bettles, P. Siddons, C. S. Adams, and I. G. Hughes. *Absolute absorption on the rubidium D_1 line including resonant dipole-dipole interactions*. Journal of Physics B: Atomic, Molecular and Optical Physics **44**, 195006 (2011). [Cited on page 142.]